University of New Mexico
UNM Digital Repository

Chemistry ETDs | Electronic Theses and Dissertations

Fall 11-1-2016

MOLECULAR TETRAPODS FOR OPTOELECTRONIC APPLICATIONS

Jianzhong Yang
University of New Mexico

Follow this and additional works at: https://digitalrepository.unm.edu/chem_etds

 Part of the Chemistry Commons, and the Polymer and Organic Materials Commons

Recommended Citation
Yang, Jianzhong. "MOLECULAR TETRAPODS FOR OPTOELECTRONIC APPLICATIONS." (2016).
https://digitalrepository.unm.edu/chem_etds/58

This Dissertation is brought to you for free and open access by the Electronic Theses and Dissertations at UNM Digital Repository. It has been accepted for inclusion in Chemistry ETDs by an authorized administrator of UNM Digital Repository. For more information, please contact disc@unm.edu.

Jianzhong Yang
Candidate

Chemistry and Chemical Biology
Department

This dissertation is approved, and it is acceptable in quality and form for publication:

Approved by the Dissertation Committee:

Prof. Yang Qin, Chairperson

Prof. Wei Wang

Prof. John K. Grey

Prof. Sang Eon Han

MOLECULAR TETRAPODS FOR OPTOELECTRONIC APPLICATIONS

BY

JIANZHONG YANG

B.S. Applied Chemistry, Shantou University, China, 2011

DISSERTATION

Submitted in Partial Fulfillment of the
Requirements for the Degree of

Doctor of Philosophy
Chemistry

The University of New Mexico
Albuquerque, New Mexico

December 2016

ACKNOWLEDGEMENTS

First and foremost, I want to thank my advisor Dr. Yang Qin for his guidance and assistance on my research projects during the past five years. Dr. Qin could always use his knowledge and experience to guide me to tackle the problems in my projects and to push them forward. I really appreciate his patience and individual hands-on training, which helped me gain extensive experimental skills. More importantly, he taught me the way of scientific thinking and how to do research step by step. Without his help, it would be impossible to have this dissertation in press. Anyway, I believe the skills, knowledge and research experience that I gained from him will benefit me in the future.

Secondly, I would like to express my gratitude to my committee members, Dr. Wang, Dr. Grey and Dr. Han for their precious time spent in reading this dissertation and valuable suggestions on finalizing this draft. In addition, I want to thank them for their advices during my research proposal, which really expedited the progress of this project.

Thirdly, all our lab collaborators are also acknowledged for their effort to facilitate this project. Dr. Ying-Bing Jiang gave me access to the TEM facility and helped me for troubleshooting during the measurements; Dr. Kemp and his postdoc Dr. Diane Dickie helped me with single crystal XRD. Besides, my thanks also go to Dr. Fu-Sen Liang for his generosity to allow me to access his lab microscope conveniently during the past years.

Fourthly, I am grateful to all my current and former lab members. I will give special thanks to Fei Li, who is our previous lab member. He taught me how to use most of the instruments in our lab, gave me useful suggestions on my research and also encouraged me to go through the difficulties.

Moreover, I want to thank my parents for their understanding and support on my PhD study in the USA. Especially, their great help on taking care of my son during the busy research times. At the same time, many thanks to my local friends James and Priscilla Duncan, for their great help on guiding me adapt to the lifestyle in Albuquerque and also arranging the impressive wedding ceremony for my wife and me.

At last, I also want to appreciate my wife, who is also a PhD student in our department. Thanks for her coming to USA to pursuit the PhD together with me; thanks for her encouragement on my research; thanks for her care on my daily life; and thanks for her greatness to bring us a cute son.

MOLECULAR TETRAPODS FOR OPTOELECTRONIC APPLICATIONS

BY

JIANZHONG YANG

B.S. Applied Chemistry, Shantou University, China, 2011

Ph.D. Chemistry, University of New Mexico, USA, 2016

ABSTRACT

Most conjugated molecules including polymers and small molecules applied in organic solar cells (OSCs) have linear structures containing multiple aromatic groups connected in series. However, unfavorable film forming ability and grain boundaries both originated from high crystallinity of linear small molecules are detrimental to device performances. Thus, among multi-dimensional structures, tetrapodal molecules are especially interesting owing to their unique ability to mutually interlock, which prevents dislodging and provides high structural stabilities. Such molecular design can also increase absorption cross-sections and provide more extensively percolating pathways for charge transport, making such molecular tetrapods promising in OSCs applications. In my dissertation, I will not only include the synthesis and characterization of tetrapodal molecules, but also discussing structure-property relationships of such 3-D small molecules and their applications in multi-component OSCs. Besides, I also include the synthesis and characterization of a series of novel fullerene-borate ionic complexes, and their potential application will be discussed, too.

To start with, the tetrapodal molecule **SO**, containing a tetraphenylsilane core and four cyanoester functionalized terthiophene arms, was firstly discussed. Absorption, X-ray scattering and differential scanning calorimetry (DSC) experiments indicate crystalline nature of **SO** but very slow crystallization kinetics. Solar cells employing **SO** and phenyl-C_{61}-butyric acid methyl ester (PCBM) were fabricated and evaluated. Relatively low performance was obtained mainly due to the lack of optimal phase separation under various processing conditions including as-cast, thermal annealing and solvent annealing. Addition of poly(thienylene vinylene) (PTV), a low bandgap highly

crystalline conjugated polymer, into the **SO**/PCBM blend was found to induce device favorable phase separation and the polymer was found to act as the major hole conductor. Such ternary blend devices showed cooperatively improved performances over binary devices employing either **SO** or PTV alone.

Since our previous studies on **SO** and its model compound **MO** indicate that the slow crystallization behavior in the tetrapod may intrinsically originate from each of its arms, we conjecture that we may be able to increase the crystallization kinetics of these tetrapods by removing the alkyl side chains in the middle of each arm and by using more rigid and planar electron-accepting moieties such as the fluorinated benzothiadiazole (FBTD) units. Thus, a modified tetrapodal molecule **SFBTD** was synthesized successfully. However, absorption spectroscopy, DSC and XRD experiments reveal low degree of crystallinity in this compound and slow crystallization kinetics. Bulk heterojunction (BHJ) OSCs employing **SFBTD** and fullerene derivatives exhibit power conversion efficiencies (*PCE*s) up to 1.05 % and open-circuit voltage (V_{OC}) values as high as 1.02 V. To the best of our knowledge, this is the highest *PCE* obtained for OSCs employing molecular tetrapods as donor materials. These devices are relatively thermally stable due to the known ability of breakwater tetrapods to inter-lock, preventing dislodging and sliding. The lack of favorable phase separations and low hole mobilities of the blend films are the major factors limiting the device performance. Ternary blend devices by the addition of three low bandgap PTV derivatives were fabricated and discussed.

In the last chapter, a series of fullerene-borate ionic complexes were synthesized successfully. Various chromophores can be introduced into our fullerene-borate ionic

complex system through facile Sonogashira coupling reaction, so the optical and electrical properties of complex can be easily tuned. The fluorescence quenching study on **FP-Ant** indicated the photo-induced charge transfer in our complex system, while the existence of long-lived charge separated states is under exploration. The success of obtaining single crystal of **FP-Ph** gives us some insight to develop the infinite crystalline structures of fullerene-borate ionic complex through ionic interaction between two counter ions. We expect our fullerene-borate ionic complex will also have promising electrical and magnetic properties as some fullerene complexes reported previously.

TABLE OF CONTENTS

LIST OF FIGURES

LIST OF SCHEMES

LIST OF TABLES

LIST OF ABBREVIATIONS

1-D	One-dimensional
3-D	Three-dimensional
AFM	Atomic force microscopy
APPI	Atmospheric pressure photoionization
BET	Brunauer-Emmett-Teller
BHJ	Bulk heterojunction
Bu_4NPF_6	Tetrabutylammonium hexafluorophosphate
CB	Chlorobenzene
CF	Chloroform
CPs	Conjugated polymers
CV	Cyclic voltammetry
D-A	Donor-acceptor
DCM	Dichloromethane
DFT	Density functional theory
DMSO	Dimethyl sulfoxide
DSC	Differential scanning calorimetry
DSSCs	Dye-sensitized solar cells
eq.	Equivalent
EQE	External quantum efficiency
ETL	Electron transporting layer
EWG	Electron withdrawing group
Fc	Ferrocene

FET	Field-effect transistor
FF	Fill factor
FBTD	Fluorinated benzothiadiazole
HJ	Heterojuction
HOMO	Highest occupied molecular orbital
HRMS	High resolution mass spectrometry
ICT	Intra-molecular charge transfer
ITO	Indium tin oxide
J	Current density
J_m	Maximum current density
J_{SC}	Short circuit current density
LUMO	Lowest unoccupied molecular orbital
MDMO-PPV	Poly[2-methoxy-5-(3',7'-dimethyloctyloxy)-1,4-phenylenevinylene
MEH-PPV	Poly(2-methoxy-5-(2'-ethyl-hexyloxy)-1,4-phenylenevinylene
M_n	The number average molecular weight
M_w	The weight average molecular weight
NMR	Nuclear magnetic resonance
OSCs	Organic solar cells
P3DTV	Poly(3-decylthienylene vinylene)
P3HT	Poly(3-hexylthiophene)
PCBM	[6, 6]-Phenyl-C_{61}-butyric acid methyl ester
PCE	Power conversion efficiency
PDI	Polydipersity index

P_{in}	Power input
P_{out}	Power output
PPV	Phenylene vinylene
PSCs	Polymer solar cells
R_S	Series resistance
R_{SH}	Shunt resistance
SAED	Selected area electron diffraction
SMSCs	Small molecules solar cells
TEA	Triethylamine
TEM	Transmission electron microscopy
TD-DFT	Time dependent-density functional theory
TPA	Triphenylamine
UV-vis	Ultraviolet-visible
V	Volt
V_m	Maximum output voltage
V_{OC}	Open circuit voltage
wt	Weight
XRD	X-ray diffraction
δ	Chemical shift
λ	Wavelength

Chapter 1

Introduction

1.1 Overview

Nowadays, energy crisis has been a constantly-debated issue, which needs to be solved as soon as possible. It forces human beings to continuously search new energy sources to satisfy the increasing demands of energy. Currently, our major energy are generated by burning fossil fuels, usually causing air pollution and other environmental concerns such as global warming effect.[1] Another disadvantage of the fossil-based fuels is that they are non-renewable energy, which will be consumed completely in the foreseeable future. Therefore, it will be desired to find an energy source, which can be clean and renewable. Among all kinds of candidates, solar energy is considered as the most promising one, due to its abundance, clean and renewable nature.

In 2012, US Energy Information Administration reported that all the renewable energy sources only contributed 8% of the total US energy consumption in the year of 2011.[2] Compared with all other renewable alternatives, the solar energy is relatively less exploited, since it only contributes 2% of the overall renewable energy supplies. However, it's well-known that the sun shines on the earth can give a total energy of approximately 120 000 TW (1 TW = 1 × 1012 W), which is far more than human beings' actual needs.[3-4] Therefore, solar cell devices, which can directly convert solar energy into electricity, will be the best way to harness the abundant solar energy. At present, the commercialized solar cells are dominated by silicon-based inorganic solar cells, which have reached over 20% power conversion efficiencies (*PCE*s) down to the lab scale.[5] However, the high cost of fabrication and installation of inorganic solar cells prevents

their wide acceptance. Second generation solar cells such as dye-sensitized solar cells (DSSCs) [6-7] and organic solar cells (OSCs) including small molecules solar cells (SMSC)[8-9] and polymer solar cells (PSCs)[10-11] started to draw more and more attentions in recent years, due to their potentials to lower the costs.[12] On the other hand, OSCs are especially attractive, owing to their light-weight nature, flexibility and amenability to printing electronic techniques for massive production. The printing techniques including roll-to-roll processing and ink-jet printing are expected to further reduce the fabrication costs. At last, tailored chemical structures of organic materials give different functionalities, which allow synthetic chemists to modify the structures in order to obtain more desired properties.

1.2 Basic of Organic Solar cells

1.2.1 Development of OSCs

In 1985, Tang and his coworkers reported the first heterojunction organic solar cell.[13] They put the electron donor (p-type), electron acceptor (n-type) materials and silver electrode onto the ITO (Indium Tin Oxide) glass substrate by sequential vacuum deposition to fabricate a multilayer structure solar cell. In their solar cells, copper phthalocyanine was used as the electron donor materials, while perylenetetracarboxylic derivative was served as the electron acceptor materials, and finally about 1% efficiency was achieved. Regardless of low solar cell efficiency at that time, their work was a milestone for solar cell research, which started an era for the heterojunction solar cells. In 1995, Yu et al. reported a poly(2-methoxy-5-(2'-ethyl-hexyloxy)-1,4-phenylenevinylene) (MEH-PPV) and fullerenes solar cells by spin-coating the solutions of MEH-PPV and fullerenes blend together as active layer materials.[14] The solar cells' performance were

significantly improved when the active layer were prepared through blend solution by spin-coating method. At the same time, soluble fullerene derivatives came out, due to the great contribution of Wudl.[15] Phenyl-C_{61}-butyric acid methyl ester (PCBM) was employed to fabricate solar cells, making high fullerenes loadings become possible, owing to its good solubility in common organic solvents. More importantly, the formation of interpenetrating donor/acceptor network in the film resulted from spin-coating blend solution attributed to the improved photovoltaic properties. Since then, the concept of bulk heterojunction (BHJ) and fullerene derivatives such as PCBM were widely used as a popular strategy for the state-of-art organic solar cells. At the beginning of BHJ solar cells research, large bandgap and amorphous nature of polymers hindered further improvement of solar cell efficiencies. In recent years, transition metal catalyzed cross coupling reactions became the most popular methodology to achieve low bandgap molecules with extended light absorption ranges.[16-19] At the same time, more and more crystalline small molecules have been synthesized and employed in solar cells. So far, the efficiencies of OSCs have reached over 10%, owing to the sustainable efforts of several generations in the past decades.[20-21] However, the current efficiencies of OSCs are still the major concern to push OSCs become commercializable. Therefore, more efforts are still needed to push the PCE limit up to 15%.

1.2.2 Mechanism of OSCs

The mechanism of OSCs is depicted in Figure 1.1. The general working principle of OSCs first involves the photoexcitation of the donor material by absorption of light energy to generate excitons. This Coulombically bound electron-hole pair, the so-called exciton, diffuses to the donor-acceptor (D-A) interface where exciton dissociation occurs

via an electron-transfer process. The fully separated free charge carriers transport to the respective electrodes in the opposite direction with the aid of the internal electric field, which in turn generates the photocurrent and photovoltage.[16]

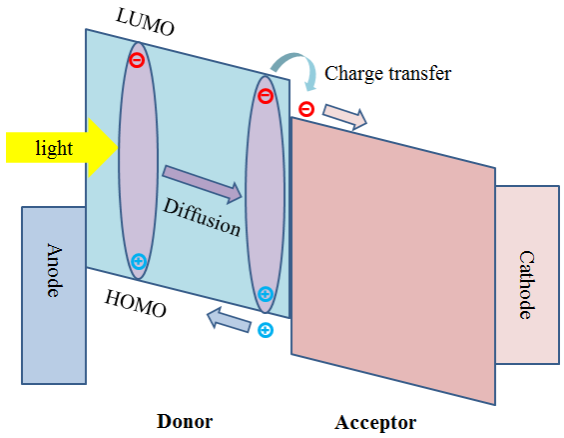

Figure 1.1 Working mechanism of OSCs.

1.2.3 General Architectures of OSCs

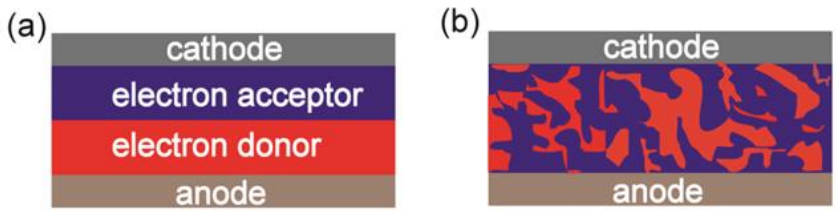

Figure 1.2 Conventional structure of HJ solar cell: **a.** bilayer; **b.** bulk heterojunction

As mentioned in previous section, two general architectures have been developed for OSCs, the bilayer heterojunction (HJ) structure and bulk heterojunction (BHJ) structure as showed in Figure 1.2.[22] Bilayer HJ structure was initially applied in OSCs. In this structure, two separate donor material layer and acceptor material layer are inserted between the two electrodes. However, the performance of solar cells fabricated by this architecture is limited by the life time or diffusion length of excitons. To overcome this difficulty, Yu et.al did the pioneering work by introducing the concept of BHJ.[23] In this

architecture, donor materials and acceptor materials are mixed together to form a bulk blend film by either spin-coating the blend solution or co-deposition at low vacuum.

1.2.4 Important Parameters of OSCs

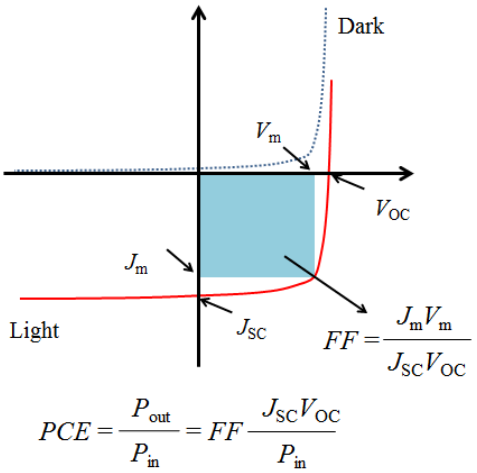

Figure 1.3 I-V curve and parameters in OSCs

The efficiency of OSCs is called power conversion efficiency (*PCE*), which can be obtained by measuring the I-V curve under simulated sunlight illumination, as shown in Figure 1.3.[24-25] Meanwhile, its value can be calculated through the following equation: $PCE = (V_{OC}*J_{SC}*FF)/P_{in}$. V_{OC} refers to open-circuit voltage, which is proportional to the built-in voltage between the LUMO of the acceptor and the HOMO of the donor.[26] J_{SC} is the short-circuit current, which is related to the amount of absorbed photons, the efficiency of the exciton dissociation, and separation of geminate excitons and the charge mobilities in the active layer.[27] *FF* stands for fill factor, which can be calculated through $FF = (V_m*J_m)/(V_{OC}*J_{SC})$ and is sensitive to the morphology of the device active layer.[28-29] P_{in} is the power input of the incident light, calculated from the power density and active device area. R_{SH} stands for shunt resistance, which can reflect the current leakage of devices due to recombination. R_S stands for series resistance, which comes from four

aspects: (1) bulk resistance of the active layer and kinds of functional layers in the film, (2) bulk resistance of the electrodes, (3) contact resistance of every interface in the device and (4) probe resistance. In simplified equivalent circuit model of solar cell showed in Figure 1.4 (left), large R_S of devices will decrease the V_{OC} of solar cell, while small R_{SH} of devices will lower the J_{SC} of solar cell. R_{SH} and R_S can be calculated from J-V curves, which also can be used to estimate the quality of devices. In Figure 1.4 (right), it shows the effect of diverging R_{SH} and R_S from ideality, which significant decreases the FF.

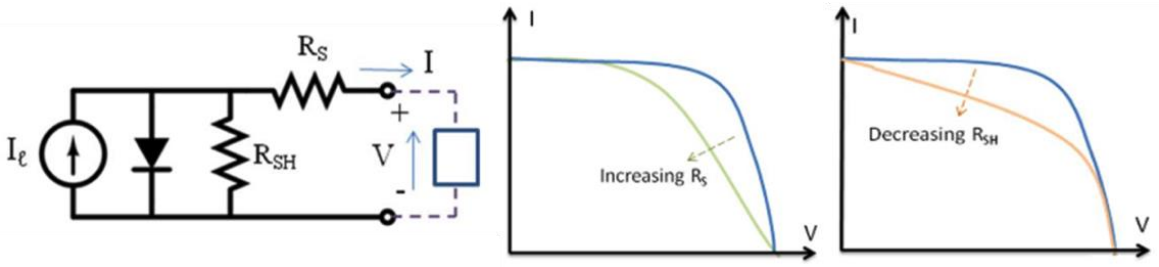

Figure 1.4 Simplified equivalent circuit model of solar cell (left) and effect of diverging R_S and R_{SH} from ideality (right).[30]

1.2.5 Morphology Control of OSCs

The efficiency of photoexcition induced exciton diffusion to the donor/acceptor interface is one of the key factors to determine the solar cell performance. The lifetime of excitons in typical conjugated molecules is very short, which only allows them to travel no more than 20 nm before they recombine and lose energy in the form of heat or luminescence.[31-33] Thus, in order to improve the exciton separation efficiency and the overall efficiencies of organic solar cells, it's very important to have a good morphology control of the donor/acceptor blends, which can lead to suitable domain sizes, interconnected charge transport pathways and good contacts with the electrodes and the interfacial layers. At present, several methodologies have been reported that can control

the morphology and eventually improve the efficiencies of devices.[34-37] These methodologies include solvents selection to dissolve the donors/acceptors mixtures, thermal annealing of devices, solvent vapor annealing, additives incorporation and the addition of third components.

A proper processing solvent not only could well dissolve both the donors and acceptors at the same time, but also could contribute to better phase separation during the film formation process after spin-coating. The evaporation rate of processing solvent could also play an important role, since the proper processing solvent is expected to modulate the crystallization speed of donors and acceptors to yield the optimal phase separation. Heeger and his coworkers[38] reported poly [N-9''-hepta-decanyl-2, 7-carbazole-alt-5, 5-(4', 7'-di-2-thienyl-2', 1', 3'-benzothiadiazole (PCDTBT) : $PC_{71}BM$ cells optimized by employing different processing solvents to yield an efficiency of 6.1%. They found that devices prepared from 1, 2-dichlorobenzene (DCB) outperformed those made from chloroform or chlorobenzene, owing to the slower evaporation rate of DCB, which gave more time for donors and acceptors to reach an ideal phase separation.

Thermal annealing has been demonstrated as an efficient methodology to improve the efficiencies of OSCs, which has already been widely used in research lab to enhance the devices performance.[39-41] In thermal annealing process, the OSCs devices are heated at a predetermined temperature for certain time and then spontaneously cool down to room temperature. Thus, the functions of thermal annealing were proposed to remove the solvent residue in the blend films to reduce the resistance, to promote phase separation of blend film by inducing the crystallization of donors or acceptors and improve the contacts between active layers and the metal electrodes.[42-43]

Solvent annealing has been proved as another efficient way to induce appreciable morphologies of blends by exposing the as-cast films with a specific solvent or their solvent vapors in a closed container.[44-48] The solvent or solvent vapor could lead to crystallization of donors or acceptors, which could further induce an optimal phase separation of blends in a slower manner.

Adding additives including solvent additives and non-solvent additives into blend solutions are both effective ways to improve the *PCE*s of organic solar cells. Bazan and his coworkers[49] found adding 5% (by volume) alkanethiol into the P3HT/PCBM system could significantly enhance the solar cell performance. Such method was applied to other low bandgap polymer/fullerene solar cells system, where higher efficiencies were also observed.[50] Since alkanethiols have higher boiling points than that of processing solvent, slower evaporation of such additive could slow down the crystallization of donors and acceptors, which lead to better phase separation. On the other hand, the alkanethiols could selectively dissolve fullerenes so that it could also change the phase separation behavior of the blends in order to obtain better morphology of the active layer. Besides alkanethiols, non-solvent additives including metal nanoparticles[51-52] and carbon nanotubes[53] etc. were also found that can improve the efficiencies of the organics solar cells.

1.3 Small Molecules Used in Solar Cells

1.3.1 Small Molecule Solar Cells

OSCs utilizing solution processable small molecules as donor materials in OSCs have made their debut in 2000.[54] Compared with their polymer counterparts, they are more repeatable in synthesis and offer easier processing in devices fabrication.[55-56] The

PCE of solution processable small molecules have steadily improved over the past decade from 0.03 % to over 10.0 %, due to sustainable efforts towards the development of new small molecules.[57-66] Significant progress has been made in the synthesis and design of donor–acceptor (D-A) small molecules, including oligothiophenes, star, or X shaped molecules, linear analogs with donor-acceptor-donor structures, triphenylamine and diketopyrrolppyrrole containing organic molecules and other low band gap organic dyes. The D-A small molecules were considered as efficient donor materials for OSCs due to their several key advantages: (1) the absorption spectrum of the D-A molecules can be extended towards longer wavelength by intra-molecular charge transfer (ICT) transition between donor and acceptor units inside molecules and, (2) the energy level can be easily controlled by introducing various electron donating or acceptor groups into the molecules.[67]

1.3.2 Molecular Tetrapods in OSCs

Current research on small molecule solar cells mainly focuses on linear small molecules. Most of current high efficient small molecules solar cells come from linear structure small molecules, while multi-dimensional molecules are still under development. In theory, low dimensionality of organic semiconductors based on linear π-conjugated systems results in the anisotropy of their charge-transport and optical properties which lowers the performance of solar cells. Thus, whereas a vertical orientation of the conjugated chains on the substrate improves mobility in organic field-effect transistors, such an orientation is detrimental for solar cells as it strongly reduces the absorption of the incident light as well as charge transport to the electrodes.[68] In an attempt to solve this problem, Roncali has done the pioneer work in the development of

three-dimensional (3-D) conjugated architectures based on triphenylamine (TPA) and silicon hybrid oligothiophenes for OSCs. The amorphous donor materials resulted by 3-D architecture combining core with linear π-conjugated system arms showed better performance than that of one-dimensional (1-D) linear π-conjugated donor materials due to isotropic optical and charge-transporting properties associated with 3-D geometry.[69]

1.4 Motivation of My Project

TPA-oligothiophene hybrid systems as shown in Figure 1.5, S(TPA-hTT) displayed a high hole mobility up to 1.1×10^{-2} cm^2 V^{-1} s^{-1} obtained though field-effect transistor testbed.[70] Based on S(TPA-hTT)，Y. F. Li and X. W. Zhan et.al replaced the hexyl group by 2-ethyl-hexyl cyano acetate to get a new star-shaped molecule and used as donor materials to yield a high *PCE* 3.60%.[71] This preliminary work demonstrates that multidimensional oligothiophenes end-capped with alkyl cyanoacetate groups may be promising donors for solution-processed OSCs. In 2006, Roncali et.al firstly synthesized the tetrapodal architectures involving four oligothiophenes chains attached to a silicon node S(2-hsTT) in Figure 1.5 (right) represent interesting donor materials.[72]

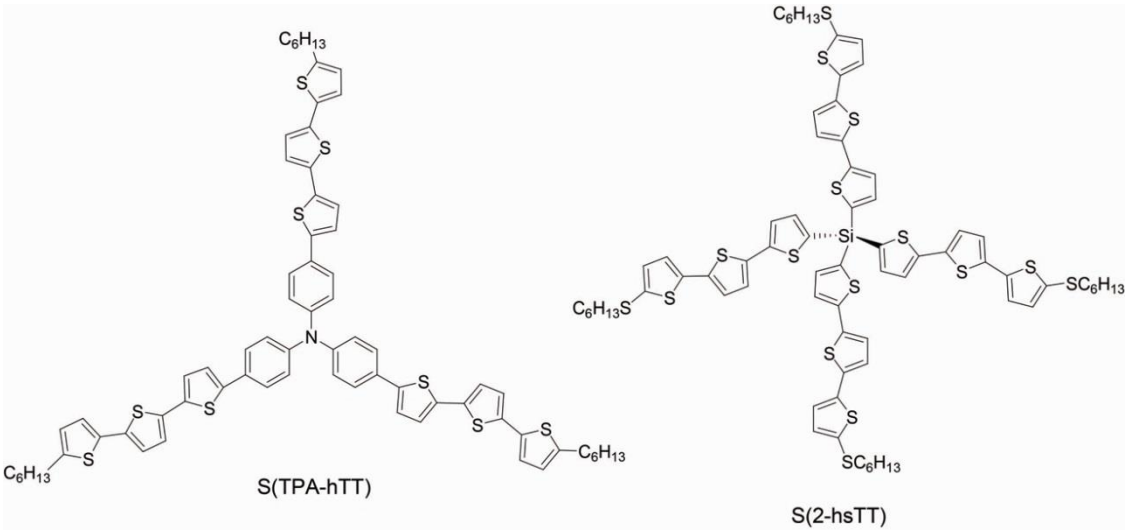

Scheme 1.1 Chemical structure of S(TPA-hTT) (left) and S(2-hsTT) (right).

However, S(2-hsTT) used as donor materials in either bilayer or bulk heterojunction structure didn't show good performance limited by the poor absorption among the visible light and poor phase separation with acceptor materials. Here we designed and synthesized tetrapodal, D-A molecules **S-EWG** shown in Figure 1.6 by using tetraphenylsilane as center, oligothiophenes as arm and electron deficient unit as acceptor unit. Stable tetraphenylsilane could avoid forming unstable cation radicals with a break of carbon-silicon bond in order to maintain the 3-D geometry of molecule. Oligothiophenes were introduced to extend the conjugated length of molecules in order to increase the absorption of molecules and also ensure the solubility of precursor molecules. Varied electron withdrawing group were used to tune the energy level and also adjust the solubility of target molecules. We expect these molecules will have good thermal stability, solution processability, broad and strong absorption in visible light range, appropriate energy level and high hole mobility with 3-D geometry architecture.

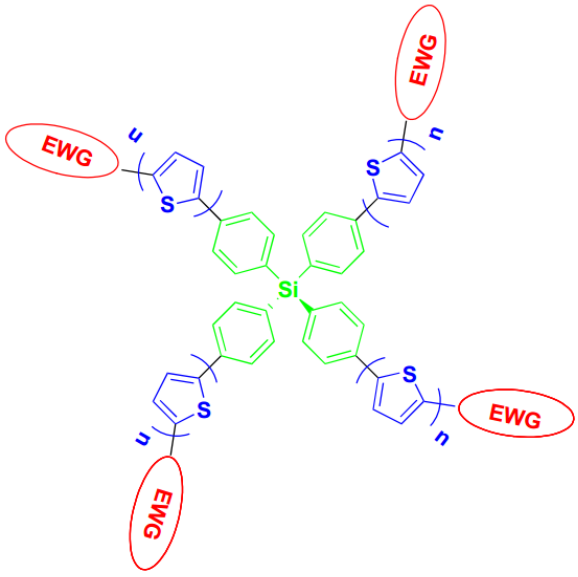

Figure 1.5 Chemical structure of proposed molecular tetrapods **S-EWG**, EWG stands for electron withdrawing group.

1.5 References

(1) Armaroli, N.; Balzani, V. *Angew. Chem., Int. Ed.* **2007**, 46, 52.

(2) US Department of Energy, *Annual Energy Review 2011*, Washington, DC; www.eia.doe.gov/emeu/aer.

(3) Krebs, F. C. In *Polymer photovoltaics: a practical approach*; SPIE press Bellingham: **2008**, p 175.

(4) Delgado, J. L.; Bouit, P. A.; Filippone, S.; Herranz, M. A.; Martin, N. *Chem. Commun.* **2010**, 46, 4853.

(5) Zhao, J.; Wang, A.; Green, M. A.; Ferrazza, F. *Appl. Phys. Lett.* **1998**, 73, 1991.

(6) Grätzel, M. *J. Photochem. Photobiol. C: Photochem. Rev.* **2003**, 4, 145.

(7) Hagfeldt, A.; Boschloo, G.; Sun, L.; Kloo, L.; Pettersson, H. *Chem. Rev.* **2010**, 110, 6595.

(8) Lin, Y.; Li, Y.; Zhan, X. *Chem. Soc. Rev.* **2012**, 41, 4245.

(9) Mishra, A.; Bäuerle, P. *Angew. Chem., Int. Ed.* **2012**, 51, 2020.

(10) Günes, S.; Neugebauer, H.; Sariciftci, N. S. *Chem. Rev.* **2007**, 107, 1324.

(11) Zhan, X.; Zhu, D. *Polym. Chem.* **2010**, 1, 409.

(12) Kalowekamo, J.; Baker, E. *Sol. Energy* **2009**, 83, 1224.

(13) Tang, C. W. *Appl. Phys. Lett.* **1986**, 48, 183.

(14) Yu, G.; Gao, J.; Hummelen, J. C.; Wudl, F.; Heeger, A. J. *Science* **1995**, 270, 1789.

(15) Hummelen, J. C.; Knight, B. W.; LePeq, F.; Wudl, F.; Yao, J.; Wilkins, C. L. *J. Org. Chem.* **1995**, 60, 532.

(16) Cheng, Y.-J.; Yang, S.-H.; Hsu, C.-S. *Chem. Rev.* **2009**, 109, 5868.

(17) Chen, J.; Cao, Y. *Acc. Chem. Res.* **2009**, 42, 1709.

(18) Beaujuge, P. M.; Fréchet, J. M. J. *J. Am. Chem. Soc.* **2011**, 133, 20009.

(19) Zhou, H.; Yang, L.; You, W. *Macromolecules* **2012**, 45, 607.

(20) He, Z.; Zhong, C.; Su, S.; Xu, M.; Wu, H.; Cao, Y. *Nat. Photon.* **2012**, 6, 591.

(21) You, J.; Chen, C.-C.; Hong, Z.; Yoshimura, K.; Ohya, K.; Xu, R.; Ye, S.; Gao, J.; Li, G.; Yang, Y. *Adv. Mater.* **2013**, 25, 3973.

(22) Kietzke, T. *Adv. OptoElectron*. **2007**, 1, 40285.

(23) Sariciftci, N. S.; Smilowitz, L.; Heeger, A. J.; Wudl, F. *Science* **1992**, 258, 1474.

(24) Brabec, C. J.; Hauch, J. A.; Schilinsky, P.; Waldauf, C. *MRS Bull.* **2005**, 30, 50.

(25) Brabec, C. J. *Sol. Energy Mater. Sol. Cells* **2004**, 83, 273.

(26) Topham, P. D.; Parnell, A. J.; Hiorns, R. C. *J. Polym. Sci., Part B: Polym. Phys.* **2011**, 49, 1131.

(27) Jørgensen, M.; Norrman, K.; Krebs, F. C. *Sol. Energy Mater. Sol. Cells* **2008**, 92, 686.

(28) Gupta, D.; Mukhopadhyay, S.; Narayan, K. S.; *Sol. Energy Mater. Sol. Cells* **2010**, 94, 1309.

(29) Tomoya, H.; Mitsuru, U.; *Macromolecular Research* **2013**, 21, 257.

(30) Http://www.ni.com/white-paper/7230/en/

(31) Brédas, J.-L.; Norton, J. E.; Cornil, J.; Coropceanu, V. *Acc. Chem. Res.* **2009**, 42, 1691.

(32) Halls, J. J. M.; Pichler, K.; Friend, R. H.; Moratti, S. C.; Holmes, A. B. *Appl. Phys. Lett.* **1996**, 68, 3120.

(33) Stübinger, T.; Brütting, W. *J. Appl. Phys.* **2001**, 90, 3632.

(34) Slota, J. E.; He, X.; Huck, W. T. S. *Nano Today* **2010**, 5, 231.

(35) Yang, X.; Loos, J. *Macromolecules* **2007**, 40, 1353.

(36) Chen, L.-M.; Hong, Z.; Li, G.; Yang, Y. *Adv. Mater.* **2009**, 21, 1434.

(37) Van Bavel, S.; Veenstra, S.; Loos, J. *Macromol. Rapid Commun.* **2010**, 31, 1835.

(38) Park, S. H.; Roy, A.; Beaupre, S.; Cho, S.; Coates, N.; Moon, J. S.; Moses, D.; Leclerc, M.; Lee, K.; Heeger, A. J. *Nat. Photon.* **2009**, 3, 297.

(39) Kim, Y.; Choulis, S. A.; Nelson, J.; Bradley, D. D. C.; Cook, S.; Durrant, J. R. *Appl. Phys. Lett.* **2005**, 86, 063502.

(40) Ma, W.; Yang, C.; Gong, X.; Lee, K.; Heeger, A. J. *Adv. Funct. Mater.* **2005**, 15, 1617.

(41) Padinger, F.; Rittberger, R. S.; Sariciftci, N. S. *Adv. Funct. Mater.* **2003**, 13, 85.

(42) Dang, M. T.; Hirsch, L.; Wantz, G.; Wuest, J. D. *Chem. Rev.* **2013**, 113, 3734.

(43) Liu, F.; Gu, Y.; Jung, J. W.; Jo, W. H.; Russell, T. P. *J. Polym. Sci., Part B: Polym. Phys.* **2012**, 50, 1018.

(44) Li, G.; Yao, Y.; Yang, H.; Shrotriya, V.; Yang, G.; Yang, Y. *Adv. Funct. Mater.* **2007**, 17, 1636.

(45) Li, G.; Shrotriya, V.; Huang, J.; Yao, Y.; Moriarty, T.; Emery, K.; Yang, Y. *Nat. Mater.* **2005**, 4, 864.

(46) Mihailetchi, V. D.; Xie, H.; De Boer, B.; Popescu, L. M.; Hummelen, J. C.; Blom, P. W. M.; Koster, L. J. A. *Appl. Phys. Lett.* **2006**, 89, 012107.

(47) Shrotriya, V.; Yao, Y.; Li, G.; Yang, Y. *Appl. Phys. Lett.* **2006**, 89, 063505.

(48) Tang, H.; Lu, G.; Li, L.; Li, J.; Wang, Y.; Yang, X. *J. Mater. Chem.* **2010**, 20, 683.

(49) Peet, J.; Soci, C.; Coffin, R. C.; Nguyen, T. Q.; Mikhailovsky, A.; Moses, D.;

Bazan, G. C. *Appl. Phys. Lett.* **2006**, 89, 252105.

(50) Peet, J.; Kim, J. Y.; Coates, N. E.; Ma, W. L.; Moses, D.; Heeger, A. J.; Bazan, G. C. *Nat. Mater.* **2007**, 6, 497.

(51) Kim, K.; Carroll, D. L. *Appl. Phys. Lett.* **2005**, 87, 203113.

(52) Naidu, B. V. K.; Park, J. S.; Kim, S. C.; Park, S.-M.; Lee, E.-J.; Yoon, K.-J.; Joon Lee, S.; Wook Lee, J.; Gal, Y.-S.; Jin, S.-H. *Sol. Energy Mater. Sol. Cells* **2008**, 92, 397.

(53) Berson, S.; de Bettignies, R.; Bailly, S.; Guillerez, S.; Jousselme, B. *Adv. Funct. Mater.* **2007**, 17, 3363.

(54) Petritsch, K.; Dittmer, J. J.; Marseglia, E. A.; Friend, R. H.; Lux, A.; Rozenberg, G. G.; Moratti, S. C.; Holmes, A. B. *Sol. Energy Mater. Sol. Cells.* **2000**, 61, 63.

(55) Lloyd, M. T.; Anthony, J. E.; Malliaras, G. G. *Mater. Today*, **2007**,10, 34.

(56) Rand, B. P.; Genoe, J.; Heremans, P.; Poortmans, J. *Progr. Photovolt. Res. Appl.* **2007**, 15, 659.

(57) Walker, B.; Tamayo, A. B.; Dang, X.D.; Zalar, P.; Seo, J. H.; Garcia, A.; Tantiwiwat, M.; Nguyen, T. Q. *Adv. Funct. Mater.*, **2009**, 19, 3063.

(58) Mikroyannidis, J. A.; Stylianakis, M. M.; Suresh, P.; Balraju, P.; Sharma, G. D. *Org an. Electron.*, **2009**, 10, 1320.

(59) Sharma, G. D.; Balraju, P.; Mikroyannidis; J. A.; Stylianakis, M. M. *Sol. Energy Mater. Sol. Cells*, **2009**, 93, 2025.

(60) Tamayo, A. B.; Walker, B.; Nguyen, T. Q. *J. Phys. Chem.C* **2008**, 112, 1154.

(61) Tamayo, A. B.; Dang, X. D.; Walker, B.; Seo, J.; Kent, T.; Nguyen, T. Q. *Appl. Phys. Lett.*, **2009**, 94, 103301.

(62) Sharma, G. D.; Suresh, P.; Mikroyannidis; J. A.; Stylianakis, M. M. *J. Mater. Chem.*,

2010, 20, 561.

(63) Mikroyannidis, J. A.; Suresh, P.; Sharma, G. D. *Synth. Met.* **2010**, 160, 932.

(64) Mikroyannidis, J. A.; Kabanakis, A. N.; Tsagkournos, D. V.; Balrajubd, P.; Sharma, G. D. *J. Mater. Chem.*, **2010**, 20, 6464.

(65) Mikroyannidis, J. A.; Stylianakis, M. M.; Balraju, P.; Suresh, P.; Sharma, G. D. *ACS Appl. Mater. Interfaces* **2009**, 1, 1711.

(66) Zhou, J. Y.; Zuo, Y.; Wan, X. J.; Long, G. K.; Zhang, Q.; Ni, W.; Liu, Y. S.; Li, Z.; He, G. R.; Li, C. X.; Kan, B.; Li, M. M.; Chen, Y. S. *J. Am. Chem. Soc.* **2013**, 135, 8484.

(67) Sharma, G. D. *AIP Conf. Proc.* **2011**, 42, 1391.

(68) Videlot, C.; El Kassmi, A.; Fichou, D.; *Sol. Energy Mater. Sol. Cells* **2000**, 63, 69.

(69) Ning, Z. Tian, H. *Chem. Commun.*, **2009**, 37, 5483.

(70) Cravino, A.; Roquet, S.; Aleveque, O.; Leriche, P.; Frere, P.; Roncali, J. *Chem. Mater.* **2006**, 18, 2584.

(71) Lin, Y. Z.; Zhang, Z.-G.; Bai, H. T.; Li, Y. F.; Zhan, X. W. *Chem. Commun.* **2012**, 48, 9655.

(72) Roncali, J.; Frere, P.; Blanchard, P.; de Bettignies, R.; Turbiez, M.; Roquet, S.; Leriche, P.; Nicolas, Y. *Thin Solid Films*, **2006**, 567, 511.

Chapter 2

A Molecular Breakwater-Like Tetrapod for Organic Solar Cells

(Reproduced with permission from

Journal of Materials Chemistry A **2015**, 3, 2108 - 2119.

Copyright © The Royal Society of Chemistry 2015.

The other authors, Wenhan He, Kimberly Denman and Ying-Bing Jiang, are acknowledged.

Supporting information of the publication is incorporated in this chapter)

2.1 Introduction

Organic solar cells (OSCs) are considered a promising low-cost renewable energy source.[1-2] Research efforts in OSCs have been exclusively focused on conjugated polymers (CPs) owing to the device favorable processability and thin film forming ability, as well as the versatility in structure/property variations through well-established chemical transformations.[3-5] As a result, power conversion efficiencies (*PCE*s) of polymer solar cell (PSC) devices have been steadily increased to approach 10% in recent years.[6-13] CPs are typically synthesized through cross-coupling reactions in step-growth fashions that unavoidably generate materials with large distributions of molecular weights and frequently encountered structural defects. Control over this type of polymerization is poor, which commonly leads to batch-to-batch and lab-to-lab variations in polymer structures and properties. Most CPs applied in efficient PSCs have been found to be amorphous and thus possess relatively low charge mobilities. These aspects can potentially limit materials mass production and impede further device improvement. On the other hand, conjugated small molecules can be highly crystalline and thus have

superior charge mobilities, and at the same time have discrete and reproducible molecular structures.[14-22] These features have attracted increasing attention and bulk heterojunction (BHJ) OSCs devices employing conjugated small molecules and fullerene derivatives have been constantly improved to rival their CP counterparts, showing great promises in solar cell research.[23-30]

Most small molecules applied in solar cells have linear structures containing multiple aromatic groups connected in series. These molecules are typically highly crystalline and conductive along the π-stacking direction. However, charge migration along both long and short molecular axes are relatively limited due to the one-dimensional (1-D) nature of these molecules. Unfavorable film forming ability and grain boundaries both originated from high crystallinity of linear molecules are also detrimental to device performances. As a result, significant attention has been paid to conjugated small molecules having conjugation extended in three dimensions (3-D).[22] Such molecular design can increase absorption cross-sections and provide more extensively percolating pathways for charge transport. Among the many 3-D structures, breakwater-like tetrapods are especially interesting owing to their unique ability to mutually interlock, which prevents dislodging and provides high structural stabilities. This concept has been frequently applied in inorganic nanocrystal synthesis and the size scales of resulting tetrapods are on the order of hundred nm.[31-33] On the other hand, organic molecular tetrapods are less common in OSCs research.

Roncali *et al*. reported the synthesis of two tetrapodal molecules, each containing a silicon core and four terthiophene arms bearing alkyl and thioalkyl side chains, respectively.[34] The overall solar cell performances were significantly limited by the large

bandgaps of these tetrapods, but still out-performed the devices employing corresponding linear counterparts having structures of one of the four arms. Köse *et al*. recently reported low bandgap tetrapodal molecules composed of a silicon core and four arms composed of thiophene and benzothiadiazole units.[35] Favorable impact of high dimensionality of these molecules on charge mobility in disordered media was discovered. In both of these examples, the molecular tetrapods all contain silicon atoms as the cores that are connected to four thiophene rings. Owing to the electron rich character and relatively small sizes of thiophene rings, the silicon centers are more exposed and the silicon-thiophene bonds are relatively weak. This instability can potentially complicate compound synthesis and characterization, as well as reduce device operation lifetimes.[36] On the other hand, tetraphenylsilane is a commercially available compound and known to be robust under various reaction conditions, and is thus a better starting point to construct the molecular tetrapods. Herein, we report the synthesis, characterization and application in OSCs of a stable low bandgap breakwater-like tetrapod containing a tetraphenylsilane core and four cyanoester functionalized terthiophene arms.

2.2 Synthesis and Characterization

2.2.1 Synthesis of SO and MO

Detailed synthetic procedures for the tetrapodal molecule **SO**, and a model compound **MO** that represents a single arm of the tetrapod, are shown in Scheme 2.1. Compound **1** was prepared from commercial 1,4-dibromobenzene through lithium halogen exchange followed by reaction with 0.20 equivalents of $SiCl_4$. Compound **1** can be conveniently applied as a common core for grafting with different arms toward 3-D tetrapodal molecules. After Stille coupling reaction with **10** followed by acetal

deprotection, the tetra-aldehyde compound **11** was obtained. The aldehyde groups can be transformed to several strongly electron withdrawing substituents, *e.g.*, dicyanovinyl and cyanoester groups. However, **11** was found to have very limited solubility in common OSC processing solvents including chlorobenzene and dichlorobenzene. We thus chose *n*-octyl cyanoacetate (**12**) to impart the electron deficient moiety as well as sufficient solubility. Indeed, after the simple Knoevenegal-type condensation reaction, compound **SO** was obtained in high yields and has good solubility in a wide range of organic solvents including $CHCl_3$, THF and chlorobenzene. All compounds are fully characterized by ^{1}H and ^{13}C NMR spectroscopy, which agree well with proposed structures (Supporting Information). High resolution mass spectrometry (HR-MS) was attempted to confirm the tetra-arm structures of the newly synthesized compounds. Unfortunately, **SO** could not be ionized under current experimental conditions and no meaningful mass signals could be observed. Instead, HR-MS was performed on the precursor **11**. The measured molar masses (1768.3419 [M^+] and 1791.3317 [$M+Na^+$]) match perfectly with the calculated values (1768.3414 [M^+] and 1791.3312 [$M+Na^+$]), confirming the proposed tetrapodal structures of **11** and consequently of **SO**.

Scheme 2.1 Synthesis of **SO** and **MO.**

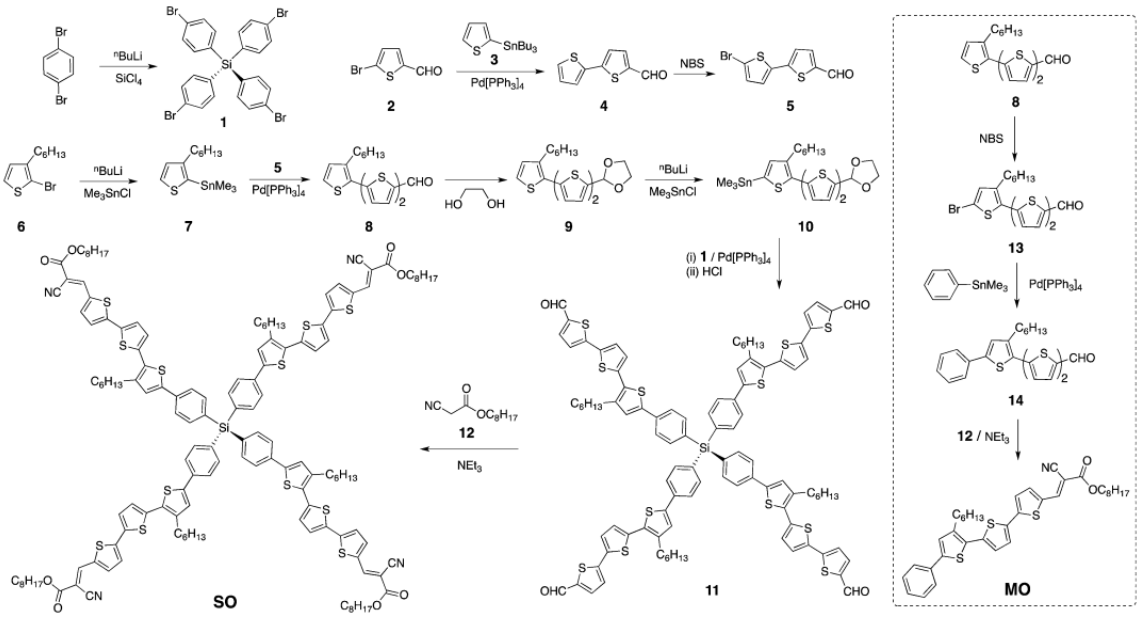

2.2.2 UV-vis Absorption and Fluorescence Spectroscopies

The electronic properties of **SO** and **MO** were investigated by UV-vis absorption and fluorescence spectroscopies in both dilute solutions and as thin films. As shown in Figure 2.1, both **SO** and **MO** in chlorobenzene solutions (10^{-5} M) display nearly identical structureless absorption profiles with λ_{max}'s at ca. 470 nm. The solution fluorescence spectra of both compounds are also indistinguishable with λ_{em}'s at ca. 595 nm. Such similarity in absorption and emission spectra indicates that there is no electronic communication among the four conjugated arms of **SO** when intermolecular interactions are negligible in dilute solutions. This is understandable since these four arms are stretched out away from one another in a tetrahedral geometry, which are connected through a non-conjugated silicon core. However, owing to the differences in molecular shapes, **MO** and **SO** show very different spectra in thin films. The as-cast thin film of **SO** displays a λ_{max} at ca. 570 nm, which is red-shifted from that of the solution profile by 100 nm. This red-shift in absorption is commonly observed in conjugated systems due to structural planarization and intermolecular interactions in the solid state. The

fluorescence of **SO** films is very weak, having a λ_{em} at ca. 625 when excited at the λ_{max}, which gives a relatively small Stoke's shift of 55 nm. On the contrary, the main absorption peak of **MO** is slightly blue-shifted to ca. 445 nm in thin films, indicating H-type aggregation of the molecules.[37] A low energy shoulder peak at ca. 530 nm is also observed, which is likely originated from new species due to aggregation. Emission of **MO** films is expectedly quenched to a large extent and only a weak fluorescence peaked at ca. 650 nm can be observed. From the absorption edges, the optical bandgaps of **SO** and **MO** are estimated to be both ca. 2.2 eV in solutions and 1.9 eV and 2.0 eV in thin films, respectively.

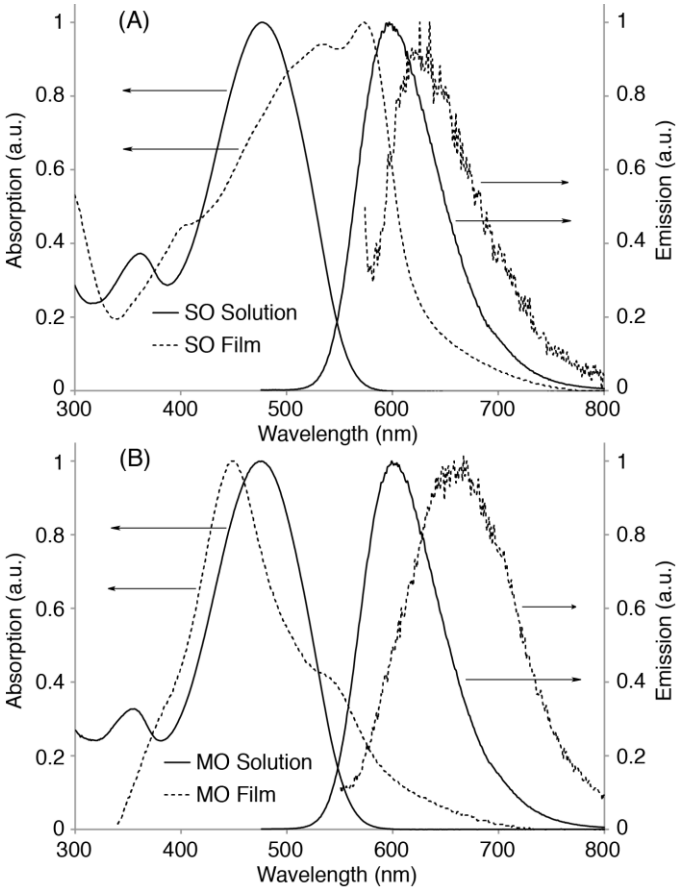

Figure 2.1 Normalized UV-vis absorption and emission spectra of (A) **SO** and (B) **MO** in chlorobenzene solutions (10^{-5} M, solid lines) and as thin films (dashed lines).

2.2.3 Cyclic Voltammetry Measurements

In order to quantify the frontier energy levels and bandgaps, cyclic voltammetry (CV) measurements were performed on **SO** and **MO** in dichloromethane solutions (1 mM). A glassy carbon working electrode, a Ag/AgCl reference electrode and a Pt wire counter electrode were used. Tetrabutylammonium hexafluorophosphate (Bu_4NPF_6, 0.1 M) was used as the supporting electrolytes. The recorded CV curves were externally referenced to ferrocene/ferrocenium (Fc/Fc^+) redox couple (4.80 eV below vacuum). Therefore, the HOMO and LUMO energy levels can be estimated using the empirical formula $E_{HOMO} = -(E_{ox}^{onset} + 4.80)$ eV and $E_{LUMO} = -(E_{red}^{onset} + 4.80)$ eV, respectively. As shown in Figure 2.2, both **SO** and **MO** displayed nearly identical redox behaviors. Two quasi-reversible oxidation peaks and one irreversible reduction peak, at onsets of ca. 0.4 V, 1.0 V and −1.5 V, respectively, were observed. As a result, the HOMO and LUMO levels of **SO** and **MO** were estimated to be –5.2 eV and –3.3 eV. This leads to an electrochemical bandgap of ca. 1.90 eV for both **SO** and **MO**, agreeing well with the results of optical measurements.

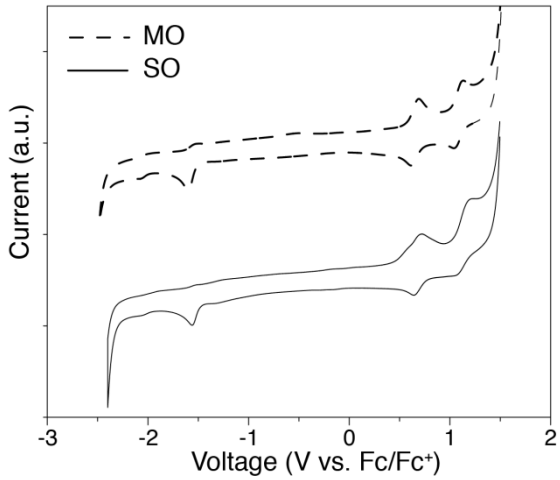

Figure 2.2 Cyclic voltammograms of MO and SO in CH_2Cl_2 solutions (1 mM) containing Bu_4NPF_6 as the supporting electrolytes (0.1 M). The voltages are referenced externally to ferrocene (Fc) redox couple. Scan rate: 100 mV/s.

2.2.4 DSC Measurements of SO and MO

Thermal properties of **SO** and **MO** were studied by using differential scanning calorimatry (DSC) measurements and the results are displayed in Figure 2.3. At a typical scanning rate of 10 °C/min, **SO** shows an exothermic crystallization transition peaked at 115 °C and two closely spaced melting transitions at 180 °C and 188 °C. No crystallization event is observed in the cooling curve. At a slower scanning rate of 1 °C/min, the crystallization transition is only observed during the cooling event at ca. 105 °C. Such behavior indicates slow crystallization kinetics of the compound and similar properties were previously reported for a linear conjugated small molecule having two specifically designed structural twists.[38] We originally thought that the tetrapodal structure of **SO**, which can be considered to possess four structural twists in the molecule, is the leading cause for the slow crystallization behavior. However, the same trend is observed for **MO**. At a scanning rate of 10 °C/min, **MO** displays both a crystallization (35 °C) and a melting transitions (68 °C) in the heating event while the crystallization transition (24 °C) is only observed upon cooling when the scanning rate is reduced to 1 °C/min. This indicates that the slow crystallization behavior of **SO** may be intrinsically resulted from the structure of each of its arms as demonstrated in the case of **MO**.

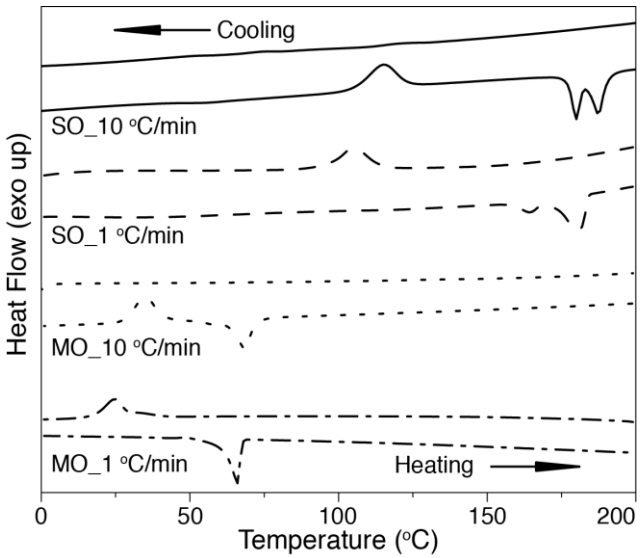

Figure 2.3 Differential scanning calorimetry (DSC) histograms of **SO** at a scanning rate of 10 °C/min (solid line) and at 1 °C/min (dashed line); and of **MO** at 10 °C/min (dotted line) and at 1 °C/min (dash dotted line). Second heating (lower segments) and cooling (upper segments) curves are shown.

2.2.5 DFT Calculation of MO

In order to gain a deeper insight on the structural origin of these thermal behaviors, we performed density functional theory (DFT) calculations (B3LYP/6-31G*) on **MO** and the optimized geometries are shown in Figure 2.4. The calculated minimum energy structure of **MO** is not completely planar. Dihedral angles of 26° and 15° are found between the phenyl and alkylthienyl groups and between the alkylthienyl and the adjacent thienyl groups, respectively. These structural twists are likely responsible for inefficient molecular packing and thus slow crystallization kinetics. Also seen from calculation results, the HOMO orbital of **MO** is delocalized throughout the entire conjugation and the LUMO orbital is positioned toward the cyanoester side. Electronic transitions from HOMO to LUMO thus possess charge transfer characteristics as

expected. The HOMO level is calculated to be –5.3 eV, matching that from CV measurements, while the LUMO is over estimated to be −2.7 eV (Figure 2.4).

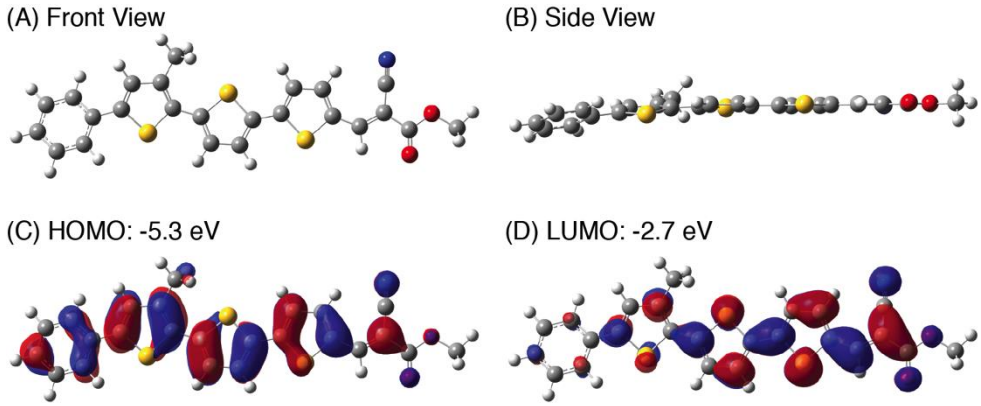

Figure 2.4 Density functional theory (DFT) calculation results (B3LYP/6-31G*) of **MO**.

2.2.6 Hole Mobilities of SO and MO Films

Hole mobilities in **SO** and **MO** films were estimated using space charge limited current (SCLC) method[39] in hole only devices having ITO/MoO_3 (10 nm)/organic/MoO_3 (10 nm)/Al (100 nm) geometries. The results are averaged from three devices with different organic layer thickness for each compound. The hole mobility of **SO** film is calculated to be ca. 1.8×10^{-4} cm^2/Vs, which is more than 100 times higher than that found for the **MO** film at 1.1×10^{-6} cm^2/Vs. The tetrahedral shape of **SO** likely leads to enhanced percolating pathways and thus improved charge mobilities, which is consistent with previous report.[35]

2.2.7 Wide-Angle X-ray Scattering of SO Thin Film

We have so far not been able to obtain high quality single crystals for **SO** in order for detailed X-ray analysis. DSC studies indicate certain crystallinity of the compound, which is further confirmed by thin film wide-angle X-ray scattering experiments as shown in Figure 2.5. Multiple scattering peaks are observed at 2θ values of ca. 4.0°, 5.7°, 8.1° and 12.3°, which correspond to *d*-spacings of ca. 2.2, 1.5, 1.1 and 0.7 nm,

respectively. Assignments of these scattering peaks are still not certain at present. The **SO** thin films were further studied by transmission electron microscopy (TEM) and selected area electron diffraction (SAED) measurements, and the results are summarized in Figure 2.6. Micron-sized ellipsoidal aggregates are randomly distributed throughout the film as seen in the TEM image. From the SAED image, only a few scattering rings can be observed and azimuthal integration of the major scattering ring gives a d-spacing of ca. 1.3 nm. The SAED pattern indicates that although there exists periodic structures in the **SO** films, the compound itself does not form conventional crystals ordered in three dimensions.

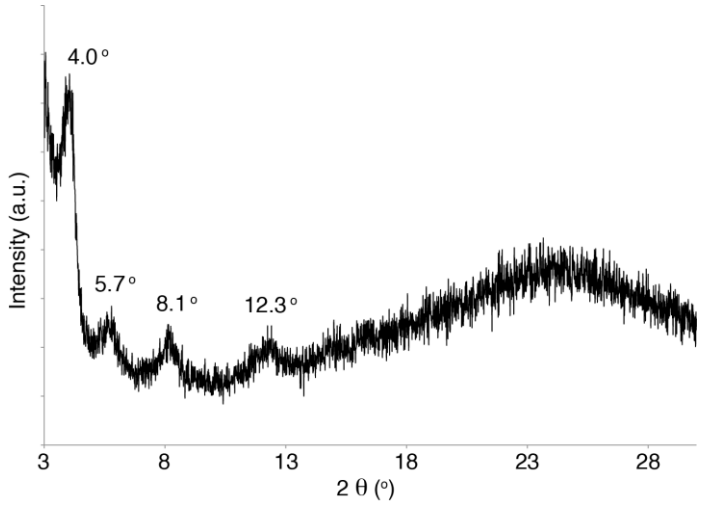

Figure 2.5 Wide-angle X-ray scattering profiles of **SO** thin films deposited on glass.

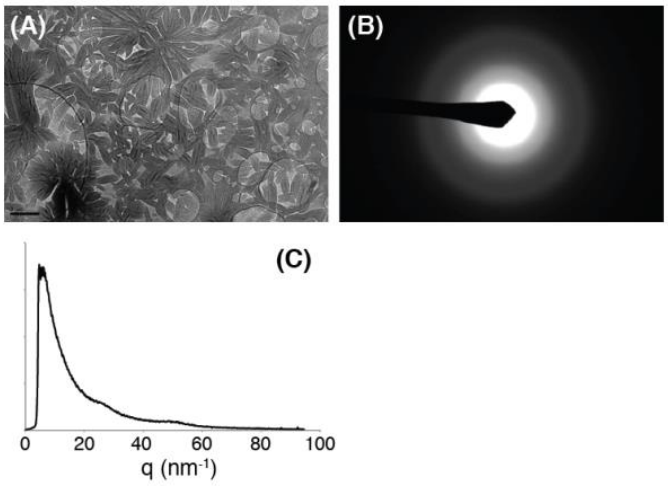

Figure 2.6 Transmission electron microscopy (TEM) image (A), selected area electron diffraction (SAED) images (B) and azimuthal integration curve of the SAED pattern (C) of as-cast **SO** thin films. Scale bar in A: 2 μm.

2.3 Binary Blend Devices

2.3.1 Binary Devices Performance

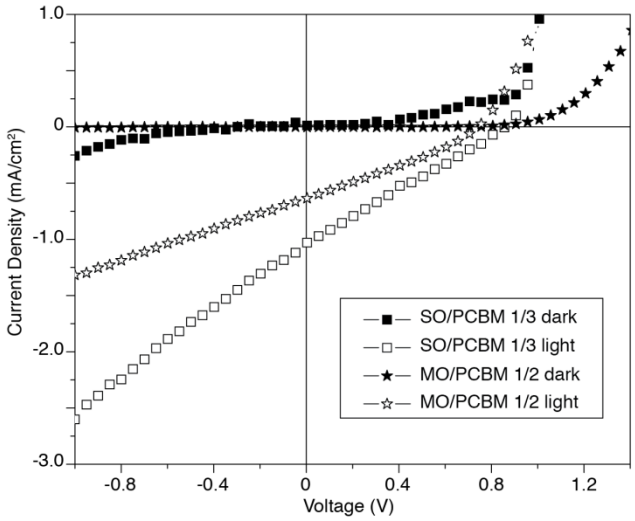

Figure 2.7 Current density-voltage (I-V) curves of solar cells employing **SO** or **MO** and PCBM in dark and under simulate solar light (100 mW/cm^2).

Solar cell devices were fabricated using conventional structures: ITO glass/MoO_3 (10 nm)/active layer (100 nm)/Al (100 nm). Mixtures of **SO** or **MO** and phenyl-C_{61}-butyric acid methyl ester (PCBM, American Dye Source, Inc.) at various weight ratios in chlorobenzene were spun cast to form the active layer. Thermal annealing at various temperatures was employed to optimize the device performances. The best *PCE*s were found in as-cast devices employing **SO**/PCBM at a weight ratio of 1/3, and **MO**/PCBM at a weight ratio of 1/2. Devices employing **SO** generally out-performed those using **MO** and the current density−voltage (I-V) curves of the best performing devices are shown in Figure 2.7. Both **SO** and **MO** devices show relatively high open circuit voltage (V_{OC})

values at 0.84 V and 0.74 V, respectively, which is consistent with the deep lying HOMO levels of these molecules. However both devices suffer greatly from low short circuit current (J_{SC}) and fill factor (*FF*) values. For instance, the **MO** device gives a J_{SC} of 0.64 mA/cm^2 and a *FF* of 30%, leading to *PCE* of 0.14%. While the **SO** device displays a J_{SC} of 1.01 mA/cm^2, a *FF* of 26% and the *PCE* of 0.22%. Steep increases in current densities at reverse bias are observed for both devices under light, which indicates significant charge recombination at short circuit conditions. Similar behaviors were observed by Köse *et al*. for their tetrapodal molecules, which they ascribed to inferior blend morphologies.[35] We thus studied the thin film morphologies of **SO**, **MO** and corresponding PCBM blends at optimal weight ratios for device operation by using optical microscopy and the photographs are included in Figure 2.8.

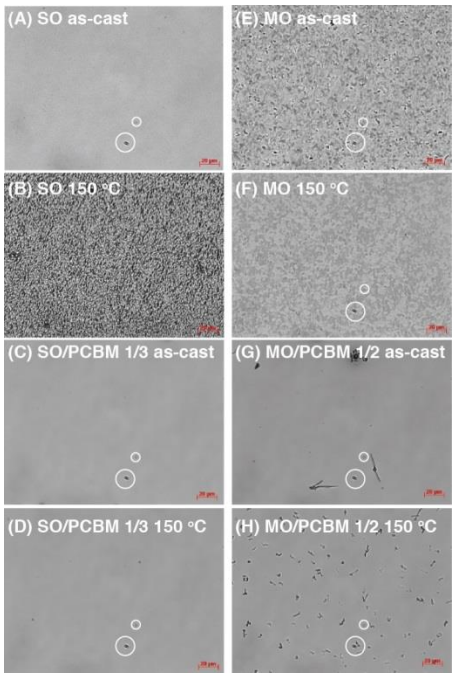

Figure 2.8 Optical micrographs (400 X magnificantion) of thin films of **SO**, **MO** and corresponding PCBM blends under different annealing conditions. Obvious artifacts are circled out in white. Scale bars in all: 20 μm.

2.3.2 Optics Images of Neat Films and Binary Blend Films

The as-cast **SO** thin films have smooth morphologies that are free of any visible aggregates or crystallites (Figure 2.8A). Annealing at 150 °C for 10 min leads to crystallization of **SO**, resulting in heavily textured morphology and dark crystallites as seen in Figure 2.8B. This observation is consistent with those from DSC studies and confirmed by cross-polarized light microscopy. As shown in Figure 2.9A,† no features can be observed in the as-cast **SO** thin films while annealing leads to heavily textured morphologies with relatively small feature sizes (Figure 2.9B). However, thin films containing **SO**/PCBM mixture at a 1/3 weight ratio do not display any phase separation (Figure 2.8C) even after annealing at 150 °C for 10 min (Figure 2.8D). It is likely that PCBM molecules are intercalated among the arms of **SO**, which effectively prevents crystallization of both **SO** and PCBM, and thus suppresses any appreciable phase separation within the blends. This lack of phase separation into pure domains of electron donors and acceptors can significantly limit charge transport and lead to large rates of charge recombination. On the other hand, **MO** thin films show slightly different behaviors. Clear and dense crystallites are observed in the as-cast films of **MO** (Figure 2.8E), which is not surprising since **MO** has a crystallization transition temperature around 25 °C. Annealing at 150 °C leads to still textured morphology with apparently less crystallites (Figure 2.8F). This trend is also confirmed by cross-polarized light microscopy. Crystals of **MO** can be cleared observed under cross-polarized light in as-cast films (Figure 2.9C), which become larger and less densely packed after thermal annealing (Figure 2.9D). As-cast thin films of **MO**/PCBM blends show overall smooth morphologies having a few sparsely located crystallites (Figure 2.8G) that become more

populated in annealed films (Figure 2.8H). We suspect that these crystallites are those of PCBM molecules. In short summary, addition of PCBM seems to suppress crystallization of both **MO** and **SO**, while **SO** has a more pronounced effects on suppression of PCBM aggregation than **MO** does, owing to its tetrapodal structure that can potential interact with PCBM molecules more strongly. On the other hand, because of the break-water like structure of **SO**, the molecularly mixed state seems to result in thermally robust morphologies, which is preferred for OSC operations.

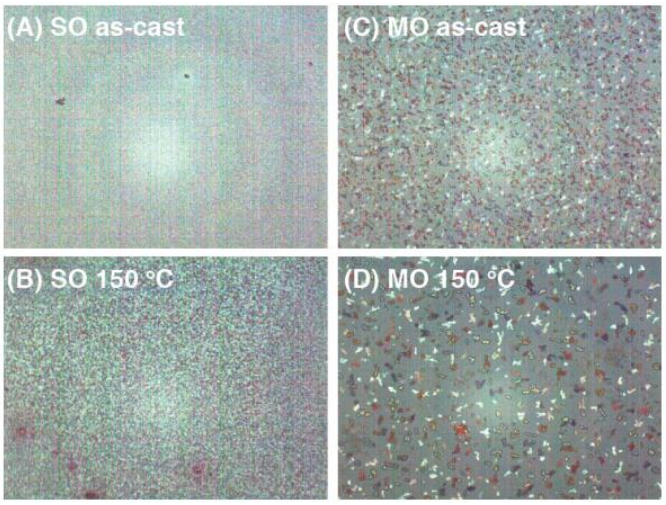

Figure 2.9 Cross-polarized light micrographs (400× magnification) of thin films of **SO** and **MO** under different annealing conditions.

2.3.3 Slow Cooling Experiment

Since DSC measurements showed slow crystallization behaviors for the **SO** compound, we attempted slow cooling experiments on the **SO**/PCBM (1/3) devices in hope to induce phase separation of these two components. The typical procedure is to anneal the devices on a hotplate with preset temperatures for 10 min and the hotplate is turned off without removing the device. The hotplate temperature then slowly drops to r.t. within 1.5 to 2 h and the devices are then tested. Four different preset hotplate

temperatures at 100 °C, 150 °C, 200 °C and 250 °C were selected. However, all devices under test displayed slightly reduced *PCE*s than those from the as-cast devices. Optical micrographs (Figure 2.10) of these slow-cooled devices showed identically smooth, aggregation free morphologies, indicating the ineffectiveness of this method for inducing appreciable phase separation between **SO** and PCBM.

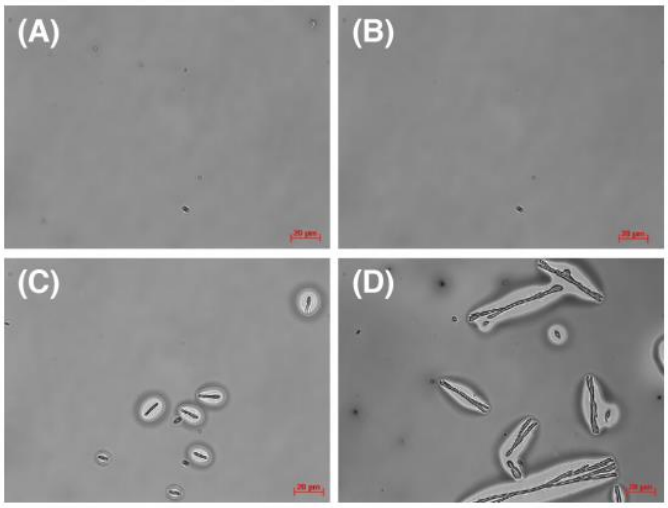

Figure 2.10 Optical micrographs (400 × magnification) of **SO**/PCBM (1/3) devices after slow cooling from (A) 100 °C, (B) 150 °C, (C) 200 °C and (D) 250 °C. Scale bars in all: 20 μm.

2.3.4 Solvent Annealing

Alternatively, solvent annealing has been shown as an effective method for inducing phase separation in blend films.[40-41] We thus tested the **SO**/PCBM (1/3) devices under solvent annealing conditions by placing the devices in a sealed container saturated with chlorobenzene vapor for up to 20 h. Devices were then tested after predetermined annealing times and subjected to optical microscopy measurements as summarized in Fig. 5. No performance differences were observed for devices annealed up to 1 h, although spherulite-like crystals started to appear and became denser and bigger with time (Figure

2.11 A–D). The devices annealed for 1.5 h, 3 h and 6 h all showed slightly improved *PCE* values to ca. 0.25–0.27%, which comes from an improvement in *FF* to ca. 44% accompanied by a decrease in J_{SC} to ca. 0.62 mA/cm^2. However, devices annealed for 20 h lost almost all of the photovoltaic effects and no diode behaviors could be observed. As seen in Figure 2.11E–G, at longer annealing times, the spherulite-like crystals seem to grow and merge into large platelets having straight boundaries. These platelets have lighter smoother central regions and darker needle-like peripherals, accompanied by randomly dispersed black spheres. These two regions eventually became clearly differentiated after annealing for 20 h (Figure 2.11H). We suspect that the darker crystals are those of PCBM and the lighter regions consist of **SO** or **SO**/PCBM complexes. Such solvent annealing induced crystallization, phase separation and eventual macro-phase separation likely explain the initial device improvement and final breakdown as observed. The exact identity of the needle-like crystals and mechanisms of such phase separation are currently under more detailed investigation.

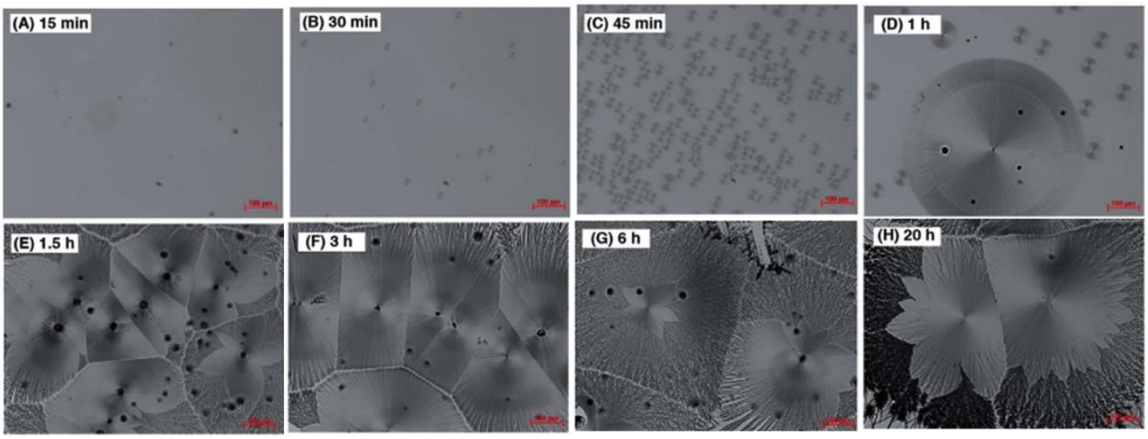

Figure 2.11 Optical micrographs (100 X magnificantion) of thin films of **SO** and PCBM (1/3, wt./wt.) blends after solvent annealing using chlorobenzene for various times. Scale bars in all: 100 μm.

2.4 Ternary Blend Devices

As discussed above, **SO** molecules tend to molecularly mix with PCBM molecules and thermal annealing is ineffective to drive appreciable phase separation. Solvent annealing does induce macroscopic phase separation but is not able to improve the device performances significantly. We suspect that addition of a third component, which has stronger interactions with either **SO** or PCBM, can potentially break up the **SO**/PCBM interactions and lead to one of the components to crystallize and phase separate into domains better for charge separation and extraction. To test this hypothesis, we chose poly (thienylene vinylene) (PTV) to be the third component. PTVs are a well-known class of conjugated polymers possessing narrow bandgaps and high crystallinity.[42-45] The π-π interactions among aromatic rings may lead to stronger **SO**/PTV interactions and the absorption windows of **SO** and PTV are complementary to each other, which can lead to improved photocurrents. Thus we have fabricated OSC devices using **SO**/PTV/PCBM ternary blends at different weight ratios. An in-house made poly (3-decylthienylene vinylene) (P3DTV, M_n = 21.3 kDa, *PDI* = 2.1)[46] was used in the studies, as shown in Scheme 2.2.

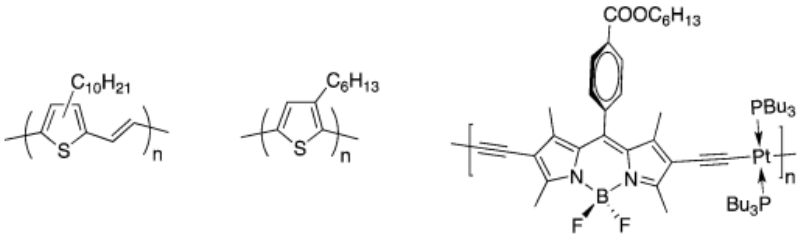

P3DTV **P3HT** **Pt-BODIPY**

Scheme 2.2 Structures of conjugated polymers applied in current studies.

The binary P3DTV/PCBM devices were first fabricated and optimized, from which a weight ratio of 1/1 and a thermal annealing temperature of 80 °C for 10 min were

found to be optimal, leading to a *PCE* of 0.49%. This relatively low efficiency is comparable to previously reported examples and is possibly caused by the short lifetimes of excitons in PTVs.[47-48] Thus, in the ternary blends, we kept the weight ratios of **SO**/PCBM and P3DTV/PCBM to be consistent at 1/3 and 1/1, respectively. Thermal annealing was found to slightly enhance ternary device performance and the optimal temperature was found to be 80 °C, beyond which device deterioration occurred. Table 2.1 summarizes detailed device parameters involving binary and ternary blends at different weight ratios and the corresponding I-V curves are included in Figure 2.12.

Table 2.1 Binary and Ternary Device Performances.[a]

SO/P3DTV/PCBM[b]	V_{OC} (V)	J_{SC} (mA/cm^2)	*FF* (%)	*PCE* (%)
(A) 2.5 / 0.0 / 7.5[c]	0.84	1.01	26	0.22
(B) 2.5 / 0.5 / 8.0	0.55	2.17	37	0.44
(C) 2.5 / 1.5 / 9.0	0.52	3.67	52	1.00
(D) 2.5 / 2.5 /10.0	0.52	4.34	54	1.22
(E) 2.0 / 2.5 / 8.5	0.52	5.18	54	1.45
(F) 1.5 / 2.5 / 7.0	0.52	5.52	54	1.54
(G) 1.0 / 2.5 / 5.5	0.51	4.27	55	1.19
(H) 0.5 / 2.5 / 4.0	0.48	3.48	52	0.87
(I) 0.0 / 2.5 / 2.5	0.45	2.22	49	0.49

[a] All devices are thermally annealed at 80 °C for 10 min; results are reported as averages of five individual cells. [b] All ratios by weight. [c] As-cast device.

Several trends are clearly observed going from binary blends to ternary blends. The V_{OC} values of ternary devices are all between those of the binary devices employing P3DTV and **SO**. These values decrease with increasing P3DTV contents and are all much closer to the side of P3DTV. For instance, in devices B (Table 2.1), addition of only 20 wt.% P3DTV (relative to **SO**) reduces the V_{OC} from 0.84 V in device A to 0.55 V. It is known that the V_{OC} of a BHJ solar cell is closely related to the energy difference between

the HOMO level of electron donor and the LUMO level of the electron acceptor.[49] Owing to the high lying HOMO level of P3DTV at ca. −4.9 eV (from CV measurements), devices containing P3DTV are expected to have reduced V_{OC} values. Interestingly, previous examples showed close to linear relationships between V_{OC} and composition changes.[50-51] In our case, we plot the V_{OC} values against P3DTV contents in the donor blends (Figure 2.13) and find that the relationship is far from linearity. All devices containing P3DTV display comparable V_{OC} values that are significantly smaller than that of the **SO** only device. This implies that in our ternary devices, P3DTV is the major hole conducting material despite of its contents, which is likely caused by high crystallinity and long-chain structures of the polymer.

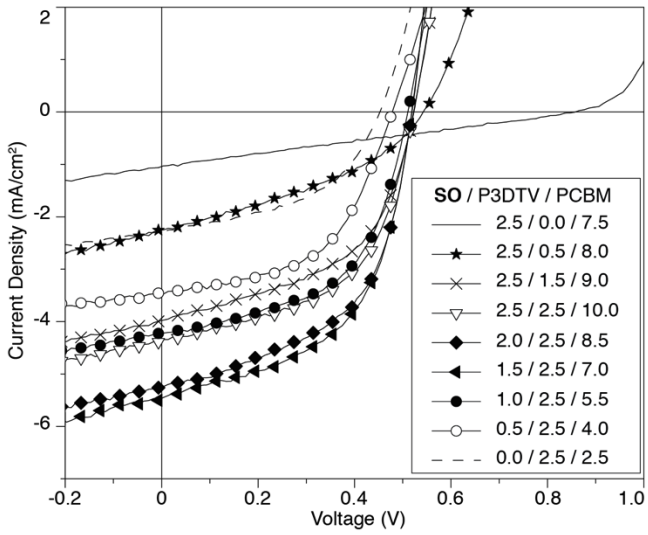

Figure 2.12 Current density-voltage (I-V) curves of devices employing **SO**, P3DTV and PCBM at various weight ratios under simulated white light (100 mW/cm^2).

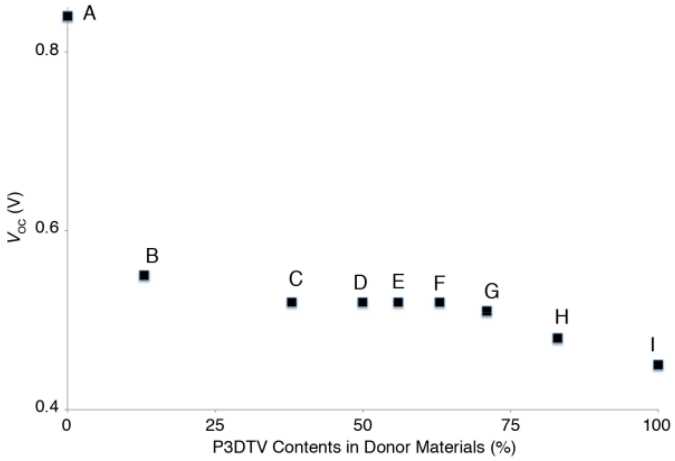

Figure 2.13 Open circuit voltage (V_{OC}) versus P3DTV contents in donor materials of various solar cell devices. See Table 1 for labeling details.

Another obvious trend is the enhancement of J_{SC} in the ternary blend devices that all, except B, show higher J_{SC} values than the binary devices. Device D can be considered a linear combination of the contents of binary devices A and I, but gives a higher J_{SC} of 4.34 mA/cm^2 than the sum of J_{SC} values of devices A and I (3.23 mA/cm^2). This indicates that there are cooperative effects on photocurrent generation by mixing **SO** and P3DTV, which enhance charge extraction from both of these materials. The best device tested is F that displays the highest J_{SC} of 5.52 mA/cm^2 and a *PCE* of 1.54%, which is ca. 3 and 7 times higher than those of binary devices employing P3DTV and **SO** alone, respectively.

Noticeably, all ternary devices show significantly higher *FF*s than the **SO** binary device, which can be related to improved morphologies by adding P3DTV. Thus, we have studied the best ternary device F by optical microscopy (Figure 2.14) and atomic force microscopy (AFM). The binary devices are also studied by AFM for comparison and all AFM images are included in Figure 2.15. As shown in Figure 2.14, the ternary film under both as-cast and annealing at 80 °C conditions do not display any appreciable

aggregation or crystallization. However, when annealed at 150 °C for 10 min, large needle like PCBM crystallites are observed. This macro-phase separation indicates the effectiveness of adding P3DTV on reducing the strong **SO**/PCBM interactions. The AFM measurements probe the thin film morphologies on the nanometer scale. As displayed in Figure 2.15A and 2.15B, the **SO**/PCBM binary blends show very smooth morphologies that lack appreciable phase separation, confirming the intermixed nature of the blend. On the other hand, much rougher topography is observed in the P3DTV/PCBM binary blends and larger aggregates are clearly present (Figure 2.15C and 2.15D). As a result, the **SO**/P3DTV/PCBM ternary blends display morphologies somewhat in between those of the binary blends (Figure 2.15E and 2.15F). This more pronounced phase separation thus creates more pure donor and acceptor domains that lead to better charge separation and collection, and enhanced performance of the ternary devices over that of the binary devices.

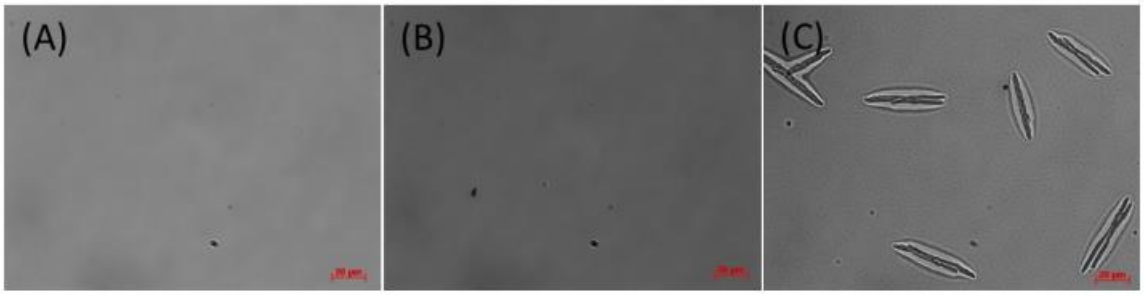

Figure 2.14 Optical micrographs (400 X magnifications) of device F containing **SO**/P3DTV/PCBM (1.5/2.5/7.0) blend films: (A) as cast; (B) annealed at 80 °C for 10 min; (C) annealed at 150 °C for 10 min. Scale bars in all: 20 μm.

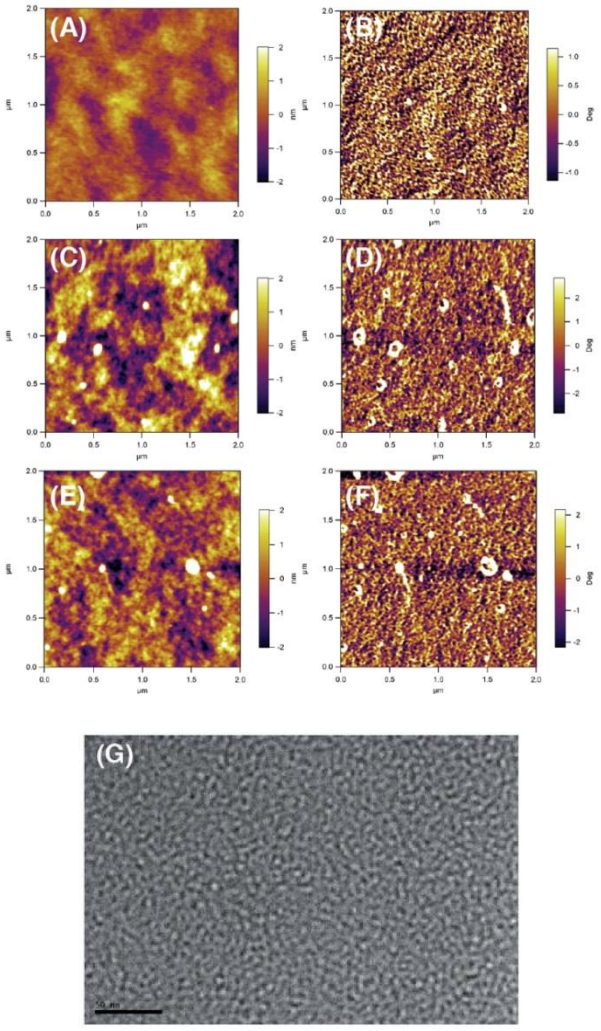

Figure 2.15 Tapping-mode atomic force microscopy (AFM) height images (left column) and phase images (right column) of binary device A (**SO**/PCBM 1/3; A and B), binary device I (P3DTV/PCBM 1/1; C and D) and ternary device F (**SO**/P3DTV/PCBM 1.5/2.5/7.0; E and F). All images are 2×2 μm in size. (G) Transmission electron microscopy (TEM) image of device F; scale bar: 50 nm.

In addition to P3DTV, which is a low bandgap, crystalline and less efficient polymer, we have started investigating ternary solar cells containing **SO**/PCBM and other types of conjugated polymers including regio-regular poly(3-hexylthiophene) (P3HT) and a platinum containing polymer (Pt–BODIPY) made in-house,[48] as shown in Scheme 2.

Compared with P3DTV, P3HT possesses similarly high crystallinity and comparable HOMO energy level, but a slightly larger bandgap at ca. 1.9 eV, and is one of the most studied high performing conjugated polymers in OSC research. On the other hand, the Pt–BODIPY polymer has a small bandgap at ca. 1.7 eV, a deep lying HOMO level at ca. 5.3 eV and is an amorphous material. Table 2.2 summarizes performance parameters of ternary devices employing these materials at various weight ratios.

Consistently, cooperative effects are observed in both types of ternary devices, as both devices K and O outperform the corresponding optimized binary devices. In device K, addition of 20 wt% **SO** increases the optimized P3HT/PCBM binary device efficiency from 3.63% to 4.22%, which mainly comes from the enhancement in *FF* up to 69%. This indicates improved morphologies in this ternary blend over the well-studied P3HT/PCBM binary blends, which implies an effective way to optimize conjugated polymer/fullerene blend morphologies and is currently under more detailed studies. Not surprisingly, the highly crystalline P3HT acts as the major hole conductor in the ternary blends similar to the case for P3DTV, since the addition of a minority amount of P3HT drastically decreases the V_{OC} values. On the other hand in device O, addition of 20 wt% **SO** into the Pt–BODIPY/PCBM binary device also improves the performance, which is however resulted from an increase in J_{SC}. Since Pt–BODIPY has a lower bandgap than **SO**, such increase in J_{SC} is likely a result of complementary absorption. The relatively small *FF*s in all ternary devices are supposedly explained by the amorphous nature of both **SO** and Pt–BODIPY, mixtures of which are thus expected to result in hardly improved morphologies. Both compounds have similar deep lying HOMO levels, leading to high V_{OC} values in all ternary devices. Interestingly, devices O and P have V_{OC} values

slightly higher than those of corresponding binary devices, the reasons for which are currently under investigation.

Table 2.2 Ternary devices involving P3HT and Pt–BODIPY.[a]

SO/P3HT/PCBM[b]	V_{OC} (V)	J_{SC} (mA/cm^2)	*FF* (%)	*PCE* (%)
(J) 0.0 / 5.0 / 5.0	0.57	10.70	59	3.63
(K) 1.0 / 5.0 / 5.0	0.59	10.31	69	4.22
(L) 2.5 / 2.5 / 7.5	0.62	4.23	62	1.63
(M) 4.0 / 1.0 /12.0	0.71	2.46	48	0.83
SO/Pt-BODIPY/PCBM[c]				
(N)0.0 / 2.5 / 7.5	0.86	2.23	48	0.91
(O) 0.5 / 2.5 / 7.5	0.91	3.39	45	1.39
(P) 2.5 / 2.5 / 7.5	0.93	2.49	33	0.77
(Q) 2.5 / 0.5 / 7.5	0.86	2.05	38	0.68

[a] Results are reported as averages of five individual cells; all ratios by weight. [b] All devices are thermally annealed at 150 °C for 10 min. [c] As cast devices.

2.5 Conclusions

We have successfully prepared a molecular tetrapod possessing a tetraphenylsilance core. The molecule has a relatively small bandgap and a deep lying HOMO energy level. The tetrapod was also found to be very hard to crystallize, which led to molecularly mixed blends with PCBM and poor solar cell device performances. This inferior morphology could be improved by adding a low bandgap PTV derivative that can induce appreciable phase separation in the ternary blends and result in much enhanced device efficiencies. Our findings can give useful insights on the structure-property relationships of such 3-D small molecules and their applications in multi-component OSCs. We are currently investigating the possibilities of increasing the

crystallization kinetics of the tetrapods and of inducing phase separations in multi-component blend films by variations of molecular structures and processing conditions.

2.6 Experimental Section

2.6.1 Materials and General Methods

All reagents and solvents were used as received from Sigma-Aldrich or Alfa Aesar unless otherwise noted. THF was distilled from Na/benzophenone prior to use. 2-Tributylstannylthiophene (**3**),[53] 2,2'-bithiophene-5-carbaldehyde (**4**),[54] 5'-bromo-(2,2'-bithiophene)-5-carbaldehyde (**5**),[54] 2-bromo-3-hexylthiophene (**6**),[55] 3-hexyl-2-trimethylstannylthiophene (**7**)[56] were prepared according to literature procedures. 300.13 MHz ^{1}H and 75.48 MHz ^{13}C NMR spectra were recorded on a Bruker Avance III Solution 300 spectrometer. All solution ^{1}H and ^{13}C NMR spectra were referenced internally to solvent signals. Ultraviolet−visible (UV−vis) absorption spectra were recorded on a Shimadzu UV-2401 PC spectrometer over a wavelength range of 240−900 nm. Fluorescence emission spectra were obtained using a Varian Cary Eclipse fluorimeter. Time-of-flight mass spectrometry (TOF MS) was performed on a Waters/Micromass LCT Premier system operating under atmospheric pressure photoionization (APPI+) mode. Cyclic voltammetry was performed at 25 °C on a CH Instrument CHI604xD electrochemical analyzer using a glassy carbon working electrode, a platinum wire counter electrode, and a Ag/AgCl reference electrode calibrated using ferrocene redox couple (4.8 eV below vacuum). Optical Micrographs were taken on a Carl Zesis Axio Imager 2 microscope at a 400X magnification. Atomic force microscopy (AFM) measurements were performed on an Asylum MFP3D AFM instrument operated under tapping mode. Powder X-ray diffraction measurements were performed on a

Rigaku SmartLab instrument. Differential scanning calorimetry (DSC) measurements were performed on a Mettler Toledo DSC STAR^e system with ca. 10 mg sample and at scan rates of 10 °C / min and 1 °C / min. Thin film thickness was measured using a KLA-Tencor AlphaStep D-100 profiler.

2.6.2 Solar Cell Fabrication and Testing

A conventional structure of ITO/MoO_3 (10 nm)/active layer (100 nm)/Al (100 nm) was adopted for the solar cells studied. Devices were fabricated according to the following procedures. **SO** and PCBM (American Dye Source, Inc.) at predetermined weight ratios were dissolved in chlorobenzene (CB) and stirred at 80 °C for 10 h in a nitrogen glovebox (Innovative Technology, model PL-He-2GB, O_2 < 0.1 ppm, H_2O < 0.1 ppm). ITO-coated glass substrates (China Shenzhen Southern Glass Display. Ltd, 8 Ω/□) were cleaned by ultrasonication sequentially in detergent, DI water, acetone and isopropyl alcohol, each for 15 min. These ITO-coated glass substrates were further treated by UV-ozone (PSD Series, Novascan) for 45 min before transferred into a nitrogen glovebox (Innovative Technology, model PL-He-4GB-1800, O_2 < 0.1 ppm, H_2O < 0.1 ppm) for MoO_3 deposition. MoO_3 (10 nm) was deposited using an Angstrom Engineering Åmod deposition system at a base vacuum level < 7×10^{-8} Torr. The blend solution was first filtered through a 0.45 μm PTFE filter and spin-coated on top of the MoO_3 layer at preset speeds for 30s. Typical thickness of organic layers was ca. 100 nm. Al (100 nm) was finally thermally evaporated through patterned shadow masks as anodes. Current−voltage (I−V) characteristics were measured by a Keithley 2400 source-measuring unit under simulated AM1.5G irradiation (100 mW/cm^2) generated by a Xe arc-lamp based Newport 67005 150-W solar simulator equipped with an AM1.5G filter.

The light intensity was calibrated by using a Newport thermopile detector (model 818P-010-12) equipped with a Newport 1916-C Optical Power Meter.

2.6.3 Synthetic Details

1. 1, 4-Dibromobenzene (5.00 g, 21.2 mmol) was weighed into a dry 100 mL Schlenk flask and 50 mL anhydrous THF was added through cannular. The flask was cooled to −78 °C and 8.1 mL ^{n}BuLi (2.5 M in THF, 20.2 mmol) solution was added dropwise. The reaction mixture was stirred at −78 °C for 2 hours and a 5 mL THF solution of $SiCl_4$ (0.742 g, 4.36 mmol) was added dropwise through syringe. The reaction mixture was first kept stirring at −78 °C for 1 hour and then warmed up to room temperature and stirred overnight. The reaction mixture was extracted by ethyl ether, followed by washing with DI H_2O and saturated brine solution. After the organic layer was dried with anhydrous Na_2SO_4, the solvent was removed under reduced pressure. The crude product was purified by silica gel chromatography using hexanes to yield compound **1** as a white powder (2.24 g, 78.9%). ^{1}H NMR (300.13 MHz, $CDCl_3$): δ (ppm) = 7.33 (*Ph-H*, d, 8H, J^{3}_{HH} = 8.4 Hz), 7.53 (*Ph-H*, d, 8H, J^{3}_{HH} = 8.1 Hz). ^{13}C NMR (75.48 MHz, $CDCl_3$): δ (ppm) = 125.4, 131.4, 131.5, 137.6.

2. 2-Bromothiophene (21.6 mL, 0.223 mol) was injected via syringe into a 1 L 3-neck round bottom flask equipped with an addition funnel and a stir bar under positive N_2 pressure. Anhydrous THF (ca. 400 mL) was transferred into the flask through cannular. Lithium diisopropylamide solution (2M in THF/heptane/ethylbenzene, 123.0 mL, 0.246 mol) was transferred into the addition funnel and added dropwise at −78 °C. The reaction mixture was kept stirring at −78 °C for 30 min and then warmed up to room temperature. Anhydrous N,N-dimethylformamide (25.8 mL, 0.335 mol) was added slowly through a

degassed syringe. The reaction mixture was further stirred at room temperature overnight. After standard aqueous workup, compound **2** was obtained as a colorless liquid by vacuum distillation. (37.0 g, 86.8%). ^{1}H NMR (300.13 MHz, $CDCl_3$): δ (ppm) = 7.19 (*Th-H*, d, 1H, J^3_{HH} = 3.9 Hz), 7.52 (*Th-H*, d, 1H, J^3_{HH} = 4.2 Hz), 9.78 (-*CHO*, s, 1H).

8. Compound **7** (1.09 g, 4.00 mmol) and compound **5** (1.59 g, 4.80 mmol) were dissolved in 30 mL anhydrous DMF in a pressure vessel containing a magnetic stir bar inside an argon filled glovebox. $Pd(PPh_3)_4$ (69.3 mg, 1.5 mol%) was then added to the reaction mixture. The pressure vessel was sealed and taken out of the glovebox. The reaction was carried out at 80 °C for 24 hours and then cooled to room temperature. After standard aqueous workup, compound **8** was further purified by silica gel chromatography with hexane/ethyl acetate (1.28 g, 88.9%). ^{1}H NMR (300.13 MHz, $CDCl_3$): δ (ppm) = 0.89 (-*CH*$_3$, t, 3H, J^3_{HH} = 6.9 Hz), 1.28-1.41 (-*CH*$_2$-, m, 6H), 1.65 (-*CH*$_2$-, m, 2H), 2.78 (-*CH*$_2$-, t, 2H, J^3_{HH} = 7.8 Hz), 6.96 (*Th-H*, d, 1H, J^3_{HH} = 6.6 Hz), 7.07 (*Th-H*, d, 1H, J^3_{HH} = 3.6 Hz), 7.22 (*Th-H*, d, 1H, J^3_{HH} = 4.8 Hz), 7.25 (*Th-H*, d, 1H, J^3_{HH} = 4.2 Hz), 7.32 (*Th-H*, d, 1H, J^3_{HH} = 3.6 Hz), 7.68 (*Th-H*, d, 1H, J^3_{HH} = 3.9 Hz), 9.87 (-*CHO*, s, 1H). ^{13}C NMR (75.48 MHz, $CDCl_3$): δ (ppm) = 13.9, 22.4, 29.0, 29.1, 30.2, 31.4, 123.6, 124.2, 126.2, 126.3, 129.5, 130.0, 134.9, 137.1, 138.0, 140.1, 141.2, 146.5, 182.0.

9. Compound **8** (1.28 g, 3.55 mmol), ethylene glycol (2.0 mL, 35.8 mmol) and a catalytic amount of *p*-toluenesulfonic acid were dissolved in 50 mL benzene in a 100 mL round bottom flask equipped with a Dean-Stark apparatus. The reaction mixture was refluxed at 150 °C for 24 hours. The resulted reaction mixture was extracted by ethyl ether and followed by washing with saturated $NaHCO_3$, DI H_2O and saturated brine solution. After the organic layer was dried with anhydrous Na_2SO_4, the solvent was removed under

reduced pressure. The crude compound was further dried under vacuum and used for next step without further purification (1.24 g, 86.4%). ^{1}H NMR (300.13 MHz, $CDCl_3$): δ (ppm) = 0.88 (-*CH*$_3$, t, 3H, J^3_{HH} = 6.6 Hz), 1.26-1.39 (-*CH*$_2$-, m, 6H), 1.64 (-*CH*$_2$-, m, 2H), 2.76 (-*CH*$_2$-, t, 2H, J^3_{HH} = 7.8 Hz), 4.04 (-*OCH*$_2$-, m, 2H), 4.14 (-*OCH*$_2$-, m, 2H), 6.09 (-*OCHO*-, s, 1H), 6.93 (*Th-H*, d, 1H, J^3_{HH} = 5.1 Hz), 7.01 (*Th-H*, d, 1H, J^3_{HH} = 3.6 Hz), 7.05 (*Th-H*, d, 1H, J^3_{HH} = 3.6 Hz), 7.07 (*Th-H*, d, 1H, J^3_{HH} = 3.6 Hz), 7.11 (*Th-H*, d, 1H, J^3_{HH} = 3.6 Hz), 7.17 (*Th-H*, d, 1H, J^3_{HH} = 5.1 Hz). ^{13}C NMR (75.48 MHz, $CDCl_3$): δ (ppm) = 14.1, 22.6, 29.2, 29.3, 30.6, 31.6, 65.2, 100.2, 123.0, 123.9, 124.2, 126.4, 127.0, 130.1, 130.2, 135.6, 136.8, 138.2, 139.9, 140.6.

10. Compound **9** (0.505 g, 1.25 mmol) was weighed into a dry 100 mL Schlenk flask under nitrogen, and 50 mL anhydrous THF was transferred through a cannular. The flask was cooled to −78 °C and 0.55 mL ^{n}BuLi (2.5 M in THF, 1.37 mmol) solution was added dropwise through a degassed syringe. The reaction mixture was stirred at −78 °C for 30 min and warmed up to room temperature. A Me_3SnCl solution (1 M in THF, 1.5 mL, 1.5 mmol) was then added dropwise. The reaction mixture was kept stirring at room temperature overnight. The resulting reaction mixture was extracted by ethyl ether, followed by washing with DI H_2O and saturated brine solution. After the organic layer was dried with anhydrous Na_2SO_4, the solvent was removed under reduced pressure. The crude compound was further dried under high vacuum and used for next step without further purification (0.709 g, 100%). ^{1}H NMR (300.13 MHz, $CDCl_3$): δ (ppm) = 0.38 (-*CH*$_3$, s, 9H), 0.87 (-*CH*$_3$, t, 3H, J^3_{HH} = 6.9 Hz), 1.26-1.39 (-*CH*$_2$-, m, 6H), 1.64 (-*CH*$_2$-, m, 2H), 2.78 (-*CH*$_2$-, t, 2H, J^3_{HH} = 7.8 Hz), 4.02 (-*OCH*$_2$-, m, 2H), 4.15 (-*OCH*$_2$-, m, 2H), 6.08 (-*OCHO*-, s, 1H), 6.99 (*Th-H*, d, 1H, J^3_{HH} = 3.9 Hz), 7.00 (*Th-H*, s, 1H), 7.04 (*Th-H*,

d, 1H, J^3_{HH} = 3.6 Hz), 7.06 (*Th-H*, d, 1H, J^3_{HH} = 3.9 Hz), 7.10 (*Th-H*, d, 1H, J^3_{HH} = 3.6 Hz). ^{13}C NMR (75.48 MHz, $CDCl_3$): δ (ppm) = −8.2, 14.1, 22.6, 29.2, 29.3, 30.7, 31.6, 65.2, 100.2, 122.9, 124.2, 126.0, 127.0, 135.9, 136.0, 136.5, 136.8, 138.3, 138.4, 140.4, 141.0.

11. Compound **1** (0.170 g, 0.26 mmol), compound **10** (0.709 g, 1.25 mmol) and $Pd(PPh_3)_4$ (9 mg, 3 mol%) were dissolved in 20 mL anhydrous DMF in a pressure vessel containing a magnetic stir bar under argon. The pressure vessel was sealed and stirred at 90 °C for 24 hours. After cooling to room temperature, the reaction mixture was extracted with $CHCl_3$, followed by washing with 1 M HCl, saturated $NaHCO_3$, DI H_2O and brine. After the organic layer was dried with anhydrous Na_2SO_4, the solvent was removed under reduced pressure. The crude product was further purified by silica gel chromatography with dichloromethane/ethyl acetate to yield **11** as a brown solid (200 mg, 43.3%). ^{1}H NMR (300.13 MHz, $CDCl_3$): δ (ppm) = 0.90 (-*CH*$_3$, t, 12H, J^3_{HH} = 6.9 Hz), 1.32-1.43 (-*CH*$_2$-, m, 24H), 1.71 (-*CH*$_2$-, m, 8H), 2.81 (-*CH*$_2$-, t, 8H, J^3_{HH} = 4.8 Hz), 7.13 (*Th-H*, d, 4H, J^3_{HH} = 3.6 Hz), 7.24 (*Th-H*, s, 4H), 7.27(*Th-H*, d, 4H, J^3_{HH} = 3.6 Hz), 7.33 (*Th-H*, d, 4H, J^3_{HH} = 3.9 Hz), 7.64(*Ph-H*, m, 16H), 7.68 (*Th-H*, d, 4H, J^3_{HH} = 3.9 Hz), 9.87 (-*CHO*, s, 4H). ^{13}C NMR (75.48 MHz, $CDCl_3$): δ (ppm) = 14.1, 22.6, 29.2, 29.7, 30.4, 31.6, 124.0, 125.0, 126.5, 126.6, 126.8, 129.9, 133.1, 135.1, 135.3, 136.9, 137.4, 138.1, 141.5, 141.6, 142.2, 146.8, 182.4. TOF MS (APPI$^+$): Calcd. for $SiC_{100}H_{92}O_4S_{12}$: 1768.3414 [M^+], 1791.3312 [$M+Na^+$]; found: 1768.3419 [M^+], 1791.3317 [$M+Na^+$].

12. Cyanoacetic acid (5.00 g, 58.8 mmol), octanol (9.8 mL, 61.8 mmol) and a catalytic amount of *p*-toluenesulfonic acid were dissolved in 30 mL benzene into a 100 mL round bottom flask equipped with a Dean-Stark apparatus. The reaction mixture was refluxed at

120 °C for 24 hours. After solvent removal under vacuum, **12** was purified by vacuum distillation as a colorless liquid (9.40 g, 81.1%). ^{1}H NMR (300.13 MHz, $CDCl_3$): δ (ppm) = 0.89 (-*CH*$_3$, t, 3H, J^3_{HH} = 6.9 Hz), 1.28-1.38 (-*CH*$_2$-, m, 10H), 1.68 (-*CH*$_2$-, m, 2H), 3.45 (-*CH*$_2$-, s, 1H), 4.20 (-*OCH*$_2$-, t, 2H, J^3_{HH} = 6.9 Hz). ^{13}C NMR (75.48 MHz, $CDCl_3$): δ (ppm) = 14.0, 22.6, 24.7, 25.7, 28.3, 29.1, 31.7, 67.1, 113.0, 162.9.

13. Compound **8** (0.600 g, 1.66 mmol) was dissolved in 25 mL DMF in a 50 mL round bottom flask and immersed in an ice bath. N-bromosuccinimide (NBS, 0.356 g, 2.00 mmol) powder was added with vigorous stirring. The reaction was warmed up to room temperature and stirred for overnight. The resulting reaction mixture was first extracted with $CHCl_3$, followed by washing with saturated Na_2SO_3, 1 M HCl solution, DI H_2O and brine solution. Solvents were removed under reduced pressure and the resulted crude product was further purified by column chromatography to get **13** as a yellow solid (0.655 g, 89.5%). ^{1}H NMR (300.13 MHz, $CDCl_3$): δ (ppm) = 0.89 (-*CH*$_3$, t, 3H, J^3_{HH} = 6.9 Hz), 1.28-1.41 (-*CH*$_2$-, m, 6H), 1.62 (-*CH*$_2$-, m, 2H), 2.71 (-*CH*$_2$-, t, 2H, J^3_{HH} = 7.8 Hz), 6.92 (*Th-H*, s, 1H), 7.01 (*Th-H*, d, 1H, J^3_{HH} = 3.9 Hz), 7.25 (*Th-H*, d, 1H, J^3_{HH} = 4.8 Hz), 7.30 (*Th-H*, d, 1H, J^3_{HH} = 3.6 Hz), 7.68 (*Th-H*, d, 1H, J^3_{HH} = 4.2 Hz), 9.87 (-*CHO*, s, 1H). ^{13}C NMR (75.48 MHz, $CDCl_3$): δ (ppm) = 13.9, 22.4, 28.9, 29.1, 30.1, 31.4, 111.1, 123.9, 126.2, 126.7, 131.0, 132.7, 135.5, 136.5, 137.1, 140.7, 141.5, 146.2, 182.1.

14. Compound **13** (0.655 g, 1.50 mmol) and trimethylstannylbenzene (0.542 g, 2.25 mmol) were dissolved in 30 mL anhydrous DMF in a pressure vessel containing a magnetic stir bar under argon. $Pd(PPh_3)_4$ (43.4 mg, 2.5 mol%), CuI (28.5 mg, 10.0 mol%) and CsF (0.342 g, 2.25 mmol) were added to the pressure vessel in an argon filled glovebox. The pressure vessel was sealed and taken out of the glovebox. The reaction

was stirred at 80 °C for 24 hours. After cooling to room temperature, the reaction mixture was first extracted with $CHCl_3$ and followed by washing with 1 M HCl solution, saturated $NaHCO_3$, DI H_2O and brine solution. Solvents were removed under reduced pressure and the crude product was further purified by silica gel column chromatography with hexane/ethyl acetate (0.46 g, 70.7%) ^{1}H NMR (300.13 MHz, $CDCl_3$): δ (ppm) = 0.90 (-*CH*$_3$, t, 3H, J^3_{HH} = 6.9 Hz), 1.30-1.42 (-*CH*$_2$-, m, 6H), 1.62 (-*CH*$_2$-, m, 2H), 2.79 (-*CH*$_2$-, t, 2H, J^3_{HH} = 7.8 Hz), 7.11 (*Th-H*, d, 1H, J^3_{HH} = 3.9 Hz), 7.17 (*Th-H*, s, 1H), 7.25 (*Th-H*, d, 1H, J^3_{HH} = 3.6 Hz), 7.30 (*Ph-H*, d, 1H, J^3_{HH} = 6.6 Hz), 7.32 (*Th-H*, d, 1H, J^3_{HH} = 3.6 Hz), 7.39 (*Ph-H*-, m, 2H), 7.60 (*Ph-H*-, d, 2H, J^3_{HH} = 8.4 Hz), 7.67 (*Th-H*, d, 1H, J^3_{HH} = 3.9 Hz), 9.87 (-*CHO*, s, 1H). ^{13}C NMR (75.48 MHz, $CDCl_3$): δ (ppm) = 14.1, 22.6, 29.2, 29.7, 30.4, 31.6, 123.9, 125.6, 126.2, 126.4, 126.5, 127.8, 128.9, 129.2, 133.8, 135.1, 137.3, 138.3, 141.4, 141.5, 142.8, 146.9, 182.3.

MO. Compounds **14** (0.131 g, 0.300 mmol) and **12** (0.118 g, 0.60 mmol) were dissolved 15 mL $CHCl_3$ containing 0.5 mL triethylamine. The reaction mixture was first bubbled with N_2 for 30 min and stirred at room temperature for 2 days. Solvents were removed under reduced pressure and **MO** was purified by silica gel column chromatography with hexane/dichloromethane and by precipitation into methanol as a dark red solid (160 mg, 86.7%) ^{1}H NMR (300.13 MHz, $CDCl_3$): δ (ppm) = 0.90 (-*CH*$_3$, t, 3H, J^3_{HH} = 6.9 Hz), 1.33-1.42 (-*CH*$_2$-, m, 16H), 1.74 (-*CH*$_2$-, m, 4H), 2.81 (-*CH*$_2$-, t, 2H, J^3_{HH} = 7.8 Hz), 4.30 (-*CH*$_2$-, t, 2H, J^3_{HH} = 6.9 Hz) 7.13 (*Th-H*, d, 1H, J^3_{HH} = 4.2 Hz), 7.18 (*Th-H*, s, 1H), 7.26 (*Th-H*, d, 1H, J^3_{HH} = 3.6 Hz), 7.31 (*Ph-H*-, d, 1H, J^3_{HH} = 7.2 Hz), 7.37 (*Th-H*, d, 1H, J^3_{HH} = 3.9 Hz), 7.39 (*Ph-H*-, m, 2H), 7.61 (*Ph-H*-, d, 2H, J^3_{HH} = 7.8 Hz), 7.68 (*Th-H*, d, 1H, J^3_{HH} = 4.2 Hz), 8.26 (-*CH*=*C*-, s, 1H). ^{13}C NMR (75.48 MHz, $CDCl_3$): δ (ppm) = 14.1,

22.6, 25.6, 28.5, 29.1, 29.7, 30.4, 31.7, 31.8, 66.6, 97.6, 116.0, 124.1, 125.6, 126.3, 126.6, 126.9, 127.8, 128.9, 129.3, 133.7, 134.2, 134.8, 138.7, 139.1, 141.6, 142.9, 146.0, 147.2, 163.0.

SO. Compound **11** (88 mg, 0.05 mmol), compound **12** (98.5 mg, 0.50 mmol) and 1 mL triethylamine were dissolved in 30 mL $CHCl_3$. The reaction mixture was purged with N_2 for 30 min and then stirred at room temperature for 48 h. After solvent removal under vacuum, **SO** was purified by silica gel chromatography with hexane/dichloromethane and then precipitation into methanol as a dark red solid (105 mg, 84.5%). ^{1}H NMR (300.13 MHz, $CDCl_3$): δ (ppm) = 0.89-0.90 (-*CH*$_3$, t, 24H), 1.31-1.34 (-*CH*$_2$-, m, 64H), 1.69-1.77 (-*CH*$_2$-, m, 16H), 2.82 (-*CH*$_2$-, t, 8H, J^3_{HH} = 7.8 Hz), 4.29 (-*OCH*$_2$-, t, 8H, J^3_{HH} = 6.9 Hz), 7.14 (*Th-H*, d, 4H, J^3_{HH} = 3.9 Hz), 7.25 (*Th-H*, d, 4H, J^3_{HH} = 3.9 Hz), 7.27 (*Th-H*, s, 4H), 7.37 (*Th-H*, d, 4H, J^3_{HH} = 3.9 Hz), 7.64 (*Ph-H*, m, 16H), 7.67 (*Th-H*, d, 4H, J^3_{HH} = 4.2 Hz), 8.26 (-CH=C, s, 4H). ^{13}C NMR (75.48 MHz, $CDCl_3$): δ (ppm) = 14.1, 22.6, 25.8, 28.6, 29.2, 29.7, 30.4, 31.7, 31.8, 66.6, 97.7, 116.0, 124.2, 125.0, 126.7, 126.8, 126.9, 129.9, 133.2, 134.3, 135.0, 135.1, 136.9, 138.6, 139.1, 141.7, 142.4, 146.1, 147.1, 163.0.

2.7 References

(1) Hoppe, H.; Sariciftci, N. S. *J. Mater. Res.* **2004**, 19, 1924.

(2) Spanggaard, H.; Krebs, F. C. *Sol. Energy Mater. Sol. Cells* **2004**, 83, 125.

(3) Thompson, B. C.; Fréchet, J. M. J. *Angew. Chem. Int. Ed.* **2008**, 47, 58.

(4) Dennler, G.; Scharber, M. C.; Brabec, C. J. *Adv. Mater.* **2009**, 21, 1323.

(5) Cheng, Y.-J.; Yang, S.-H.; Hsu, C.-S. *Chem. Rev.* **2009**, 109, 5868.

(6) Chen, H.-Y.; Hou, J.; Zhang, S.; Liang, Y.; Yang, G.; Yang, Y.; Yu, L.; Wu, Y.; Li, G. *Nat. Photon.* **2009**, 3, 649.

(7) Liang, Y.; Xu, Z.; Xia, J.; Tsai, S.-T.; Wu, Y.; Li, G.; Ray, C.; Yu, L. *Adv. Energy Mater.* **2010**, 22, E135.

(8) Chu, T.-Y.; Lu, J.; Beaupré, S.; Zhang, Y.; Pouliot, J.-R.; Wakim, S.; Zhou, J.; Leclerc, M.; Li, Z.; Ding, J.; Tao, Y. *J. Am. Chem. Soc.* **2011**, 133, 4250.

(9) Zhou, H.; Yang, L.; Stuart, A. C.; Price, S. C.; Liu, S.; You, W. *Angew. Chem. Int. Ed.* **2011**, 50, 2995.

(10) He, Z.; Zhong, C.; Su, S.; Xu, M.; Wu, H.; Cao, Y. *Nat. Photon.* **2012**, 6, 591.

(11) Yang, T.; Wang, M.; Duan, C.; Hu, X.; Huang, L.; Peng, J.; Huang, F.; Gong, X. *Energy Environ. Sci.* **2012**, 5, 8208.

(12) You, J.; Dou, L.; Yoshimura, K.; Kato, T.; Ohya, K.; Moriarty, T.; Emery, K.; Chen, C.-C.; Gao, J.; Li, G.; Yang, Y. *Nat. Commun.* **2013**, 4, 1446.

(13) You, J.; Chen, C.-C.; Hong, Z.; Yoshimura, K.; Ohya, K.; Xu, R.; Ye, S.; Gao, J.; Li, G.; Yang, Y. *Adv. Mater.* **2013**, 25, 3973.

(14) Walker, B.; Kim, C.; Nguyen, T.-Q. *Chem. Mater.* **2011**, 23, 470.

(15) Anthony, J. E. *Chem. Mater.* **2011**, 23, 583.

(16) Szarko, J. M.; Guo, J.; Rolczynski, B. S.; Chen, L. X. *Nano Rev.* **2011**, 2, 7249.

(17) Lin, Y.; Li, Y.; Zhan, X. *Chem. Soc. Rev.* **2012**, 41, 4245.

(18) Mishra, A.; Bäuerle, P. *Angew. Chem. Int. Ed.* **2012**, 51, 2020.

(19) Chen, Y.; Wan, X.; Long, G. *Acc. Chem. Res.* **2013**, 46, 2645.

(20) Coughlin, J. E.; Henson, Z. B.; Welch, G. C.; Bazan, G. C. *Acc. Chem. Res.* **2014**, 47, 257.

(21) Roncali, J.; Leriche, P.; Blanchard, P. *Adv. Mater.* **2014**, 26, 3821.

(22) Jarosz, T.; Lapkowski, M.; Ledwon, P. *Macromol. Rapid Commun.* **2014**, 35, 1006.

(23) Steinmann, V.; Kronenberg, N. M.; Lenze, M. R.; Graf, S. M.; Hertel, D.; Meerholz, K.; Bürckstümmer, H.; Tulyakova, E. V.; Würthner, F. *Adv. Energy Mater.* **2011**, 1, 888.

(24) Lin, L.-Y.; Chen, Y.-H.; Huang, Z.-Y.; Lin, H.-W.; Chou, S.-H.; Lin, F.; Chen, C.-W.; Liu, Y.-H.; Wong, K.-T. *J. Am. Chem. Soc.* **2011**, 133, 15822.

(25) Fitzner, R.; Reinold, E.; Mishra, A.; Mena-Osteritz, E.; Ziehlke, H.; Körner, C.; Leo, K.; Riede, M.; Weil, M.; Tsaryova, O.; Weiβ, A.; Uhrich, C.; Pfeiffer, M.; Bäuerle, P. *Adv. Funct. Mater.* **2011**, 21, 897.

(26) Zhou, J.; Wan, X.; Liu, Y.; Long, G.; Wang, F.; Li, Z.; Zuo, Y.; Li, C.; Chen, Y. *Chem. Mater.* **2011**, 23, 4666.

(27) Wei, G.; Xiao, X.; Wang, S.; Zimmerman, J. D.; Sun, K.; Diev, V. V.; Thompson, M. E.; Forrest, S. R. *Nano Lett.* **2011**, 11, 4261.

(28) Sun, Y.; Welch, G. C.; Leong, W. L.; Takacs, C. J.; Bazan, G. C.; Heeger, A. J. *Nat. Mater.* **2012**, 11, 44.

(29) Liu, X.; Sun, Y.; Perez, L. A.; Wen, W.; Toney, M. F.; Heeger, A. J.; Bazan, G. C. *J. Am. Chem. Soc.* **2012**, 134, 20609.

(30) Chen, G.; Sasabe, H.; Wang, Z.; Wang, X.-F.; Hong, Z.; Yang, Y.; Kido, J. *Adv. Mater.* **2012**, 24, 2768.

(31) Talapin, D. V.; Nelson, J. H.; Shevchenko, E. V.; Aloni, S.; Sadtler, B.; Alivisatos, A. P. *Nano Lett.* **2007**, 7, 2951.

(32) Dayal, S.; Reese, M. O.; Ferguson, A. J.; Ginley, D. S.; Rumbles, G.; Kopodakis, N. *Adv. Funct. Mater.* **2010**, 20, 2629.

(33) Lim, J.; Lee, D.; Park, M.; Song, J.; Lee, S.; Kang, M. S.; Lee, C.; Char, K. *J. Phys. Chem. C* **2014**, 118, 3942.

(34) Roquet, S.; De Bettignies, R.; Leriche, P.; Cravino, A.; Roncali, J. *J. Mater. Chem.* **2006**, 16, 3040.

(35) Lin, Z.; Bjorgaard, J.; Yavuz, A. G.; Köse, M. E. *J. Phys. Chem. C* **2011**, 115, 15097.

(36) We have started out on tetrathienylsilane cored tetrapod similar to the one reported herein. However, the aldehyde intermediates decomposed during the Knoevenegal condensation reactions owing to silicon-carbon bond cleavages.

(37) Spano, F. C. *Acc. Chem. Res.* **2010**, 43, 429.

(38) Lai, L. F.; Love, J. A.; Sharenko, A.; Coughlin, J. E.; Gupta, V.; Tretiak, S.; Nguyen, T.-Q.; Wong, W.-Y.; Bazan, G. C. *J. Am. Chem. Soc.* **2014**, 136, 5591.

(39) Murgatroyd, P. N. *J. Phys. D: Appl. Phys.* **1970**, 3, 151.

(40) De Luca, G.; Treossi, E.; Liscio, A.; Mativetsky, J. M.; Scolaro, L. M.; Palermo, V.; Samorì, P. S. *J. Mater. Chem.* **2010**, 20, 2493.

(41) Sinturel, C.; Vayer, M.; Morris, M.; Hillmyer, M. A. *Macromolecules* **2013**, 46, 5399.

(42) Zhang, C.; Matos, T.; Li, R.; Sun, S.-S.; Lewis, J. E.; Zhang, J.; Jiang, X. *Polym. Chem.* **2010**, 1, 663.

(43) Qin, Y.; Hillmyer, M. A. *Macromolecules* **2009**, 42, 6429.

(44) Kim, J. Y.; Qin, Y.; Stevens, D. M.; Ugurlu, O.; Kalihari, V.; Hillmyer, M. A.; Frisbie, C. D. *J. Phys. Chem. C* **2009**, 113, 10790.

(45) Jestin, I.; Frère, P.; Blanchard, P.; Roncali, J. *Angew. Chem. Int. Ed.* **1998**, 37, 942.

(46) Yang, G.; Hu, K.; Qin, Y. *J. Polym. Sci. A Polym. Chem.* **2014**, 52, 591.

(47) Olejnik, E.; Pandit, B.; Basel, T.; Lafalce, E.; Sheng, C.-X.; Zhang, C.; Jiang, X.; Vardeny, Z. V. *Phys. Rev. B* **2012**, 85, 235201.

(48) Musser, A. J.; Al-Hashimi, M.; Maiuri, M.; Brida, D.; Heeney, M.; Cerullo, G.; Friend, R. H.; Clark, J. *J. Am. Chem. Soc.* **2013**, 135, 12747.

(49) Qi, B.; Wang, J. *J. Mater. Chem.* **2012**, 22, 24315.

(50) Khlyabich, P. P.; Burkhart, B.; Thompson, B. C. *J. Am. Chem. Soc.* **2011**, 133, 14534.

(51) Khlyabich, P. P.; Burkhart, B.; Rudenko, A. E.; Thompson, B. C. *Polymer* **2013**, 54, 5267.

(52) W. He, Y. Jiang and Y. Qin, *Polym. Chem.*, **2014**, 5, 1298.

(53) Pu, S.; Zheng, C.; Sun, Q.; Liu, G.; Fan, C. *Chem. Commun.* **2013**, 49, 8036.

(54) Grisorio, R.; De Marco, L.; Allegretta, G.; Giannuzzi, R.; Suranna, G. P.; Manca, M.; Mastrorilli, P.; Gigli, G. *Dyes Pigments* **2013**, 98, 221.

(55) Amir, E.; Sivanandan, K.; Cochran, J. E.; Cowart, J. J.; Ku, S.-Y.; Seo, J. H.; Chabinyc, M. L.; Hawker, C. J. *J. Polym. Sci. A Polym. Chem.* **2011**, 49, 1933.

(56) Crouch, D. J.; Sparrowe, D.; Heeney, M.; McCulloch, I.; Skabara, P. J. *Macromol. Chem. Phys.* **2010**, 211, 2642.

Chapter 3

A Molecular Tetrapod for Organic Photovoltaics

(Reproduced with permission from

ACS Applied Materials and Interfaces **2016**, 8 (34), pp 22392-22401.

Copyright © 2016 American Chemical Society

The other authors, Zhen Zhang is acknowledged.

Supporting information of the publication is incorporated in this chapter)

3.1 Introduction

In previous chapter, we have discussed breakwater-like tetrapod **SO** (Scheme 1) containing a tetraphenylsilane core and four cyanoester functionalized terthiophene arms. The tetrapod was found to be very hard to crystallize, which led to molecularly mixed blends with [6,6]-phenyl-C_{61}-butyric acid methyl ester ($PC_{61}BM$) and thus poor solar cell performances.[1] We speculated that the slow crystallization behavior of **SO** was intrinsically resulted from the structure of each of its arms, since the same crystallization behavior was found in **MO** (Scheme 1). Thus, we conjecture that we may be able to increase the crystallization kinetics of these tetrapods by removing the alkyl side chains in the middle of each arm and by using more rigid and planar electron-accepting moieties such as the fluorinated benzothiadiazole (FBTD) units. Meanwhile, recent studies have suggested that the introduction of fluorine atoms can increase internal dipole moments of conjugated molecules, which provides extra driving forces to induce phase separations within the blend films.[2-4] Furthermore, the strongly electron-withdrawing effects of fluorine atoms can lower the energies of both the lowest unoccupied molecular orbital (LUMO) and the highest occupied molecular orbital (HOMO) without significantly

affecting the bandgaps of conjugated molecules.[5] Therefore, the deepened HOMO level can potentially lead to increased open-circuit voltage (V_{OC}) values without changing the desired light harvesting properties.[6] Herein, we report the synthesis, characterization and application in OSCs of a stable medium bandgap molecular tetrapod, **SFBTD**, containing a tetraphenylsilane core and four arms composed of one FBTD and three thiophene units. **SFBTD** shows excellent solution processability and thermal stability, broad and strong absorption and appropriate energy levels relative to fullerene acceptors. Solution-processed BHJ OSCs based on **SFBTD**/$PC_{61}BM$ without any additives and interfacial engineering exhibit *PCE*s as high as 1.05 % with high V_{OC} values up to 1.02 V. To the best of our knowledge, this is the highest *PCE* reported for devices using molecular tetrapods as donor materials OSCs.

Scheme 3.1 Structures of **SO** and **MO** from our previous report.[1]

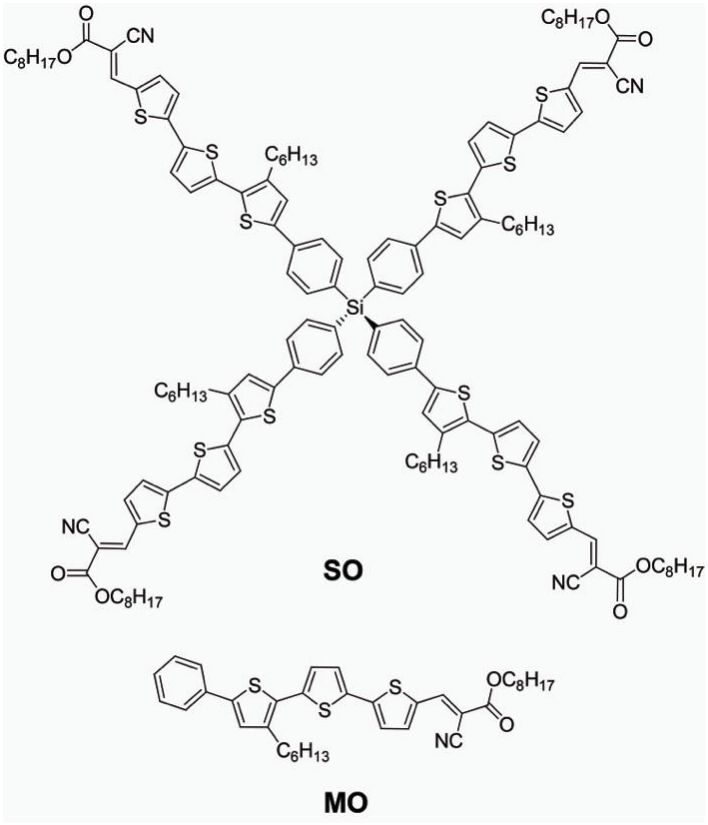

3.2 Synthesis and Characterization

3.2.1 Synthesis of SFBTD and MFBTD

Synthetic details for the molecular tetrapod **SFBTD**, and the linear model compound **MFBTD**, are summarized in Scheme 3.2 and included in the experimental section. Compound **9** was synthesized according to previous reported procedures.[1] Compound **10** was prepared from **9** through Suzuki coupling reactions with bis(pinacolato)diboron. Compounds **9** and **10** can conveniently serve as common cores for constructing different 3-D molecular tetrapods by grafting with different arms. After Suzuki coupling reactions of **10** with four equivalents of **8**, **SFBTD** was obtained by column chromatography and shows excellent solubility in common processing solvents such as $CHCl_3$, tetrahydrofuran (THF) and nonpolar aromatic solvents. The 2-hexyldecyl side chains on **SFBTD** are necessary to ensure solubility of the tetrapod, since initial attempts at preparing **SFBTD** analogues without alkyl side chains and with linear alkyl side chains all failed due to precipitation of reaction intermediates. ^{1}H and ^{13}C NMR spectroscopy were employed to characterize the newly prepared compounds, which match well with proposed structures. The tetrapodal structure of **SFBTD** was confirmed by high-resolution mass spectrometry (HR-MS), giving a measured molar mass of 2825.7766 [M^+] that matches reasonably well with the calculated value of 2824.9255 [M^+]. The slightly larger than expected discrepancy is presumably caused by the significantly lower molar mass of the calibration standard applied (cholesterol, m/z = ca. 369). In order to supplement the HR-MS experiments, we have also performed elemental analysis on **SFBTD**, giving measured elemental contents of C, H, N at 67.95, 6.54, and 3.75%, matching well with the calculated values at 67.95, 6.27, and 3.96%, respectively.

Scheme 3.2 Synthesis of **SFBTD** and **MFBTD**.

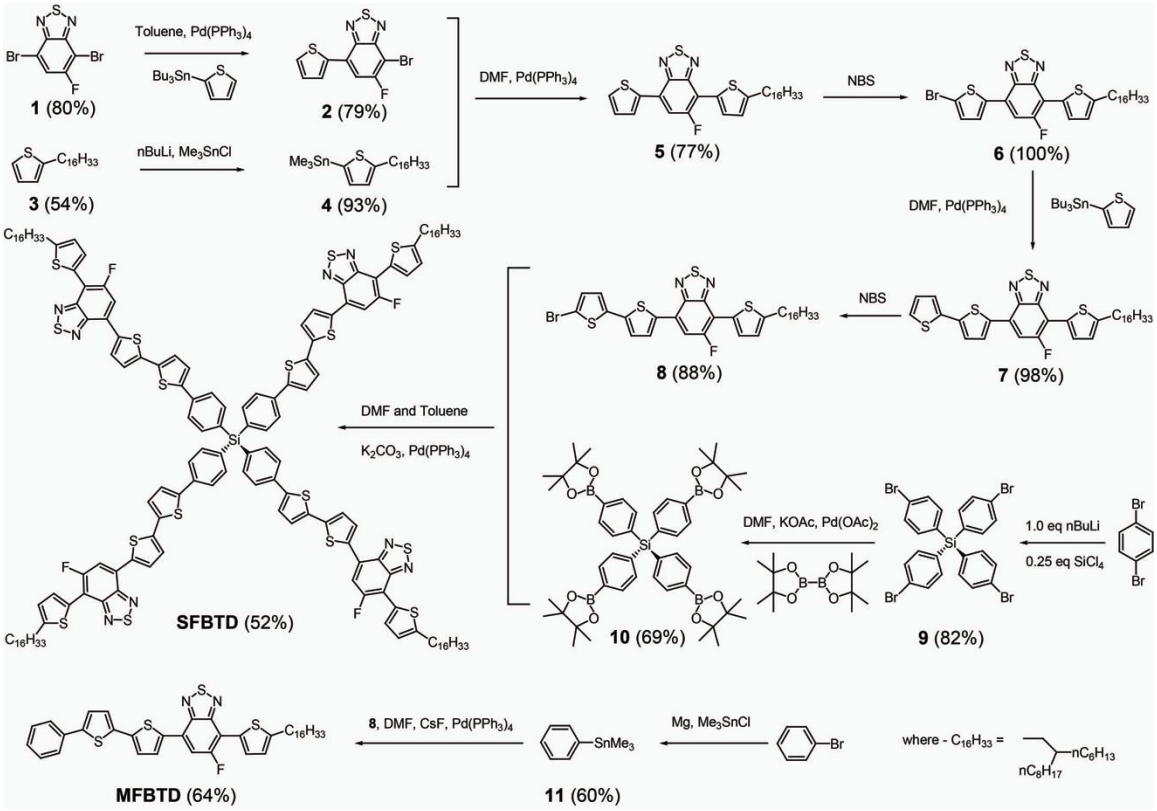

3.2.2 UV-vis Absorption, Fluorescence Spectroscopies and TD-DFT Calculations

We employed UV-vis absorption and fluorescence spectroscopies to investigate the electronic properties of **SFBTD** and **MFBTD** in both dilute solutions and as thin films (Figure 3.1). Chlorobenzene solutions (10^{-5} M) of **SFBTD** and **MFBTD** exhibit almost identical absorption profiles that are structureless with two major transition peaks at ca. 504 nm and 384 nm, and indistinguishable fluorescence spectra with λ_{em}'s at ca. 620 nm. The emission quantum efficiencies of **SFBTD** and **MFBTD** are calculated to be also similar, at 3.4% and 4.1%, respectively. The similarity in solution optical properties between **SFBTD** and **MFBTD** suggests that the four conjugated arms of **SFBTD** have negligible electronic communications. We assign the electronic transition at 504 nm to intramolecular charge transfer (ICT) transition and the other at 384 nm to largely π-π*

transition mixed with certain degrees of ICT character. We base these assignments on time dependent density functional theory (TD-DFT) calculations as shown in Figure 3.2 The geometry optimization was performed on **MFBTD**, with a methyl group replacing the long alkyl side-chain, using the B3LYP functional and the 6-31G* basis set in Gaussian 09.[7] TD-DFT was performed on the optimized geometry only using the same functional and basis set. Two bright singlet states, namely S1 and S3, having transition energies at 2.07 and 3.02 eV, corresponding to transitions from HOMO to LUMO and HOMO to LUMO+1 orbitals, respectively, are found. The S1 state clearly has charge transfer characteristics with hole density delocalized throughout the entire chromophore while the electron density is mainly localized at the electron poor FBTD unit. The S3 state, on the other hand, possess largely π-π^* character with large overlap between the hole and electron densities. From the simulated absorption spectrum, the S3 state transition energy more closely matches that of the high energy absorption peak at 384 nm (3.02 eV vs. 3.22 eV), while the S1 state transition energy is much lower than observed (2.07 eV vs. 2.46 eV), since TD-DFT is known to have difficulties in estimating energies of charge transfer states.[8]

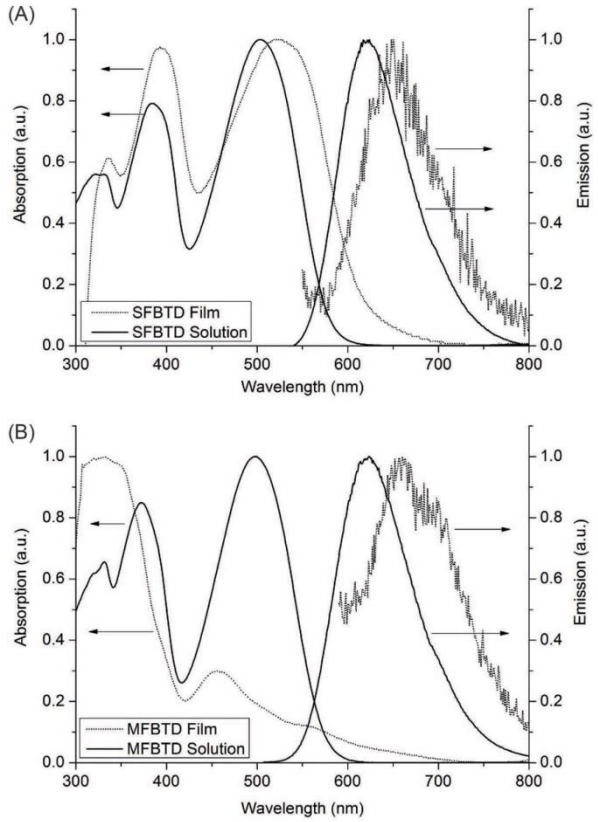

Figure 3.1 UV-vis absorption (left axis) and emission (right axis) spectra of (A) **SFBTD** and (B) **MFBTD** in chlorobenzene solutions (10^{-5} M, solid lines) and as thin films (dashed lines).

The extinction coefficient (ε) of **SFBTD** is calculated to be ca. 1.3×10^5 L mol^{-1} cm^{-1} based on concentrations of the molecular tetrapod, corresponding to an $\varepsilon = 3.3 \times 10^4$ L mol^{-1} cm^{-1} for each of its arms. **MFBTD**, on the other hand, displays an $\varepsilon = 2.8 \times 10^4$ L mol^{-1} cm^{-1} in solution. The seemingly stronger absorption observed for **SFBTD**, on per arm basis, is presumably caused by its more isotropic structure and thus larger absorption cross-section.[9] As expected form the differences in molecular shapes, **SFBTD** and **MFBTD** show very different behaviors in thin films. The as-cast thin film of **SFBTD** displays a λ_{max} at ca. 525 nm, which is slightly red-shifted from that of the solution profile by 25 nm. The red shift is likely a solid state phenomenon in which the conjugated

chains become slightly more planar due to packing interactions, thus leading to longer conjugation lengths and lower transition energies. The fluorescence of **SFBTD** films is very weak, having a λ_{em} at ca. 650 nm when excited at the λ_{max}, which gives a large Stoke's shift of 125 nm. Interestingly, the two major electronic transitions of **MFBTD** are both blue-shifted in thin films. The ICT peak shifts to 457 nm, and a shoulder peak at ca. 550 nm is observed that matches well with the ICT transition of **SFBTD** thin films. We conjecture that **MFBTD** behave similarly to **SFBTD** in the solid state and, due to its linear shape, **MFBTD** can form H-type aggregates, leading to the observed blue-shift in absorption spectra.[10] Emission of **MFBTD** films is thus expectedly quenched to a large extent and only a weak fluorescence peaked at ca. 660 nm can be observed. The optical band gaps of **SFBTD** and **MFBTD** are thus estimated from the absorption edges to be both ca. 2.2 eV in solutions and 2.0 eV in thin films, respectively.

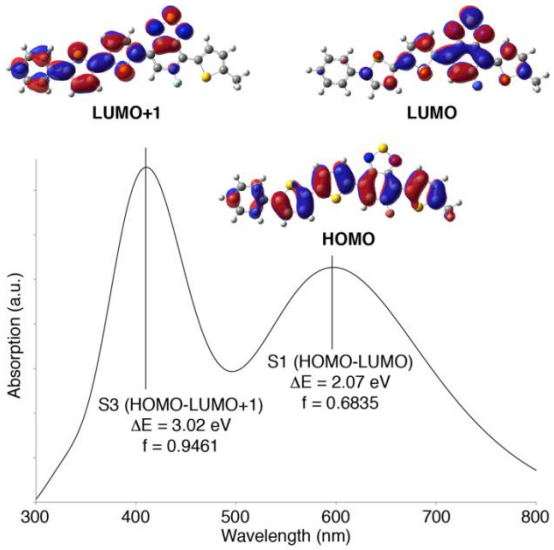

Figure 3.2 Time dependent density functional theory (TD-DFT, B3LYP, 6-31G*) calculation results of **MFBTD** (the long alkyl side-chain is replaced with a methyl group for computation economy). The HOMO, LUMO and LUMO+1 orbitals and simulated UV-vis absorption spectrum are shown; ΔE: transition energy; f: oscillator strength.

3.2.3 Cyclic Voltammetry Measurement

The frontier energy levels and bandgaps of **SFBTD** and **MFBTD** in solution and thin film state are estimated by using cyclic voltammetry (CV). The recorded voltammograms were referenced externally to ferrocene/ferrocenium (Fc/Fc^+) redox couple (4.80 eV below vacuum). Therefore, the HOMO and LUMO energy levels can be estimated using the empirical formula $E_{HOMO} = -(E_{ox}^{onset} + 4.80)$ eV and $E_{LUMO} = -(E_{red}^{onset} + 4.80)$ eV, respectively. As depicted in Figure 3.3, very similar redox behaviors of both **SFBTD** and **MFBTD** are observed in both solutions and thin films. In solutions, two quasi-reversible oxidation waves with onsets at ca. 0.4 V and 0.9 V for **SFBTD** and at ca. 0.5 V and 0.8 V for **MFBTD** are observed. Two quasi-reversible reduction waves with onsets at ca. −1.6 V and – 2.1 V are recorded for both **SFBTD** and **MFBTD**. From onsets of the first oxidation and reduction waves, the HOMO and LUMO levels of **SFBTD** are estimated to be –5.2 eV and –3.2 eV, while the HOMO and LUMO levels of **MFBTD** are estimated to be –5.3 eV and –3.2 eV, respectively. Therefore, electrochemical bandgaps of 2.0 eV and 2.1 eV are calculated for **SFBTD** and **MFBTD**, respectively, agreeing reasonably well with the results of UV-vis measurements. In thin films, four irreversible oxidation waves and three quasi-reversible reduction waves are observed in both **SFBTD** and **MFBTD** thin film. The onsets of first oxidation and reduction waves are located at ca. 0.7 V and -1.3 V for **SFBTD** and at ca. 0.6 V and -1.4 V for **MFBTD**, respectively. The HOMO and LUMO levels of **SFBTD** in solid state are thus estimated, respectively, at –5.5 eV and –3.5 eV, while the HOMO and LUMO levels of **MFBTD** are estimated to be –5.4 eV and –3.4 eV, respectively. Thus, electrochemical

bandgap of both **SFBTD** and **MFBTD** thin film are calculated as 2.0 eV, matching well with UV-vis measurement.

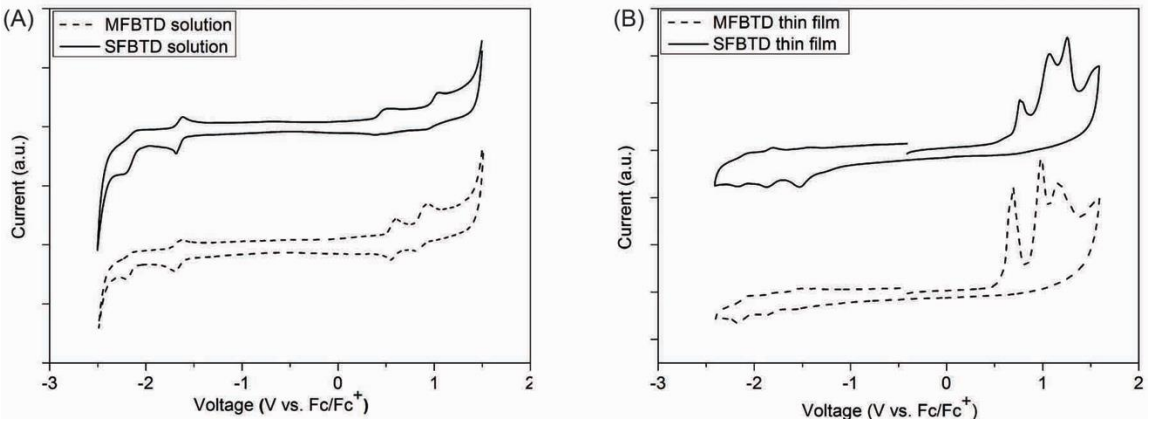

Figure 3.3 Cyclic voltammograms (CV) of (A) **SFBTD** and **MFBTD** in CH_2Cl_2 solutions (1 mM) and (B) **SFBTD** and **MFBTD** thin film in acetonitrile solutions containing Bu_4NPF_6 as the supporting electrolytes (0.1 M). The voltages are referenced externally to ferrocene (Fc) redox couple. Scan rate: 100 mV/s.

3.2.4 DSC Measurement

Thermal properties of **SFBTD** and **MFBTD** were studied by differential scanning calorimetry (DSC) measurements and the results are displayed in Figure 3.4. Unlike the slow crystallization kinetics observed for the similar model compound **MO** we reported previously[1] and for a structurally twisted linear conjugated small molecule reported by Bazan *et al*.,[11] **MFBTD** shows much enhanced crystallinity. At a typical scanning rate of 10 °C/min, **MFBTD** displays two melting transitions at 46 °C and 115 °C in the heating event and two crystallization transitions at 28 °C and 108 °C upon cooling. At the same scanning rate of 10 °C/min, however, **SFBTD** shows an exothermic crystallization transition peak at 150 °C and one melting transition at 183 °C. No crystallization event is observed in the cooling curve. On the other hand, at a slower scanning rate of 1 °C/min, the crystallization transition is only observed during the cooling event at ca. 140 °C. Such

behavior indicates slow crystallization kinetics of **SFBTD**, which was also found in our previously reported molecular tetrapod **SO** and its model compound **MO**. As a result, the slow crystallization kinetics of **SFBTD**, as well as that of **SO**, is most likely caused by their 3-D molecular geometry and not intrinsically by the nature of the constituting arms as we previously speculated. Such solid-state characteristics of **SFBTD** and **MFBTD** are further confirmed by using X-ray diffraction (XRD) experiments on thin films drop cast onto glass substrates from chlorobenzene solutions, as shown in Figure 3.5. No obvious scattering peaks are observed in the thin films of **SFBTD**, while in the thin films of **MFBTD** two sharp scattering peaks are observed at 2θ values of ca. 2.8° and 3.2°, which correspond to *d*-spacings of ca. 3.2 and 2.8 nm, respectively. This indicates that **MFBTD** exhibits better crystallinity and more ordered solid-state packing than **SFBTD**, as found in our DSC studies.

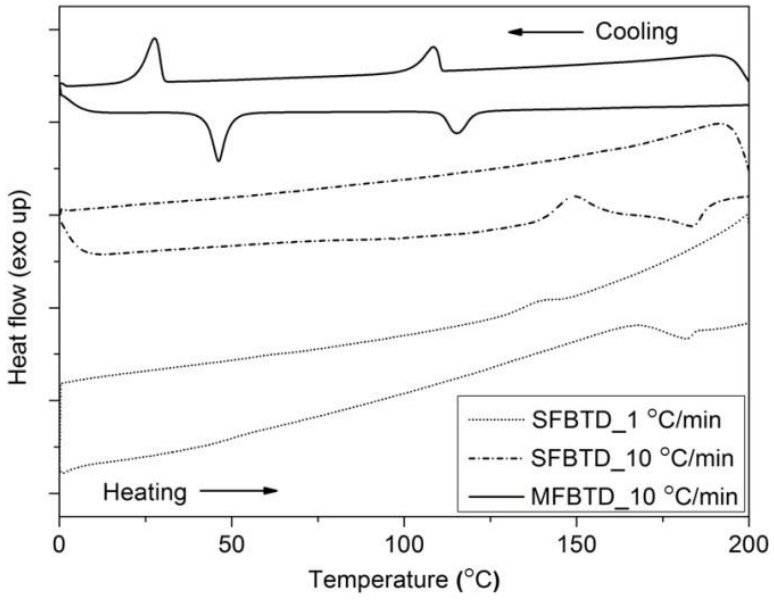

Figure 3.4 Differential scanning calorimetry (DSC) histograms of **MFBTD** at 10 °C/min (solid line); and of **SFBTD** at scanning rates of 10 °C/min (short dash dot line) and at 1 °C/min (dot line). Second heating and cooling curves are shown.

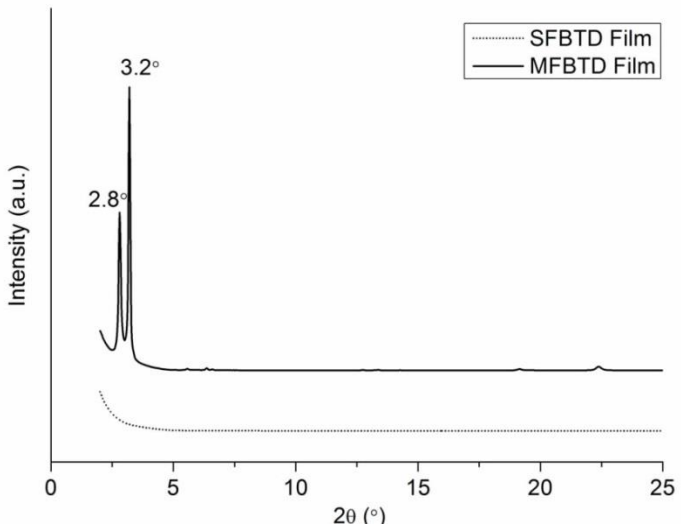

Figure 3.5 X-ray diffraction (XRD) profiles of **SFBTD** and **MFBTD** thin films deposited on glass substrates.

3.3 Binary Blend Devices

We firstly fabricated BHJ OPV devices by adopting conventional devices geometries: ITO glass/MoO_3 (10 nm)/active layer /Al (100 nm). The active layer was prepared by spin-coating the chloroform blend solution of **SFBTD** or **MFBTD** and $PC_{61}BM$ (American Dye Source, Inc.) at predetermined weight ratios. Optimization of OPV devices was thoroughly investigated by changing the thermal annealing temperature, and the best condition was found to be thermal annealing at 80 °C for 15 min. Photovoltaic performances of devices by representative fabrication conditions are summarized in Table 3.1, and the current density-voltage (I-V) curves of the best performing devices from each compound are shown in Figure 3.6. Under optimized fabrication conditions, devices from **SFBTD** consistently out-perform those using **MFBTD**. Both **SFBTD** and **MFBTD** devices show relatively high open circuit voltage (V_{OC}) values up to 0.88 V and 0.85 V, respectively, which is relatively insensitive to the donor/acceptor ratios and as expected from the deep lying HOMO levels of these

molecules. Devices employing **SFBTD**/$PC_{61}BM$ at a weight ratio of 1/4 and **MFBTD**/$PC_{61}BM$ at a weight ratio of 1/2 give the best performance. The best **SFBTD** device has a short circuit current (J_{SC}) of 3.64 mA/cm^2, a fill factor (*FF*) of 33% and the *PCE* of ca. 1.05%, which is the highest *PCE* reported for binary organic solar cells employing molecular tetrapods. While the best **MFBTD** device displays a J_{SC} of 2.41 mA/cm^2 and a *FF* of 27%, leading to *PCE* of ca. 0.55%. Both **SFBTD** and **MFBTD** devices suffer greatly from low J_{SC} and *FF* values. We believe that significant charge recombination is responsible for the low current and *FF* values, which is suggested by the steep increases in current densities at reverse bias for both devices under light. We also observed similar behaviors for our previous molecular tetrapod **MO**, for which we found that inferior blend morphologies and low charge mobilities were mainly responsible for the low device performances.[1] We thus employed optical microscopy to study the morphologies of neat films of **SFBTD** and **MFBTD** as well as those of corresponding $PC_{61}BM$ blend films, and the micrographs are included in Figure 3.7.

Table 3.1 Summary of Device Performance Data of Organic Solar Cells Employing **SFBTD** and **MFBTD** under Various Fabrication Conditions.[a]

	Ratios[b]	V_{OC} (V)	J_{SC} (mA/cm^2)	*FF* (%)	*PCE* (%)
SFBTD/ $PC_{61}BM$	2.5 / 7.5	0.87 ± 0.04 (0.90)	2.84 ± 0.17 (3.09)	30 ± 0.89 (31)	0.74 ± 0.04 (0.81)
	2.5 / 10.0	0.88 ± 0.03 (0.92)	3.64 ± 0.17 (3.86)	33 ± 1.83 (35)	1.05 ± 0.06 (1.11)
	2.5 / 12.5	0.85 ± 0.01 (0.86)	2.46 ± 0.11 (2.62)	31 ± 0.42 (32)	0.66 ± 0.02 (0.69)
MFBT/ $PC_{61}BM$	2.5 / 2.5	0.74 ± 0.02 (0.77)	1.15 ± 0.13 (1.41)	27 ± 0.97 (28)	0.23 ± 0.02 (0.28)
	2.5 / 5.0	0.85 ± 0.01 (0.86)	2.41 ± 0.10 (2.61)	27 ± 0.35 (27)	0.55 ± 0.03 (0.58)
	2.5 / 7.5	0.79 ± 0.02 (0.81)	1.17 ± 0.15 (1.29)	28 ± 0.56 (28)	0.25 ± 0.03 (0.28)

[a] All devices were thermally annealed at 80 °C for 15 min; results are reported as averages of five individual cells; the highest values are given in parentheses. [b] All ratios by weight.

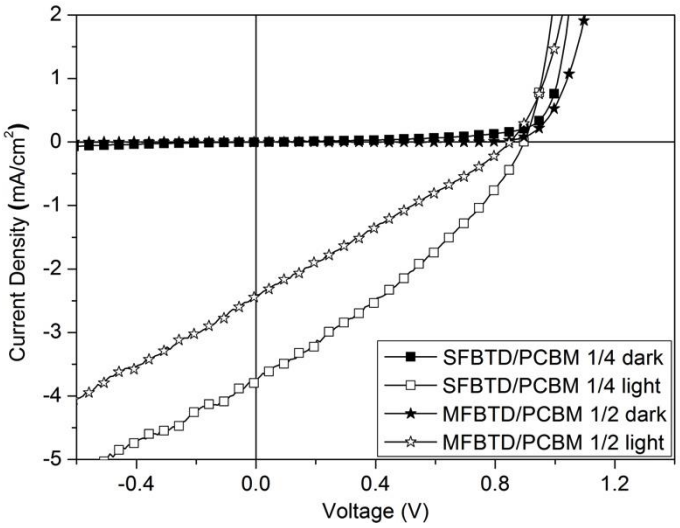

Figure 3.6 Current density-voltage (I-V) curves of the best performing devices employing **SFBTD**/$PC_{61}BM$ (1/4, wt./wt.) and **MFBTD**/$PC_{61}BM$ (1/2, wt./wt.) under simulated white light (100 mW/cm^2).

SFBTD thin films either as cast or thermally annealed at 80 °C and 150 °C for 15 min all show smooth morphologies that are free of any visible aggregates or crystallites (Figure 3.7A-C). The lack of any visible aggregates or crystallites in thermally annealed film of **SFBTD** is consistent with the low crystallinity of **SFBTD** we found in DSC studies. Therefore, it's not surprising that blend films containing **SFBTD**/$PC_{61}BM$ (1/4, wt./wt.) do not display crystalline features (Figure 3D) even after annealing at 80 °C and 150 °C for 15 min (Figure 3E and 3F, respectively). This lack of phase separation into pure domains of electron donors and acceptors can significantly limit charge transport and lead to large rates of charge recombination. On the other hand, **MFBTD** thin films show strong intendancy to crystallize. Clear and sparse needle-like crystallites can be observed in the as-cast films of **MFBTD** (Figure 3G). These crystalline features become more pronounced and form large amount of needle-like crystals after thermal annealing at 80 °C for 15 min (Figure 3H). Surprisingly, these crystallites completely disappeared

after thermal annealing at 150 °C for 15 min (Figure 3I). Even though **MFBTD** neat film show strong intendancy to crystallize, fresh blend films of **MFBTD**/$PC_{61}BM$ (1/2, wt./wt.) including as-cast and thermal annealed at 80 °C or 150 °C for 15 min doesn't show any phase separation. In addition, there are no fullerene crystallites found even after thermal annealing at 150 °C for 15 min. Interestingly, these blend films are left at room temperature for several days, many crystals are observed, as shown in (Figure 3J-L). This indicates that **MFBTD** becomes hard to crystallize once they are blended with $PC_{61}BM$.

The hole mobilities in neat films and BHJ blend films are measured by space-charge limited current (SCLC) method with the hole-selective device structure: ITO/MoO_3/organic layer/MoO_3/Al (Figure 3.8).[12] All neat films and blend films are thermally annealed at 80 °C for 15 min before testing. Hole mobility of neat **SFBTD** film is ca. 2.0×10^{-6} $cm^2 V^{-1} s^{-1}$, which drastically decreases to ca. 5.9×10^{-8} $cm^2 V^{-1} s^{-1}$ in the blend films of **SFBTD**/$PC_{61}BM$ (1/4, wt./wt.). The neat **MFBTD** film displays a better hole mobility of ca. 1.7×10^{-4} $cm^2 V^{-1} s^{-1}$, which is consistent with the observed better crystallinity of **MFBTD**. In the blend film of **MFBTD**/$PC_{61}BM$ (1/2, wt./wt.), the hole mobility also decreases to ca. 6.2×10^{-6} $cm^2 V^{-1} s^{-1}$. Such low hole mobilities of both **SFBTD** and **MFBTD**, either as neat films or in BHJ, are expected to result in significant charge recombination and thus low J_{SC} and *FF* values.

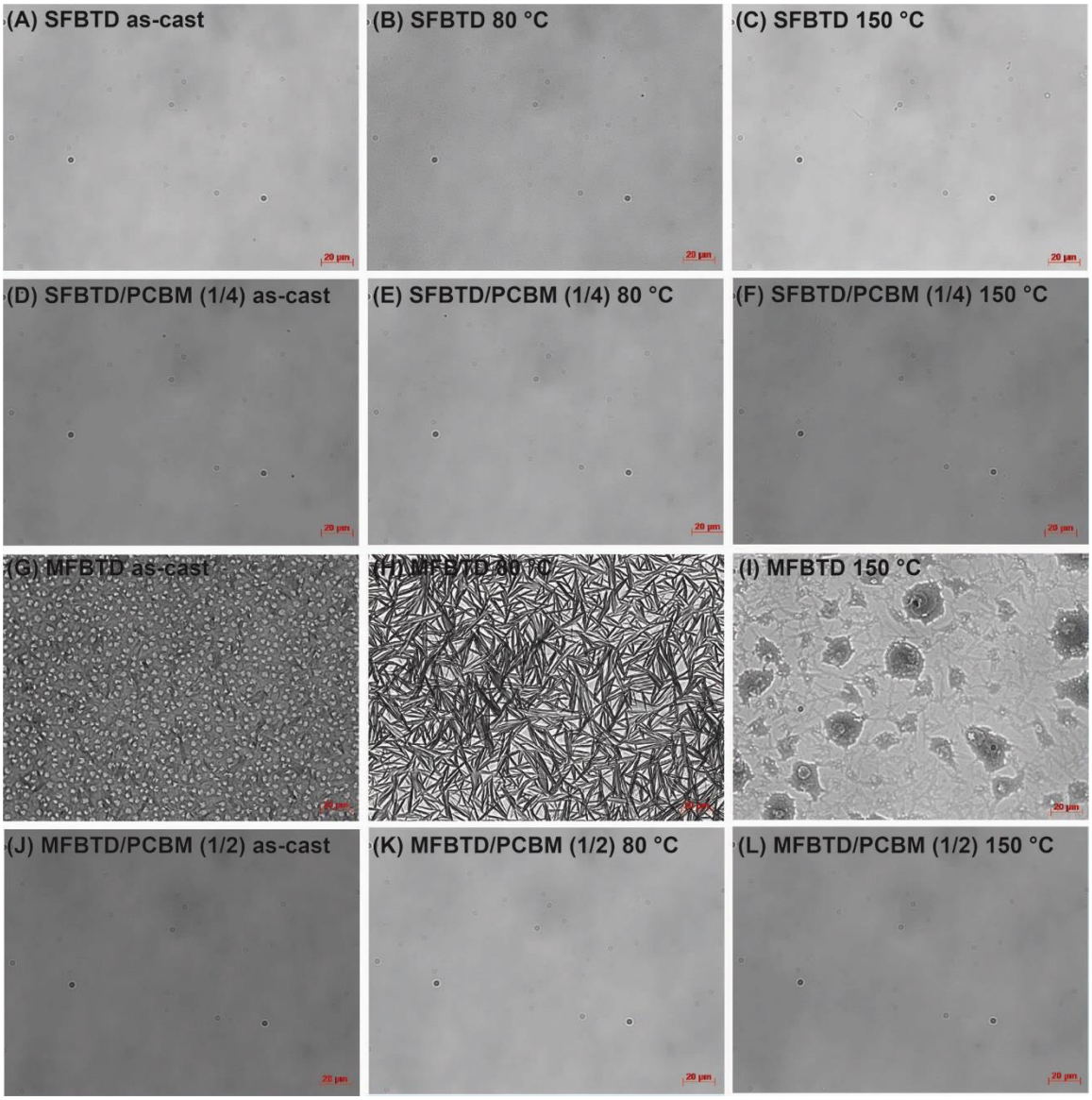

Figure 3.7 Optical micrographs (400 X magnification) of thin films of **SFBTD**, **MFBTD** and corresponding $PC_{61}BM$ blend films under different thermal annealing conditions. Scale bars in all: 20 μm.

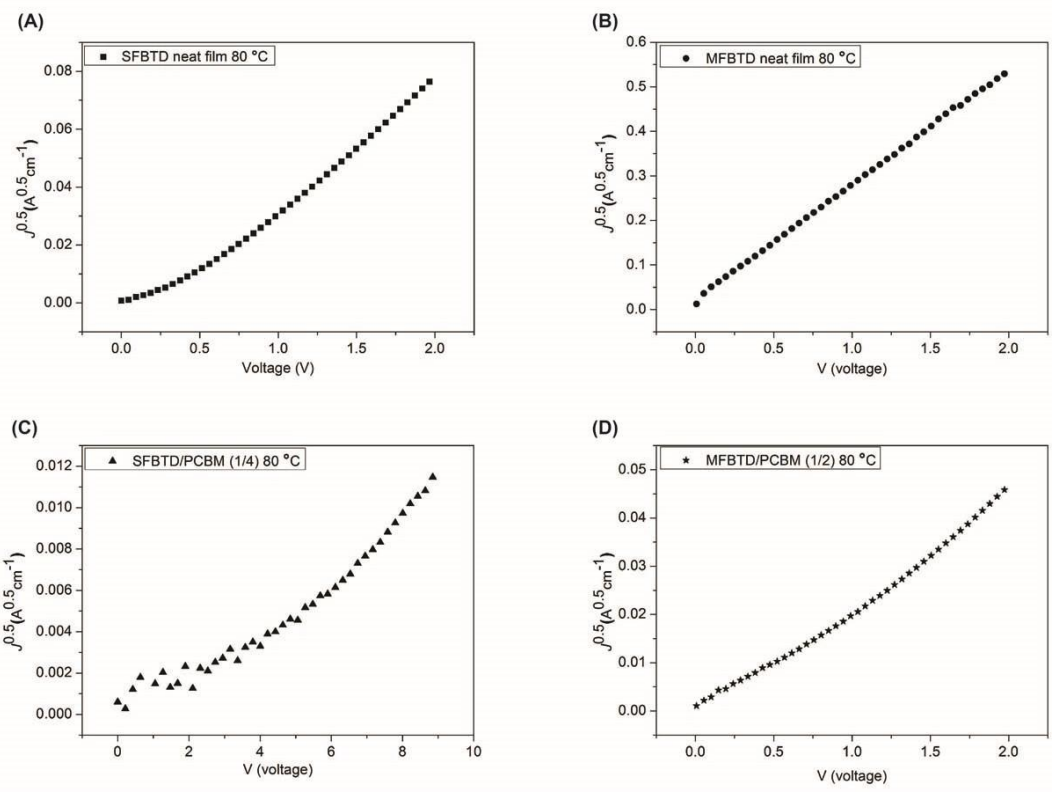

Figure 3.8 Current density-voltage (I-V) curves of hole selective devices containing **SFBTD** (A) and **MFBTD** (B) neat films and their corresponding blend films with $PC_{61}BM$ under optimized device conditions (C and D, respectively).

The external quantum efficiency (EQE) of optimized devices employing **SFBTD** and **MFBTD** devices are shown in Figure 3.9. These devices show broad EQE responses from 300 nm to 700 nm, which matches well with corresponding absorption profiles. The device employing **SFBTD** gives maximum EQE values between 27% and 29% from 330 nm to 600 nm, while the device employing **MFBTD** gives the maximum EQE values between 10% and 13% from 340 nm to 550 nm.

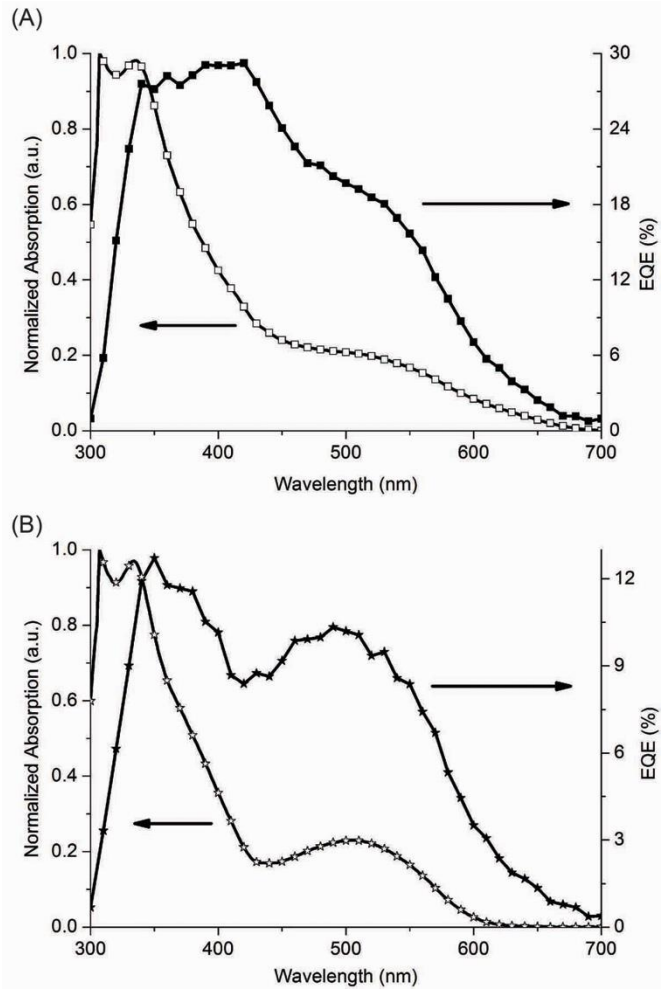

Figure 3.9 External quantum efficiency (EQE, right axis) and normalized absorption spectrum (left axis) of the best performing devices employing (A) **SFBTD**/$PC_{61}BM$ (1/4, wt./wt.) and (B) **MFBTD**/$PC_{61}BM$ (1/2, wt./wt.).

Since the tetrapodal structures are capable of mutual interlock to prevent dislodge, we expect high thermal stability of OSC devices using these molecular tetrapods. Accelerated aging tests were performed on the optimized devices employing **SFBTD** and **MFBTD** by thermal annealing at 80 °C inside a N_2 filled glovebox and tested at pre-determined time intervals. The aging test results are summarized in Figure S7 with device performance details given in Tables 3.2 and 3.3. After aging for 120 hours, devices employing **SFBTD** lost ca. 10% of its original efficiency, while devices employing

MFBTD lost ca. 16%. Aging test of devices employing **SFBTD** continued for a total of 384 hours, after which 87% of the original efficiency was maintained. Interestingly, during the aging tests, V_{OC} values of devices employing both **SFBTD** and **MFBTD** increased initially up to 1.02 V and 0.90 V, respectively, and did not change significantly with time.

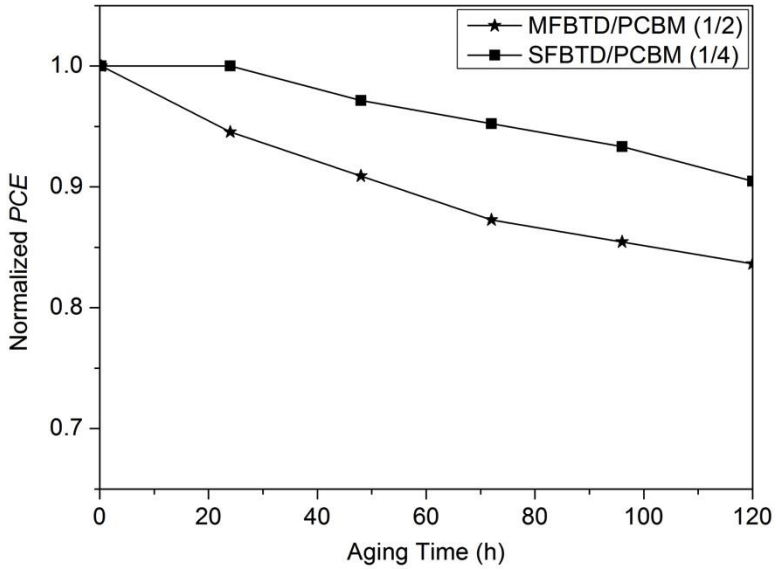

Figure 3.10 Relative *PCE*s of optimized devices employing **SFBTD** and **MFBTD** under accelerated aging conditions (80 °C).

Table 3.2 Performance details of devices employing **SFBTD/PC$_{61}$BM** (1/4, wt./wt.) under accelerated aging conditions (80 °C).

Aging time (h)	*PCE*	J_{SC} (mA/cm^2)	V_{OC} (V)	*FF*
0.25	1.05%	3.64	0.88	0.33
24	1.05%	3.23	1.00	0.33
48	1.02%	3.05	1.01	0.32
72	1.00%	3.14	1.01	0.32
96	0.98%	3.09	1.02	0.31
120	0.95%	3.01	1.02	0.31
144	0.92%	2.98	1.02	0.30
168	0.95%	2.98	1.02	0.31
192	0.94%	2.95	1.02	0.31
216	0.92%	2.93	1.01	0.31

240	0.90%	2.94	1.01	0.31
264	0.90%	2.87	1.02	0.31
288	0.88%	2.66	0.99	0.32
312	0.89%	2.63	1.01	0.31
336	0.93%	2.90	1.01	0.32
360	0.92%	2.89	1.02	0.31
384	0.91%	2.85	1.01	0.31

Table 3.3 Performance details of devices employing **MFBTD/PC$_{61}$BM** (1/2, wt./wt.) under accelerated aging conditions (80 °C).

Aging time (h)	*PCE*	J_{SC} (mA/cm^2)	V_{OC} (V)	*FF*
0.25	0.55%	2.41	0.85	0.27
24	0.52%	2.25	0.90	0.26
48	0.50%	2.19	0.88	0.26
72	0.48%	2.13	0.89	0.25
96	0.47%	2.08	0.89	0.25
120	0.46%	2.08	0.89	0.25

3.4 Ternary Blend Devices

As we demonstrated previously, the inferior morphology and low hole mobilities of **SO**/fullerene blends could be improved by adding a low bandgap and crystalline poly(3-decylthienylene vinylene) (P3DTV)[13-16] polymer (Scheme 3.3). The addition of P3DTV induced appreciable phase separation in the ternary blends and resulted in much enhanced device efficiencies.[35] Meanwhile, the addition of P3DTV, which has a higher lying HOMO level than that of **SFBTD**, can potentially increase the hole mobility by selectively conducting holes through the more conductive conjugated polymer. Thus, we have fabricated OSC devices using **SFBTD**/P3DTV/PC$_{61}$BM ternary blends at different weight ratios. An in-house made P3DTV (M_n = 21.3 kDa, *PDI* = 2.1)[17] was used in the studies. The binary P3DTV/PC$_{61}$BM devices were first fabricated and optimized, in which a weight ratio of 1/1 and a thermal annealing temperature of 80 °C were found to be optimal, leading to a *PCE* of ca. 0.49%. This relatively low efficiency is comparable

to previously reported examples and is possibly caused by the extremely short exciton lifetimes in PTVs.[18-19] Thus, in the ternary blends, we kept the weight ratios of **SFBTD**/$PC_{61}BM$ and P3DTV/$PC_{61}BM$ consistent at 1/4 and 1/1, respectively. Thermal annealing was found to slightly enhance ternary device performances and the optimal temperature was found to be 80 °C, beyond which device deterioration occurred. Table 3.4 summarizes detailed device parameters involving binary and ternary blends of **SFBTD** and P3DTV at different weight ratios.

Scheme 3.3 Structures of PTV derivatives.

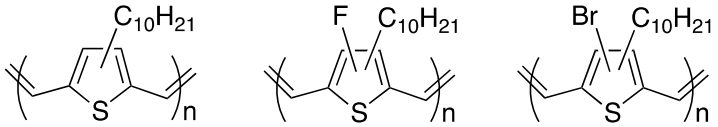

P3DTV **PFDTV** **PBrDTV**

Table 3.4 Binary and Ternary Device Performance Data Employing **SFBTD** and **P3DTV**.[a]

SFBTD/P3DTV/$PC_{61}BM$[b]	V_{OC} (V)	J_{SC} (mA/cm^2)	*FF* (%)	*PCE* (%)
A. 2.5 / 0.0 / 10.0	0.88 ± 0.03 (0.92)	3.64 ± 0.17 (3.86)	33 ± 1.83 (35)	1.05 ± 0.06 (1.11)
B. 2.5 / 0.125 / 10.0	0.57 ± 0.00 (0.57)	2.50 ± 0.25 (2.87)	35 ± 0.49 (36)	0.50 ± 0.04 (0.56)
C. 2.5 / 1.5 / 11.5	0.50 ± 0.00 (0.50)	3.59 ± 0.17 (3.76)	48 ± 0.47 (48)	0.85 ± 0.04 (0.90)
D. 2.5 / 2.5 /12.5	0.50 ± 0.01 (0.51)	3.77 ± 0.27 (4.11)	53 ± 1.50 (55)	1.01 ± 0.05 (1.09)
E. 1.5 / 2.5 / 8.5	0.49 ± 0.01 (0.50)	4.80 ± 0.33 (5.37)	52 ± 1.61 (54)	1.21 ± 0.06 (1.30)
F. 0.5 / 2.5 / 4.5	0.47 ± 0.00 (0.47)	4.33 ± 0.42 (4.96)	50 ± 0.62 (50)	1.01 ± 0.09 (1.15)
G. 0.0 / 2.5 / 2.5[c]	0.45 ± 0.00 (0.45)	2.22 ± 0.14 (2.38)	49 ± 0.84 (50)	0.49 ± 0.03 (0.53)

[a] All devices are thermally annealed at 80 °C for 15 min; results are reported as averages of five individual cells; the highest values are given in parentheses. [b] All ratios by weight. [c] Devices are thermally annealed at 80 °C for 10 min.

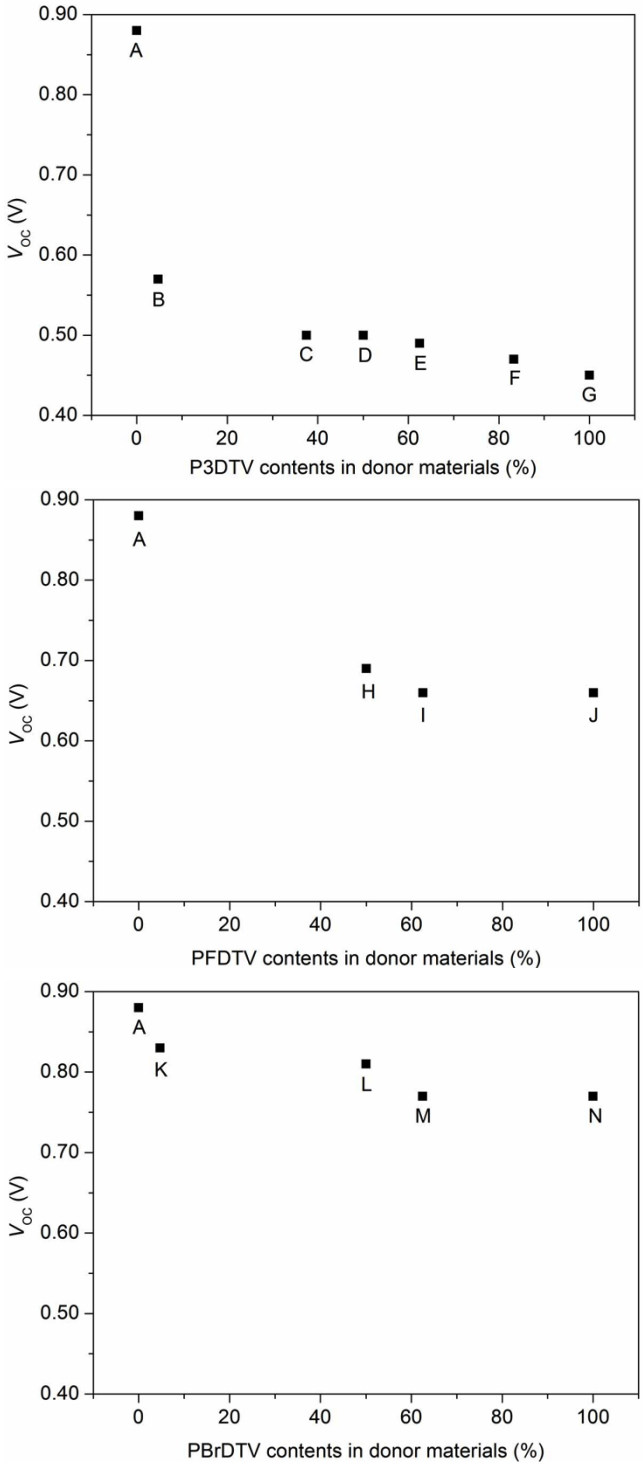

Figure 3.11 Open circuit voltage (V_{OC}) values in ternary blend devices containing **SFBTD** and $PC_{61}BM$ with varying amount of P3DTV, PFDTV and PBrDTV, respectively. See Tables 2 and 3 for labeling details.

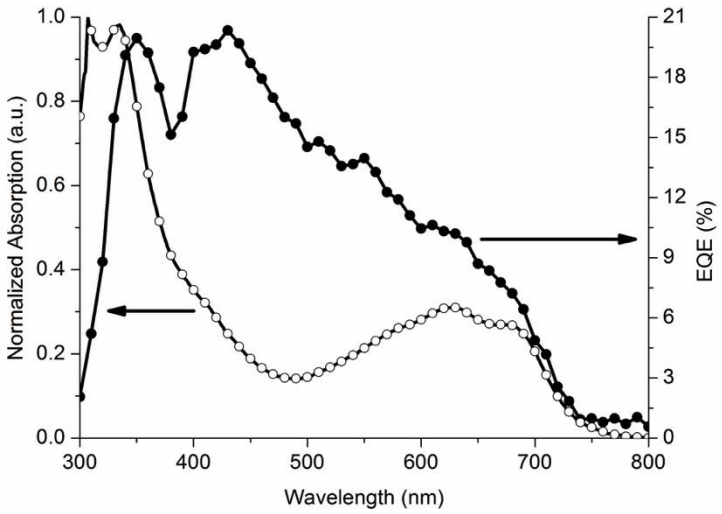

Figure 3.12 External quantum efficiency (EQE, right axis) and normalized absorption spectrum (left axis) of the best performing ternary devices employing **SFBTD**/P3DTV/$PC_{61}BM$ (1.5/2.5/8.5, wt./wt./wt.).

From binary blends to ternary blends, several trends are clearly observed. The V_{OC} values of ternary devices decrease with increasing P3DTV contents, which are all much closer to the side of P3DTV. For instance, in devices B (Table 3.4), addition of only 5 wt.% P3DTV (relative to **SFBTD**) reduces the V_{OC} from 0.88 V in device A to 0.57 V. Unlike previous ternary examples showing close to linear relationships between V_{OC} and composition changes,[20-21] we find that the relationship in our ternary blends is far from linearity after plotting the V_{OC} values against P3DTV contents in the donor blends (Figure 3.11). This result is consistent with our recent report for **SO**/P3DTV/PCBM ternary blends, which implies that in this ternary devices, P3DTV serves as the major hole conducting material regardless of its contents, likely due to the high lying HOMO level, high crystallinity and long-chain structures of the polymer.[1] The best performance is observed in ternary device E that displays a *PCE* of 1.21%, which is about 15% and 150% higher than those of binary devices employing **SFBTD** and P3DTV alone,

respectively. To better understand the working mechanism of ternary blend and current contributions from each of blend components, EQE experiments are performed on optimized ternary device E, as shown in Figure 3.12. Compared with binary device employing **SFBTD**/$PC_{61}BM$, ternary device exhibits higher efficiency between 600 nm and 750 nm, which should be contributed by P3DTV. Despite a low V_{OC} value at ca. 0.49 V, the improvement comes from the significantly improved J_{SC} and *FF* values. This indicates cooperative effects on photocurrent generation by mixing **SFBTD** and P3DTV, which enhance charge extraction from both of these materials. However, this cooperative effect becomes less pronounced as **SFBTD** contents increases.

Table 3.5 Ternary Device Performance Data Employing **PFDTV** and **PBrDTV** as the Second Donor Material.[a]

SFBTD/PFDTV/$PC_{61}BM$[b]	V_{OC} (V)	J_{SC} (mA/cm^2)	*FF* (%)	*PCE* (%)
H. 2.5 / 2.5 / 12.5	0.69 ± 0.00 (0.69)	2.20 ± 0.12 (2.37)	39 ± 1.54 (41)	0.59 ± 0.03 (0.63)
I. 1.5 / 2.5 / 8.5	0.66 ± 0.01 (0.66)	2.06 ± 0.21 (2.41)	42 ± 0.78 (43)	0.56 ± 0.06 (0.66)
J. 0.0 / 2.5 / 2.5 [c]	0.66 ± 0.01 (0.68)	0.98 ± 0.05 (1.05)	49 ± 1.53 (50)	0.32 ± 0.01 (0.33)
SFBTD/PBrDTV/$PC_{61}BM$[b]				
K. 2.5 / 0.125 / 10.0	0.83 ± 0.02 (0.86)	3.37 ± 0.21 (3.78)	31 ± 0.37 (32)	0.87 ± 0.05 (0.97)
L. 2.5 / 2.5 / 12.5	0.81 ± 0.00 (0.81)	2.65 ± 0.26 (3.01)	41 ± 0.74 (42)	0.88 ± 0.09 (1.01)
M. 1.5 / 2.5 / 8.5	0.77 ± 0.01 (0.78)	2.99 ± 0.19 (3.19)	44 ± 1.96 (46)	1.01 ± 0.07 (1.14)
N. 0.0 / 2.5 / 2.5[c]	0.77 ± 0.01 (0.77)	1.91 ± 0.12 (2.12)	45 ± 1.14 (46)	0.65 ± 0.04 (0.72)

[a] All devices are thermally annealed at 80 °C for 15 min; results are reported as averages of five individual cells; the highest values are given in parentheses. [b] All ratios by weight. [c] As-cast devices.

It is clear that in ternary blends with P3DTV, the low V_{OC} value, limiting the overall performance enhancement, is caused by the high lying HOMO level of P3DTV. We thus started investigating other conjugated polymers with lower lying HOMO levels, which may lead to higher V_{OC} values in our ternary blends with **SFBTD**. Therefore, two in-house made PTV derivatives are considered: PFDTV (M_n = 17.8 kDa, *PDI* = 2.0) and PBrDTV (M_n = 14.0 kDa, *PDI* = 2.2), as shown in Scheme 3.3.[22] They have similar optical bandgaps, but lower HOMO levels than that of P3DTV, which are at ca. −5.2 eV and −5.3 eV (from CV measurement), respectively. Table 3 summarizes detailed ternary device parameters involving PFDTV and PBrDTV at different weight ratios. Due to the HOMO levels of both PTV polymers that are close to that of **SFBTD,** higher V_{OC} values are achieved, which do not experience as drastic changes as that of the ternary devices employing P3DTV (Figure 3.11). *FF*s of these ternary devices are generally slight higher than those of binary devices using **SFBTD** alone, but the overall device performances are significantly limited by low J_{SC} values. It is likely that both PFDTV and PBrDTV do not act as the major hole conductor in the ternary blends due to their HOMO levels matching that of **SFBTD**, leading to unimproved charge extraction efficiencies. Thus, a judiciously experimented balance between energy level alignments, charge mobility and phase separation is critical in ternary blend OSCs involving both small molecules and polymers, which is currently under more thorough investigations.

3.5 Conclusions

We have prepared a molecular tetrapod **SFBTD** containing a tetraphenylsilance core and four fluorinated benzothiadiazole functionalized arms. The molecule has a medium bandgap and a deep lying HOMO energy level. DSC studies showed that

SFBTD has low degree of crystallinity and slow crystallization kinetics, owning to its tetrahedral geometry. Solution-processed BHJ OSCs employing **SFBTD**/$PC_{61}BM$ without any additives and interfacial engineering exhibit *PCE* of 1.05 %, which is limited by the low hole mobility and unfavorable blend morphologies. The device performance of **SFBTD**/$PC_{61}BM$ binary blends could be slightly improved by adding low bandgap PTV derivatives that can improve hole transportation in the ternary blends and result in a slight increase in device efficiencies. Our findings can give useful insights on the structure-property relationships of such molecular tetrapods and their applications in multi-component OSCs. Although we have shown high device stability using these molecular tetrapods, it is critical to increase the crystallization kinetics of the tetrapods and fully understand how they interact with fullerene acceptors within the blend films to order to induce proper phase separation in binary systems. On the other hand, our ternary blend studies has shown that a suitable third component with appropriate energy alignment and crystallinity can generate cooperative effects leading to devices that out-perform those employing each of the binary components alone. We are currently investigating these aspects in more detail in order to further understand the structure-property-function relationships in this class of conjugated molecular tetrapods.

3.6 Experimental Section

3.6.1 Materials and General Methods

All reagents and solvents were used as received from Sigma-Aldrich or Alfa Aesar unless otherwise noted. THF was distilled from Na/benzophenone prior to use. 4,7-dibromo-5-fluorobenzo[c][1,2,5]thiadiazole(**1**),[23] 2-(2-hexyldecyl)thiophene(**3**),[24] (5-(2-hexyldecyl)thiophen-2-yl)trimethylstannane (**4**),[24] trimethyl(phenyl)stannane(**11**),[25]

were prepared according to literature procedures. 300.13 MHz ^{1}H, 75.48 MHz ^{13}C and 282.37 MHz ^{19}F NMR spectra were recorded on a Bruker Avance III Solution 300 spectrometer. ^{1}H spectra were referenced internally to tetramethylsilane and ^{13}C spectra were referenced internally to chloroform. ^{19}F were referenced externally by using C_6F_6 (δ = −164.9 ppm). Time-of-flight mass spectrometry (TOF MS) was performed on a Waters/Micromass LCT Premier system operating under atmospheric pressure photoionization ($APPI^+$) mode. Elemental analysis was performed by ALS Environmental Laboratory in Tucson, Arizona. Samples were analyzed by combustion method through thermal conductivity and infrared detection. Ultraviolet-visible (UV-vis) absorption spectra were recorded on a Shimadzu UV-2401 PC spectrometer over a wavelength range of 240-900 nm. Fluorescence emission spectra were obtained using a Varian Cary Eclipse fluorimeter. Cyclic voltammetry was performed at 25 °C on a CH Instrument CHI604xD electrochemical analyzer using a glassy carbon working electrode, a platinum wire counter electrode, and a Ag/AgCl reference electrode calibrated using ferrocene redox couple (4.8 eV below vacuum). Tetrabutylammonium hexafluorophosphate (Bu_4NPF_6, 0.1 M) was used as the supporting electrolytes for the measurement. CV in solution was performed by dissolving samples in dichloromethane (1 mM) and adding into Bu_4NPF_6 (0.1 M) in dichloromethane during measurement. CV in thin film was done by dissolving samples in dichloromethane (1 mM) and drop-casting on the top of glassy carbon electrode, while Bu_4NPF_6 was dissolved in acetonitrile (0.1 M). Differential scanning calorimetry (DSC) measurements were performed on a Mettler Toledo DSC STAR^e system with ca. 10 mg sample was loaded into aluminum pan, and measurement was performed at scan rates of 10 °C / min and 1 °C / min under nitrogen.

The results are reported from the second heating curves. X-ray diffraction data was collected using a Rigaku SmartLab diffractometer in Bragg-Brentano mode employing Cu K-alpha radiation and a D/tex 1-dimensional detector. A nickel filter was used to remove the Cu K-beta radiation component. Data was collected over the two–theta range 2 to 40 degrees using a 0.02 degree step size at a scan rate of 6.2 degree/minute. Samples were prepared by dissolving **SFBTD** and **MFBTD** in chlorobenzene (10 mg/mL), respectively. The chlorobenzene solutions were drop-cast into glass slides and left in fume hood to evaporate solvent until they were dry for measurement. Optical Micrographs were taken on a Carl Zesis Axio Imager 2 microscope at a 400X magnification. Thin film samples were prepared by spin-coating method on ITO slides or directly used from OPV devices.

3.6.2 Quantum Efficiency

Quinine bisulfate in 0.1 M H_2SO_4 (quantum yield (Q) = 0.54 for excitation at 339 nm) was used as standard. **SFBTD** and **MFBTD** was dissolved in chlorobenzene to form very diluted solution. UV-vis absortion spectra of chlorobenzene solutions of **SFBTD** and **MFBTD** were measured, respectively. All extinctions should be below 0.05 to avoid inner filter effects. Refractive index of 0.1 M H_2SO_4 and chlorobenzene are 1.33 and 1.52, respectively. Use the following equation to calculate the quantum efficiency:

$$Q = Q_R \frac{I}{I_R} \frac{E_R}{E} \frac{n^2}{n_R^2}$$

Therefore, Q is quantum efficiency; I is integrated fluorescence intensity; E is extinction; n is refractive index; The index R indicates the standard.

3.6.3 Thin Film Preparation for UV-vis Measurement, Optics Images and Mobility Measurement

Neat films of **SFBTD** and **MFBTD** were prepared from chloroform solution (10 mg/mL) by spin-coating method on ITO surface. Though **SFBTD** and **MFBTD** have excellent solubility in chloroform, **MFBTD** solution cannot well wet ITO surface. Thus, neat **MFBTD** film was prepared by spin-coating at a slow speed such as 300 rpm for 30 s, while neat **SFBTD** film was spin-coated at 500 rpm for 30 s. The blend films including binary and ternary blends were all prepared from chloroform solution (10 mg/mL) and spin-coated at 500 rpm for 30 s.

3.6.4 Solar Cell Fabrication and Testing

A conventional structure of ITO/MoO_3 (10 nm)/active layer/Al (100 nm) was adopted for the solar cells studied. Devices were fabricated according to the following procedures. **SFBTD,** PCBM (American Dye Source, Inc.) and PTV derivatives (ternary blend) at predetermined weight ratios were dissolved in chloroform (CF) and stirred at room temperature for 3 h in a nitrogen glovebox (Innovative Technology, model PL-He-2GB, O_2 < 0.1 ppm, H_2O < 0.1 ppm). ITO-coated glass substrates (China Shenzhen Southern Glass Display. Ltd, 8 Ω/□) were cleaned by ultrasonication sequentially in detergent, DI water, acetone and isopropyl alcohol, each for 15 min. These ITO-coated glass substrates were further treated by UV-ozone (PSD Series, Novascan) for 45 min before transferred into a nitrogen glovebox (Innovative Technology, model PL-He-4GB-1800, O_2 < 0.1 ppm, H_2O < 0.1 ppm) for MoO_3 deposition. MoO_3 (10 nm) was deposited using an Angstrom Engineering Åmod deposition system at a base vacuum level < 7×10^{-8} Torr. The blend solution (10 mg/mL for both binary and ternary device) was first filtered through a 0.45 μm PTFE filter and spin-coated on top of the MoO_3 layer at preset speeds (1000 rpm to 2000 rpm) for 30s. Al (100 nm) was finally thermally evaporated

through patterned shadow masks as anodes. Current-voltage (I-V) characteristics were measured by a Keithley 2400 source-measuring unit under simulated AM1.5G irradiation (100 mW/cm^2) generated by a Xe arc-lamp based Newport 67005 150-W solar simulator equipped with an AM1.5G filter. The light intensity was calibrated by using a Newport thermopile detector (model 818P-010-12) equipped with a Newport 1916-C Optical Power Meter. External quantum efficiency (EQE) values were measured by using a commercial solar cell quantum efficiency measurement system (Model QEXL, PV Measurements, Inc., Boulder, CO). The EQE system was calibrated with a Si photodiode certified by the National Renewable Energy Laboratory (NREL). Samples are directly used from OPV devices.

3.6.5 Mobility Measurement

Hole-only devices were fabricated using the architectures: ITO/MoO_3/neat film/MoO_3/Al and ITO/MoO_3/blend film/MoO_3/Al. Mobilities were extracted by fitting the current density–voltage curves using the Mott–Gurney relationship (Space charge limited current, SCLC), where the SCLC is described by $J = 9\varepsilon_0\varepsilon_r\mu V^2/8L^3$, where J is the current density, L is the film thickness of active layer, μ is the hole or electron mobility, ε_r is the relative dielectric constant of the transport medium, ε_0 is the permittivity of free space (8.85×10^{-12} Fm^{-1}), V is the internal voltage in the device and $V = V_{appl} - V_r - V_{bi}$, where V_{appl} is the applied voltage to the device, V_r is the voltage drop due to contact resistance and series resistance across the electrodes, and V_{bi} is the built-in voltage due to the relative work function difference of the two electrodes. Thin film thickness was measured by using the KLA-Tencor D-100 Profilometer.

3.6.6 Synthetic Procedures

2. Compound **1** (0.624 g, 2.00 mmol) and tributyl(thiophen-2-yl)stannane (0.746 g, 2.00 mmol) was dissolved in anhydrous toluene in a pressure vessel containing a magnetic stir bar. $Pd(PPh_3)_4$ (69.3 mg, 3 mol%) were added to the pressure vessel in argon filled glovebox. The pressure vessel was sealed and taken out of the glove box. The reaction was carried out at 110 °C for 24 hours. After cooling the reaction mixture to room temperature, the resulted reaction mixture was firstly extracted with ether and followed by washing with DI H_2O and brine solution. After the organic layer was dried with anhydrous Na_2SO_4, the solvent was removed by rotor-vapor. The crude product was further purified by silica gel chromatography with hexane/chloroform to yield yellow solid. (0.501 g, 79.4%) ^{1}H NMR (300.13 MHz, $CDCl_3$), δ (ppm) = 7.22 (*Th-H*, dd, 1H, J^3_{HH} = 5.1 Hz), 7.53 (*Th-H*, d, 1H, J^3_{HH} = 5.1 Hz), 7.70 (*Ph-H*, d, 1H, J^3_{HH} = 9.9 Hz), 8.11 (*Th-H*, d, 1H, J^3_{HH} = 3.6 Hz) ^{13}C NMR (75.48 MHz, $CDCl_3$): 95.9, 96.3, 115.8, 115.9, 116.2, 116.3, 127.3, 127.4, 128.2, 128.3, 128.9, 137.1, 148.8, 154.0, 154.1, 158.9, 162.2. ^{19}F NMR (282.37 MHz, $CDCl_3$), δ (ppm) = - 101.9.

5. Compound **2 (**0.63 g, 2.0 mmol) and compound **4** (1.42 g, 3.0 mmol) was dissolved in anhydrous DMF in a pressure vessel containing a magnetic stir bar. $Pd(PPh_3)_4$ (115.6 mg, 5mol%) were added to the pressure vessel in argon filled glovebox. The pressure vessel was sealed and taken out of the glove box. The reaction was carried out at 150 °C for 24 hours. After cooling the reaction mixture to room temperature, the resulted reaction mixture was firstly extracted with ether and followed by washing with 1M HCl solution, DI H_2O and brine solution. After the organic layer was dried with anhydrous Na_2SO_4, the solvent was removed by rotor-vapor. The crude product was further purified by silica gel chromatography with hexane/chloroform to get orange solid. (0.96 g, 77.1%) ^{1}H NMR

(300.13 MHz, $CDCl_3$), δ (ppm) = 0.87 – 0.88 (-*CH_3*, m, 6H), 1.26 – 1.32 (-*CH_2*, m, 24H), 1.73 (-*CH_2*, m, 1H), 2.83 (-*CH_2*, d, 2H, J^3_{HH} = 6.6 Hz), 6.87 (*Th-H*, d, 1H, J^3_{HH} = 3.6 Hz), 7.17 (*Th-H*, dd, 1H, J^3_{HH} = 5.1 Hz), 7.45 (*Th-H*, d, 1H, J^3_{HH} = 5.1 Hz), 7.69 (*Ph-H*, d, 1H, J^3_{HH} = 12.9 Hz), 8.06 – 8.08 (*Th-H*, m, 2H) ^{13}C NMR (75.48 MHz, $CDCl_3$): 14.1, 22.7, 26.6, 29.3, 29.6, 29.7, 30.0, 31.9, 33.3, 34.5, 40.0, 111.5, 111.7, 116.7, 117.2, 124.9, 125.0, 125.6, 127.5, 128.1, 130.1, 130.2, 138.0, 147.6, 147.7, 149.7, 153.2, 153.4, 156.7, 160.1. ^{19}F NMR (282.37 MHz, $CDCl_3$), δ (ppm) = - 107.4.

6. Weight 0.96 g (1.54 mmol) compound **5** and dissolve in THF, and then 0.30 g (1.69 mmol) NBS powder was weighted and added into flask under ice bath. The reaction was stirring at room temperature for overnight. The resulted reaction mixture was washed with saturated Na_2SO_3, 1 M HCl solution, DI H_2O and brine solution. After the organic layer was dried with anhydrous Na_2SO_4, the solvent was removed by rotor-vapor. The crude product was dried in vacuum without further purification and used for next step. (1.08 g, 100%) ^{1}H NMR (300.13 MHz, $CDCl_3$), δ (ppm) = 0.87 – 0.88 (-*CH_3*, m, 6H), 1.27 – 1.33 (-*CH_2*, m, 24H), 1.72 (-*CH_2*, m, 1H), 2.82 (-*CH_2*, d, 2H, J^3_{HH} = 6.6 Hz), 6.87 (*Th-H*, 1H), 7.11 (*Th-H*, d, 1H, J^3_{HH} = 3.9 Hz), 7.59 (*Ph-H*, d, 1H, J^3_{HH} = 12.9 Hz), 7.71 (*Th-H*, d, 1H, J^3_{HH} = 3.9 Hz), 8.07 (*Th-H*, d, 1H, J^3_{HH} = 3.3 Hz) ^{13}C NMR (75.48 MHz, $CDCl_3$): 14.1, 22.7, 26.6, 29.3, 29.6, 29.7, 30.0, 31.9, 33.2, 34.5, 40.0, 111.8, 111.9, 115.5, 115.9, 116.4, 123.6, 123.7, 125.6, 127.4, 129.9, 130.0, 130.3, 130.4, 130.5, 139.3, 147.8, 147.9, 149.2, 152.9, 153.1, 156.5, 159.8. ^{19}F NMR (282.37 MHz, $CDCl_3$), δ (ppm) = - 107.4.

7. Compound **6** (1.08 g, 1.54 mmol) and tributyl(thiophen-2-yl)stannane (0.69 g, 1.85 mmol) was dissolved in anhydrous DMF in a pressure vessel containing a magnetic stir

bar. $Pd(PPh_3)_4$ (89.0 mg 5mol%) were added to the pressure vessel in argon filled glovebox. The pressure vessel was sealed and taken out of the glove box. The reaction was carried out at 90 °C for 24 hours. After cooling the reaction mixture to room temperature, the resulted reaction mixture was firstly extracted with ether and followed by washing with 1M HCl solution, DI H_2O and brine solution. After the organic layer was dried with anhydrous Na_2SO_4, the solvent was removed by rotor-vapor. The crude product was further purified by silica gel chromatography with hexane/chloroform to yield orange-red solid. (1.07 g, 98.2%) ^{1}H NMR (300.13 MHz, $CDCl_3$), δ (ppm) = 0.87 – 0.88 (-*CH*$_3$, m, 6H), 1.27 – 1.33 (-*CH*$_2$, m, 24H), 1.74 (-*CH*$_2$, m, 1H), 2.84 (-*CH*$_2$, d, 2H, J^3_{HH} = 6.6 Hz), 6.90 (*Th-H*, 1H), 7.07 (*Th-H*, dd, 1H, J^3_{HH} = 5.1 Hz), 7.26 – 7.31 (*Th-H*, m, 3H), 7.74 (*Ph-H*, d, 1H, J^3_{HH} = 12.9 Hz), 8.03 (*Th-H*, d, 1H, J^3_{HH} = 3.9 Hz), 8.11 (*Th-H*, d, 1H, J^3_{HH} = 3.6 Hz) ^{13}C NMR (75.48 MHz, $CDCl_3$): 14.1, 22.7, 26.6, 29.3, 29.6, 29.7, 30.0, 31.9, 33.3, 34.5, 40.0, 111.3, 111.5, 115.9, 116.3, 124.1, 124.3, 124.5, 124.9, 125.6, 127.9, 128.7, 130.1, 130.2, 130.3, 136.5, 136.6, 137.0, 139.5, 147.5, 147.6, 149.5, 153.1, 153.3, 156.7, 160.0. ^{19}F NMR (282.37 MHz, $CDCl_3$), δ (ppm) = - 107.6.

8. Weight (1.07 g, 1.52 mmol) compound **7** and dissolve in THF, and then (0.30 g, 1.67 mmol) NBS powder was weighted and added into flask under ice bath. The reaction was stirring at room temperature for overnight. The resulted reaction mixture was washed with saturated Na_2SO_3, 1 M HCl solution, DI H_2O and brine solution. After the organic layer was dried with anhydrous Na_2SO_4, the solvent was removed by rotor-vapor. The resulted crude product was further purified by silica gel chromatography with hexane/dichloromethane to yield dark red solid. (1.05 g, 88.2%) ^{1}H NMR (300.13 MHz, $CDCl_3$), δ (ppm) = 0.87 – 0.88 (-*CH*$_3$, m, 6H), 1.27 – 1.33 (-*CH*$_2$, m, 24H), 1.74 (-*CH*$_2$, m,

1H), 2.84 (-CH_2, d, 2H, J^3_{HH} = 6.6 Hz), 6.90 (*Th-H*, d, 1H, J^3_{HH} = 3.9 Hz), 7.01 (*Th-H*, d, 1H, J^3_{HH} = 3.9 Hz), 7.04 (*Th-H*, d, 1H, J^3_{HH} = 3.9 Hz), 7.18 (*Th-H*, d, 1H, J^3_{HH} = 4.2 Hz), 7.72 (*Ph-H*, d, 1H, J^3_{HH} = 12.9 Hz), 7.98 (*Th-H*, d, 1H, J^3_{HH} = 3.9 Hz), 8.11 (*Th-H*, d, 1H, J^3_{HH} = 3.6 Hz) ^{13}C NMR (75.48 MHz, $CDCl_3$): 14.1, 22.7, 26.6, 29.3, 29.6, 29.7, 30.0, 31.9, 33.3, 34.5, 40.0, 111.7, 111.8, 116.2, 116.6, 124.2, 124.3, 124.5, 125.6, 128.6, 130.1, 130.2, 130.3, 130.4, 130.8, 137.0, 138.4, 138.5, 147.8, 147.9, 149.5, 153.2, 153.3, 156.7, 160.0. ^{19}F NMR (282.37 MHz, $CDCl_3$), δ (ppm) = - 107.5.

9. Weight 5.00 g (21.19 mmol) 1,4-dibromobenzene in a dry 100 ml Schlenk flask, and 50 ml anhydrous THF was transferred into Schlenk flask at -78 °C. 8.47 ml (21.19 mmol) 2.5 M nBuLi solution was injected slowly by syringe. Then, the reaction mixture was further stirring at -78 °C for 2 hours. 0.90 g (5.30 mmol) $SiCl_4$ was weighted and dissolved in 5 ml anhydrous THF in argon filled glovebox. $SiCl_4$ solution was then injected into reaction mixture via syringe at -78 °C. The reaction mixture was firstly kept stirring at -78 °C for 1 hour and then warmed up to room temperature for overnight. The resulted reaction mixture was extracted by ethyl ether and followed by washing with DI H_2O and saturated brine solution. After the organic layer was dried with anhydrous Na_2SO_4, the solvent was removed by rotor-vapor. The crude product was then purified by silica gel chromatography with hexane to yield white powder product. (2.84 g, 82.3%) ^{1}H NMR (300.13 MHz, $CDCl_3$), δ (ppm) = 7.33 (*Ph-H*, d, 8H, J^3_{HH} = 8.4 Hz), 7.53 (*Ph-H*, d, 8H, J^3_{HH} = 8.1 Hz) ^{13}C NMR (75.48 MHz, $CDCl_3$): 125.4, 131.4, 131.5, 137.6.

10. Compound **9** (0.58 g, 0.89 mmol), bis (pinacolato) diboron (1.13 g, 4.45 mmol) and potassium acetate (0.52 g, 5.34 mmol) were dissolved in 30 mL anhydrous DMF in a pressure vessel containing a magnetic stir bar inside an argon filled glovebox. $Pd(OAc)_2$

(12 mg, 6.0 mol%) was then added to the reaction mixture. The pressure vessel was sealed and taken out of the glovebox. The reaction was carried out at 80 °C for 24 hours and then cooled to room temperature. After standard aqueous workup, compound 10 was further purified by silica gel chromatography with hexane/ethyl acetate (0.52 g, 69.3%). ^{1}H NMR (300.13 MHz, $CDCl_3$): δ (ppm) = 1.35 (-*CH*$_3$, s, 48H), 7.55 (*Ph-H*, d, 8H, J^3_{HH} = 7.5 Hz), 7.79 (*Ph-H*, d, 8H, J^3_{HH} = 7.5 Hz). ^{13}C NMR (75.48 MHz, $CDCl_3$): δ (ppm) = 24.8, 83.8, 133.9, 135.6, 137.2.

MFBTD Compound **11** (36 mg, 0.15 mmol) and compound **8** (97.9 mg, 0.14 mmol) were dissolved in 5 mL anhydrous DMF in a pressure vessel containing a magnetic stir bar inside an argon filled glovebox. $Pd(PPh_3)_4$ (8.1 mg, 5.0 mol%), CuI (2.6 mg, 10.0 mmol%) and CsF (22.7 mg, 0.15 mmol) were then added to the reaction mixture. The pressure vessel was sealed and taken out of the glovebox. The reaction was carried out at 80 °C for 24 hours and then cooled to room temperature. After standard aqueous workup, crude **MFBTD** was further purified by silica gel chromatography with hexane/dichloromethane to yield pure compound as dark red solid (62 mg, 63.6%). ^{1}H NMR (300.13 MHz, $CDCl_3$), δ (ppm) = 0.87 – 0.88 (-*CH*$_3$, m, 6H), 1.27 – 1.33 (-*CH*$_2$, m, 24H), 1.74 (-*CH*$_2$, m, 1H), 2.85 (-*CH*$_2$, d, 2H, J^3_{HH} = 6.6 Hz), 6.91 (*Th-H*, 1H), 7.28 – 7.33 (m, 4H), 7.38 – 7.43 (*Ph-H*, m, 2H), 7.62 – 7.64 (*Ph-H*, m, 2H), 7.75 (*Ph-H*, d, 1H, J^3_{HH} = 13.2 Hz), 8.05 (*Th-H*, d, 1H, J^3_{HH} = 3.9 Hz), 8.12 (*Th-H*, d, 1H, J^3_{HH} = 3.6 Hz) ^{13}C NMR (75.48 MHz, $CDCl_3$): 14.1, 22.7, 26.6, 29.3, 29.7, 30.0, 31.9, 33.3, 34.5, 40.0, 111.3, 111.5, 115.9, 116.3, 123.8, 124.2, 124.3, 124.5, 125.0, 125.5, 127.7, 128.8, 128.9, 130.1, 130.2, 133.8, 136.2, 136.5, 139.5, 143.7, 147.6, 147.7, 149.5, 153.2, 153.3, 156.7, 160.1. ^{19}F NMR (282.37 MHz, $CDCl_3$), δ (ppm) = - 107.5.

SFBTD Compound **10** (105 mg, 0.125 mmol) and compound **8** (439.9 mg, 0.625 mmol) were dissolved in 10 mL anhydrous DMF and 10 ml toluene in a pressure vessel containing a magnetic stir bar inside an argon filled glovebox. $Pd(PPh_3)_4$ (14.4 mg, 10.0 mol%) and K_2CO_3 (103.6 mg, 0.75 mmol) was then added to the reaction mixture. The pressure vessel was sealed and taken out of the glovebox. The reaction was carried out at 120 °C for 48 hours and then cooled to room temperature. After standard aqueous workup, crude **SFBTD** was further purified by silica gel chromatography with hexane/chloroform to yield pure compound as dark red solid (185 mg, 52.3%).^{1}H NMR (300.13 MHz, $CDCl_3$), δ (ppm) = 0.87 (-*CH*$_3$, m, 24H), 1.26 (-*CH*$_2$, m, 96H), 1.68 (-*CH*$_2$, m, 4H), 2.73 (-*CH*$_2$, 8H), 6.73 (*Th-H*, 4H), 7.00 (*Th-H*, 4H), 7.11 (*Th-H*, 4H), 7.21 (*Th-H*, 4H), 7.51 (m, 20H), 7.75 (*Th-H*, 4H), 7.94 (*Th-H*, 4H) ^{13}C NMR (75.48 MHz, $CDCl_3$): 14.1, 21.5, 22.7, 26.5, 27.7, 29.4, 29.7, 30.0, 31.9, 33.2, 34.3, 40.0, 45.4, 111.0, 111.2, 115.4, 115.9, 123.8, 123.9, 124.2, 124.7, 125.3, 128.3, 129.7, 130.2, 130.3, 132.9, 134.8, 136.4, 136.7, 137.0, 138.9, 142.8, 147.1, 147.2, 149.2, 152.8, 153.0, 156.5, 159.9. ^{19}F NMR (282.37 MHz, $CDCl_3$), δ (ppm) = - 107.0. TOF MS ($APPI^+$): Calcd. for $SiC_{160}H_{176}F_4N_8S_{16}$: 2824.9255 [$M^+$]; found: 2825.7766 [$M^+$]. Elemental analysis: anal. calcd (%) for $SiC_{160}H_{176}F_4N_8S_{16}$: Si, 0.99; C, 67.95; H, 6.27; F, 2.69; N, 3.96; S, 18.14. Found: C, 67.95; H, 6.54; N, 3.75.

3.7 References

(1) Yang, J. Z.; He, W. H.; Denman, K.; Jiang, Y. B.; Qin, Y. *J. Mater. Chem. A* **2015**, 3, 2108.

(2) Carsten, B.; Szarko, J. M.; Son, H. J.; Wang, W.; Lu, L. Y.; He, F.; Rolczynski, B. S.; Lou, S. J.; Chen, L. X.; Yu, L. P. *J. Am. Chem. Soc.* **2011**, 133, 20468.

(3) Rolczynski, B. S.; Szarko, J. M.; Son, H. J.; Liang, Y.; Yu, L.; Chen, L. X. *J. Am. Chem. Soc.* **2012**, 134, 4142.

(4) Zang, H. D.; Liang, Y. Y.; Yu, L. P.; Hu, B. *Adv. Energy Mater.* **2011**, 1, 923.

(5) Liu, P.; Zhang, K.; Liu, F.; Jin, Y. C.; Liu, S. J.; Russell, T. P.; Yip, H. L.; Huang, F.; Cao, Y. *Chem. Mater.* **2014**, 26, 3009.

(6) Yu, G.; Gao, J.; Hummelen, J. C.; Wudl, F.; Heeger, A. J. *Science* **1995**, 270, 1789.

(7) Frisch. M. J.; Trucks, G. W. S., H. B.; et. al. *Gaussian 09*, Revision B.01; Gaussian, Inc: Wallingford, CT, **2010**.

(8) Dreuw, A.; Head-Gordon, M. *J. Am. Chem. Soc.* **2004**, 126, 4007.

(9) Roquet, S.; de Bettignies, R.; Leriche, P.; Cravino, A.; Roncali, J. *J. Mater. Chem.* **2006**, 16, 3040.

(10) Spano, F. C. *Acc. Chem. Res.* **2010**, 43, 429.

(11) Lai, L. F.; Love, J. A.; Sharenko, A.; Coughlin, J. E.; Gupta, V.; Tretiak, S.; Nguyen, T. Q.; Wong, W. Y.; Bazan, G. C. *J. Am. Chem. Soc.* **2014**, 136, 5591.

(12) Malliaras, G. G.; Salem, J. R.; Brock, P. J.; Scott, C. *Phys. Rev. B* **1998**, 58, 13411.

(13) Zhang, C.; Matos, T.; Li, R.; Sun, S. S.; Lewis, J. E.; Zhang, J. A.; Jiang, X. M. *Polym. Chem.* **2010**, 1, 663.

(14) Qin, Y.; Hillmyer, M. A. *Macromolecules* **2009**, 42, 6429.

(15) Kim, J. Y.; Qin, Y.; Stevens, D. A.; Ugurlu, O.; Kalihari, V.; Hillmyer, M. A.; Frisbie, C. D. *J. Phys. Chem. C* **2009**, 113, 10790.

(16) Jestin, I.; Frere, P.; Blanchard, P.; Roncali, J. *Angew. Chem., Int. Ed.* **1998**, 37, 942.

(17) Yang, G. S.; Hu, K. D.; Qin, Y. *J. Polym. Sci., Part A: Polym. Chem.* **2014**, 52, 591.

(18) Olejnik, E.; Pandit, B.; Basel, T.; Lafalce, E.; Sheng, C. X.; Zhang, C.; Jiang, X.; Vardeny, Z. V. *Phys. Rev. B* **2012**, 86, 235201.

(19) Musser, A. J.; Al-Hashimi, M.; Maiuri, M.; Brida, D.; Heeney, M.; Cerullo, G.; Friend, R. H.; Clark, J. *J. Am. Chem. Soc.* **2013**, 135, 12747.

(20) Khlyabich, P. P.; Burkhart, B.; Thompson, B. C. *J. Am. Chem. Soc.* **2011**, 133, 14534.

(21) Khlyabich, P. P.; Burkhart, B.; Rudenko, A. E.; Thompson, B. C. *Polymer* **2013**, 54, 5267.

(22) Zhang, Z.; Qin, Y. *Macromolecules* **2016**, 49, 3318.

(23) Albrecht, S.; Janietz, S.; Schindler, W.; Frisch, J.; Kurpiers, J.; Kniepert, J.; Inal, S.; Pingel, P.; Fostiropoulos, K.; Koch, N.; Neher, D. *J. Am. Chem. Soc.* **2012**, 134, 14932.

(24) Shi, X. L.; Chang, J. J.; Chi, C. Y.. *Chem. Commun.* **2013**, 49, 7135.

(25) Tsai, C. H.; Chirdon, D. N.; Maurer, A. B.; Bernhard, S.; Noonan, K. J. T. *Org. Lett.* **2013**, 15, 5230.

Chapter 4

Synthesis of Fullerene-Borate Ionic Complexes

(This chapter is based on a manuscript in preparation)

4.1 Introduction

Fullerenes have been widely used as an efficient electron acceptor, owing to their small reorganization energy, which results from the π-electron system being highly delocalized over the three-dimensional curved surface together with the rigid and confined structure of the aromatic π-sphere.[1–4] However, fullerenes are very difficult in modifying their properties through chemical reactions, due to their poor solubility in common organic solvents and relatively low yield of modification reactions such as Prato synthesis. In order to address this problem, a large variety of covalent and noncovalent donor-acceptor (D-A) systems using fullerenes as electron acceptor units have been designed, and the photophysical properties of these D-A materials have been investigated both in solution and in solid state as well as their use as active components in photovoltaic devices.[5-31] Among many D-A systems containing fullerenes as acceptor unit, long-lived charge separated (CS) states were observed,[32-37] which were attained by photo-induced charge separation processes to convert solar energy to chemical energy.[38-39] Hodgkiss, Friend and their coworkers also reported that ionic charges have the potential to stabilize CS states in conjugated polymers by establishing local Coulomb fields that perturb the HOMO and LUMO orbital energies. For example, a cation will lower the energy levels of HOMO and LUMO orbitals of neighboring chains, thus attracting electrons and repelling holes, while an anion will have the reverse effect.[40] Thus, introducing ionic interaction into a D-A system containing fullerenes as acceptor

unit to form an ionic fullerene complex can realize effective photo-induced charge transfer and long-lived charge separated states. On the other hand, some ionic fullerene complexes also show very interesting magnetic and conducting properties.[41-42]

At present, effective methods for selective fullerene reduction and preparation of ionic ($Cation^+$) ($C_{60}^{\bullet -}$) complexes with organic and metal-containing cations have been developed.[43] For example, metalloporphyrins and metallophthalocyanines can be inserted to form ionic fullerene complexes. However, it's rare to see an ionic fullerene system constructed by cationic fullerene with anionic chromophore. Recently, Fukuzumi and his coworkers reported a supramolecular donor-acceptor system composed of anionic sulfonated porphyrins as electron donors and a cationic lithium ion encapsulated fullerene ($Li^+@C_{60}$) as an electron acceptor. A strong supramolecular binding and a long CS lifetime were attained in PhCN at 298 K. However, $Li^+@C_{60}$ is usually synthesized by plasma method, resulting in a high cost of this material.[44] In searching of cationic fullerene, we find fulleropyrrolidinium ions are a type of promising ionic fullerene, possessing good solubility in polar solvents,[45] strong electron-accepting ability,[46] and self-assembling properties.[47-48] Jen and his coworker developed a new solution processible fulleropyrrolidinium ion and applied it as a solution processible electron transporting layer (ETL) for polymer solar cells. Devices based on this ETL/Ag hybrid cathode exhibited superior performance and device stability to those using Ca/Al or Al as cathode. Moreover, the fulleropyrrolidinium ion thin films exhibit high conductivity when they were investigated using field-effect transistor (FET) technique showing linear I_D–V_D characteristic that is independent of the gate-field.[49-50] While in the search of anionic chromophore, we notice that four-coordinated boron-cored unit such as borate is

an ideal building unit, since the boron atom enables enriching the functions of organic materials, including reagents, catalysts and luminescent materials.[51-53] Tetraphenylborate and its derivatives are some of the most frequently used borates, while fluorine or CF_3 group are introduced into tetraphenylborate can help to increase the hydrophobicity and also largely improving their stability against protic acids and oxidants.[54-57]

Herein, we aim to build a D-A complex system constructed by cationic fulleropyrrolidinium and anionic tetraphenylborate. To prove the concept, we firstly synthesized a model compound **FP-Ph**, the structure of which was confirmed by NMR and single crystal XRD. The model compound **FP-Ph** shows excellent solubility in organic solvent such as acetone, acetonitrile, DMSO and chlorobenzene. Thus, we induced anthracene to form a new complex **FP-Ant** through Sonogashira coupling reaction to extend the absorption of complex into the visible light range. We found efficient photo-induced charge transfer inside our complex through fluorescence quenching experiment. Besides, a series of fullerene-borate ionic complex were synthesized according to a similar synthetic route.

4.2 Synthesis and Characterization of Fullerene-Borate Ionic Complex FP-Ph

4.2.1 Synthesis of FP-Ph

In order to prove our concept, we first chose to build a model fullerene-borate ionic complex **FP-Ph**. Ionic fullerene **FPI** was synthesized according to literature.[58] Commercial available 1-bromo-2, 3, 5, 6-tetrafluorobenzene was applied to react with phenyl acetylene through standard Sonogashira coupling reaction. Then, the resulting coupling compound **2** was lithiated by n-BuLi and treated with 0.25 eq of 1 M BCl_3 solution in dry diethyl ether at -78 °C to yield a stable lithium tetrakis (tetrafluorophenyl)

borate. The solubility of lithium borate salt was further improved by ionic exchange with tetrabutylammonia bromide in methanol, where pure **TBA-Ph** precipitated from methanol. Thus, **TBA-Ph** and **FPI** in 1:1 ratio was mixed in DMSO, and then DI water was added to precipitate the final fullerene-borate ionic complex **FP-Ph**, which was further purified by washing with large amount of water to get rid of tetrabutyl ammonia iodide salt. The structure of **FP-Ph** was firstly confirmed by NMR such as ^{1}H, ^{11}B and ^{19}F, which agrees well with expected structure.

Scheme 4.1 Synthesis route of **FP-Ph**.

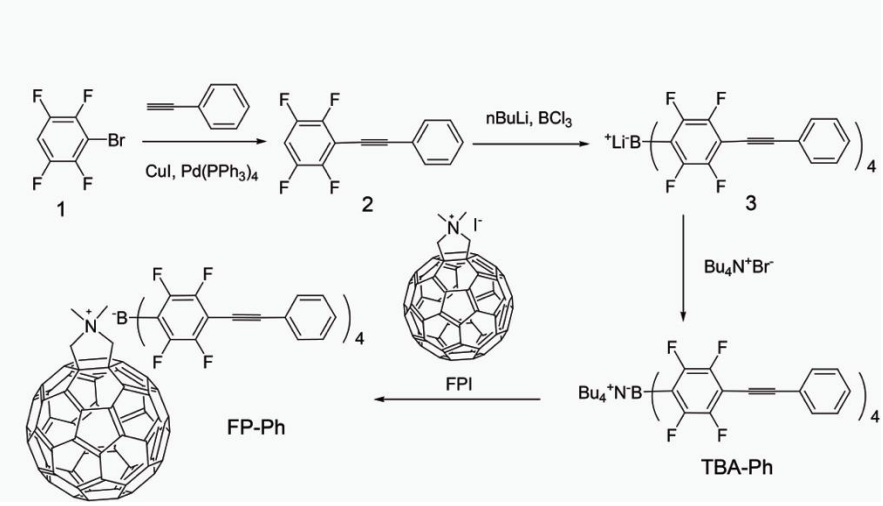

4.2.2 Growth of Single Crystal of FP-Ph

In order to further confirm the structure of **FP-Ph**, we tried to grow the single crystal of **FP-Ph** in different solvent systems. Eventually, a yellow-orange plate-like single crystal of **FP-Ph** was obtained by slowly evaporating the chlorobenzene solution of **FP-Ph** at room temperature in 2 days without any disturbing. **FP-Ph** crystal belongs to orthorhombic system, space group *pbca* with a = 19.0742 (5) Å, b = 25.8934 (6) Å, c = 34.8854 (10) Å, v = 17229.8 Å ^{3}, Dc = 1.562 g/cm^{3}, μ = 0.174 mm^{-1}.

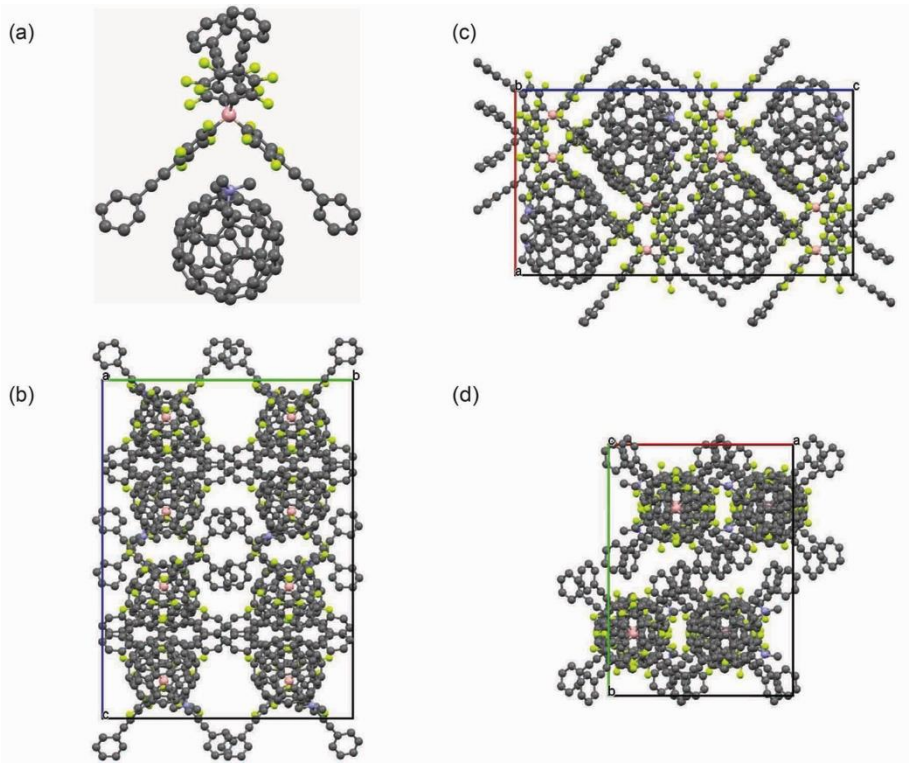

Figure 4.1 Solvent, hydrogen and disorder atoms are hidden; Grey balls are carbon, blue ball is nitrogen, yellow balls are fluorine and pink ball is boron. (a) Ball-stick single crystal structure of **FP-Ph**; (b) Crystal packing looking along down the a-axis; (c) Crystal packing looking along down the b-axis; (d) Crystal packing looking along down the c-axis.

4.2.3 UV-vis Absorption of FP-Ph and Its Precursors

As shown in Figure 4.2, the UV-vis absorption of **FP-Ph** in solution is basically the superposition of two precursors **FPI** and **TBA-Ph**. The maximum absorption of **FP-Ph** was found at 276 nm, while there are also two sharp peaks at 290 nm and 313 nm corresponding to two sharp peaks from **TBA-Ph**. The less intense absorption between 330 nm to 400 nm comes from the absorption from the fullerene side.

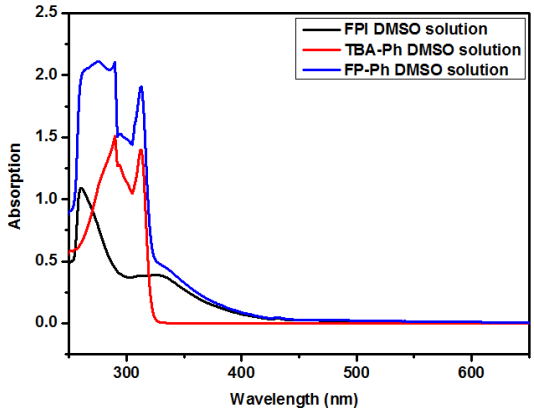

Figure 4.2 UV-vis absorption of **FP-Ph** and its precursors (10^{-5} M in DMSO).

4.2.4 Cyclic Voltammetry of FP-Ph

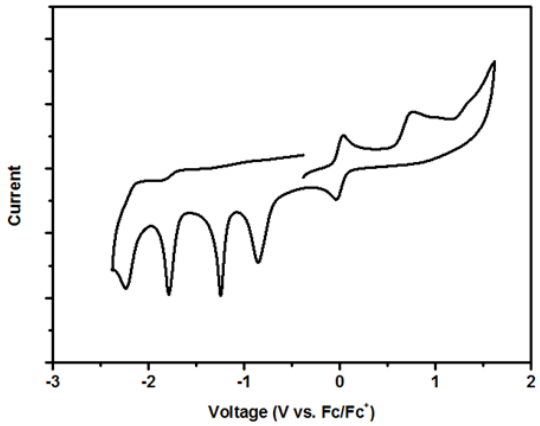

Figure 4.3 Cyclic voltammograms of **FP-Ph** in acetonitrile solutions (1 mM) containing Bu_4NPF_6 as the supporting electrolytes (0.1 M). The voltages are referenced externally to ferrocene (Fc) redox couple. Scan rate: 100 mV/s.

In order to quantify the frontier energy levels, cyclic voltammetry (CV) measurements were performed on **FP-Ph** in acetonitrile solutions (1 mM). A glassy carbon working electrode, a Ag/AgCl reference electrode and a Pt wire counter electrode were used. Tetrabutylammonium hexafluorophosphate (Bu_4NPF_6, 0.1 M) was used as the supporting electrolytes. The recorded CV curves were externally referenced to ferrocene/ferrocenium (Fc/Fc^+) redox couple (4.80 eV below vacuum). Therefore, the

HOMO and LUMO energy levels can be estimated using the empirical formula $E_{HOMO} = -(E_{ox}^{onset} + 4.80)$ eV and $E_{LUMO} = -(E_{red}^{onset} + 4.80)$ eV, respectively. As shown in Figure 4.3, the first oxidation peak and first reduction peak of **FP-Ph**, at onsets of ca. 0.59 V and −0.68 V, respectively, were observed. As a result, the HOMO and LUMO levels of **FP-Ph** were estimated to be –5.39 eV and −4.12 eV.

4.2.5 Brunauer-Emmett-Teller (BET) Surface Area Analysis

As seen in the single crystal of **FP-Ph**, ionic fullerenes were surrounded by ionic borates in an ordered matrix. We suspect that there possibly exist many pores between fullerenes and borates, which probably can give a large surface area. In order to prove our assumption, BET surface area analysis was performed on **FP-Ph** powder. Nitrogen sorption isotherms were obtained on a Gemini 2360 V5.00 at liquid nitrogen temperature (77 K). Prior to measurement, samples were outgassed for 20 h at 120 ℃ with nitrogen flow. BET specific surface areas were obtained from the adsorption branch from P/P_0 = 0.05-0.30. BET surface area of **FP-Ph** powder was calculated as 11.2 m^2/g, which indicated **FP-Ph** was nonporous.

4.3 Synthesis and Characterization of Ionic Complex FP-Ant

4.3.1 Synthesis of FP-Ant

As we learn in previous section, model fullerene-borate ionic complex **FP-Ph** doesn't have intense absorption in visible light range (300 nm to 700 nm). Therefore, we decide to extend the absorption of complex by replacing the end-capped phenyl group with anthracene, which is a small size and planar chromophore. According to the previous work reported by Mullen and his coworkers,[59] an ethynyl-functionalized of tetrakis (tetrafluorophenyl) borate (**TBA-A**) was synthesized in good yield as depicted in

Scheme 4.2. This compound can serve as a universal starting point, which is convenient to attach different chromophores through a standard Sonagashira coupling reaction in order to get different absorption ranges of ionic fullerene-borate complex. Thus, 9-bromoanthracene was attached to form **TBA-Ant**. A new ionic fullerene **FPTF** was synthesized as depicted in Scheme 4.2, and then used to mix with **TBA-Ant** in 1:1 ratio to yield new fullerene-borate ionic complex **FP-Ant** referring to a similar synthetic method as **FP-Ph**. The structure of **FP-Ant** was confirmed by ^{1}H, ^{11}B and ^{19}F NMR, however, many efforts for growth of single crystal of **FP-Ant** didn't succeed.

Scheme 4.2 Synthesis route of **FP-Ant**.

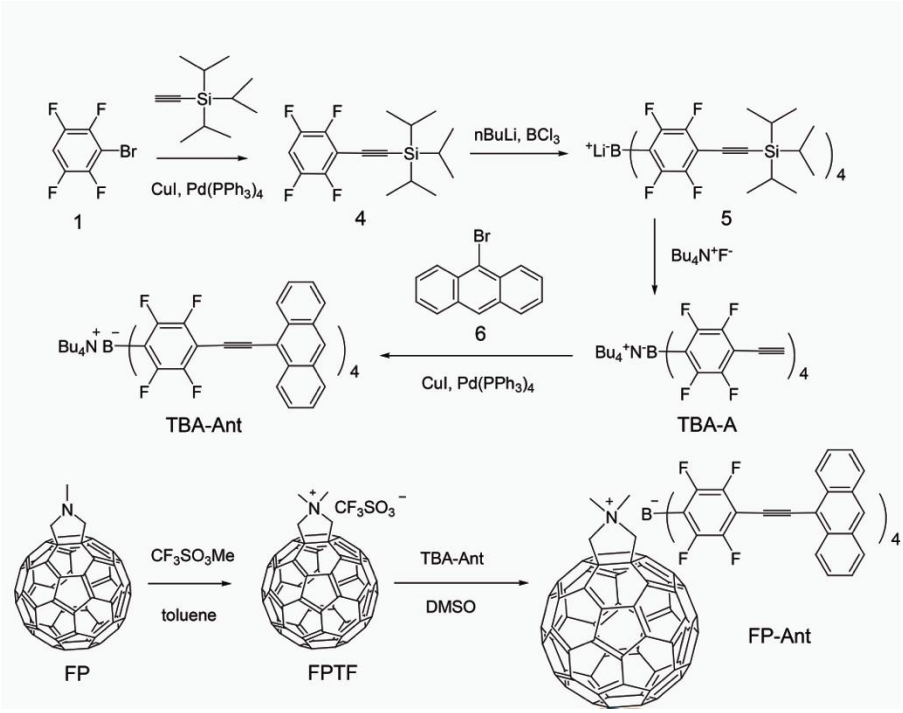

4.3.2 UV-vis Absorption and Quenching Experiment of FP-Ant

Like the model compound **FP-Ph**, the UV-vis absorption of **FP-Ant** in DMSO solution is also the superposition absorption of two precursors **FPTF** and **TBA-Ant** as shown in Figure 4.4. The maximum absorption of **FP-Ant** was found at 307 nm, while

there are also two sharp peaks at 406 nm and 430 nm corresponding to two sharp peaks from **TBA-Ant**. Compared with absorption of **FP-Ph** shown in Figure 4.2, there are more intense absorption between 350 nm to 450 nm in the absorption of new complex **FP-Ant**. Quenching experiments were carried on in diluted solutions of **TBA-Ant**, **FPTF** and **FP-Ant**, as structure of each compound shown in Scheme 4.2. The solution was firstly taken the absorption spectra to find the absorbance of λ_{max}, and then the solution was excited at λ_{max} to find the corresponding intensity of λ_{max}. Here, we defined D_{abs} is the maximum absorbance of **TBA-Ant**, D_{emi} is the maximum emission of **TBA-Ant**, DA_{abs} is the maximum absorbance of **FP-Ant** or **TBA-Ant-PCBM** (1-1) and DA_{emi} is the maximum emission of **FP-Ant** or **TBA-Ant-PCBM** (1-1). Thus, we also defined the quenching efficiency (QE) = 1- (DA_{emi}/ DA_{abs})/(D_{emi}/ D_{abs}).

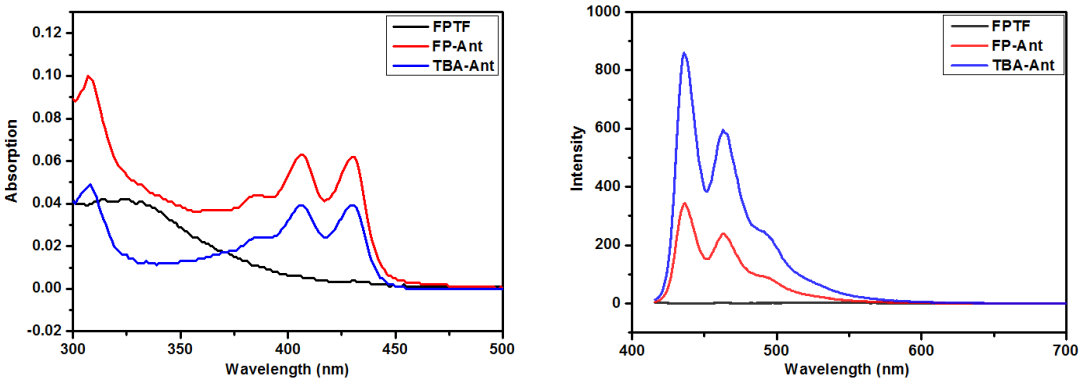

Figure 4.4 UV-vis absorption (left) and emission (right, excited at 406 nm) spectra of **TBA-Ant**, **FPTF** and **FP-Ant** (5×10^{-7} M in toluene, which was diluted from 10^{-4} M stock solution in DMSO).

All stock solutions were prepared in DMSO (10^{-4} M), and then further diluted into less polar solvent such as toluene to get same concentration solution (5×10^{-7} M), which absorption and emission spectra were shown in Fig.4.4. QE was calculated as 73%, where maximum absorbance was at 406 nm and maximum emission was at 436 nm.

Therefore, this showed 73% of fluorescence intensity of **TBA-Ant** was quenched by the ionic fullerene side. This indicated efficient photo-induced charge transfer happened in our complex, which was already reported in many D-A complex system. To further prove the efficient fluorescence quenching of ionic complex, the control experiment using **PCBM** was carried in the same condition. **PCBM** and **TBA-Ant-PCBM** (1:1 ratio) stock solution in DMSO were prepared with the addition of 10% toluene, due to the poor solubility of **PCBM** in DMSO, and then the stock solution was diluted into 5×10^{-7} M in toluene to keep almost the same solvent composition, which absorption and emission spectra were shown in Figure 4.5. QE was calculated as 31%, where maximum absorbance is at 406 nm and maximum emission is at 436 nm. It's obvious to see that the fluorescence quenching is more pronounced in our ionic fullerene-borate complex. We speculate that the more efficient fluorescence quenching in our fullerene-borate ionic complex can be explained by the ionic interaction between donor and acceptor units, which makes the photo-induced charge transfer more pronounced compared to a D-A system with neutral acceptor such as PCBM.

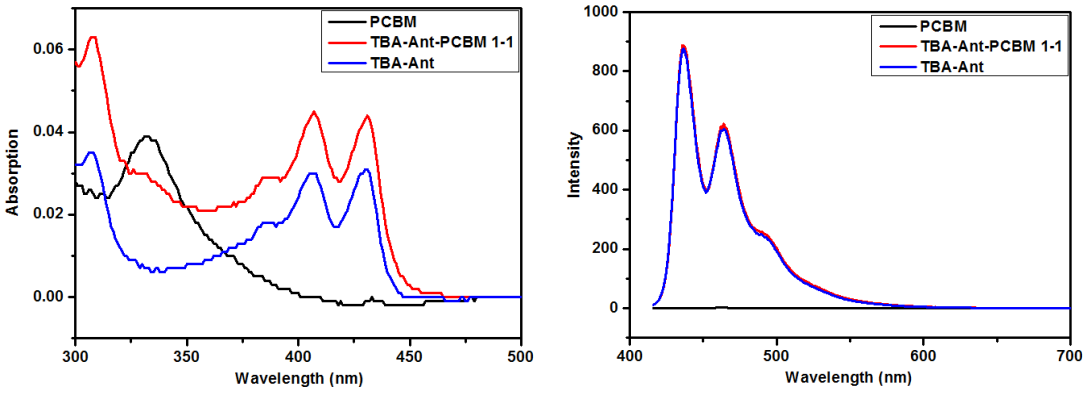

Figure 4.5 UV-vis absorption (left) and emission (right, excited at 406 nm) spectra of **TBA-Ant**, **PCBM** and **TBA-Ant-PCBM** (5×10^{-7} M in toluene, which was diluted from 10^{-4} M stock solution in DMSO).

4.4 Synthesis of More Fullerene-Borate Ionic Complexes

According to the synthetic methods developed in previous section, more different sizes of chromophores can be attached to borate center through Sonogashira coupling reactions. All fullerene-borate ionic complexes can be easily obtained by ionic exchange with **FPI** or **FPTF** according to the method described above. The structures of each complex were fully characterized by NMR such as ^{1}H, ^{11}B, ^{19}F and ^{31}P, however, growth of single crystals of them didn't succeed in many attempts to further confirm their structures. As depicted in Scheme 4.3, a Pt-containing moiety was attached to the **TBA-A** to form **TBA-Pt**, where we induced heavy metal into our ionic borates. Newly formed Pt-bisacetylide moieties in **TBA-Pt** are very common moieties in reported metal-containing materials applied in OSCs, which might lead to facile formation of triplet excitons. Thus, we expect the final fullerene-borate ionic complex **FP-Pt** will have extended lifetimes of excitons. Similarly, FBTD and pyrene was also induced into borate center by Sonogashira coupling reactions, so we expect the absorptions of final fullerene-borate ionic complexes will have different absorption range.

Scheme 4.3 Synthesis of more fullerene-borate ionic complexes.

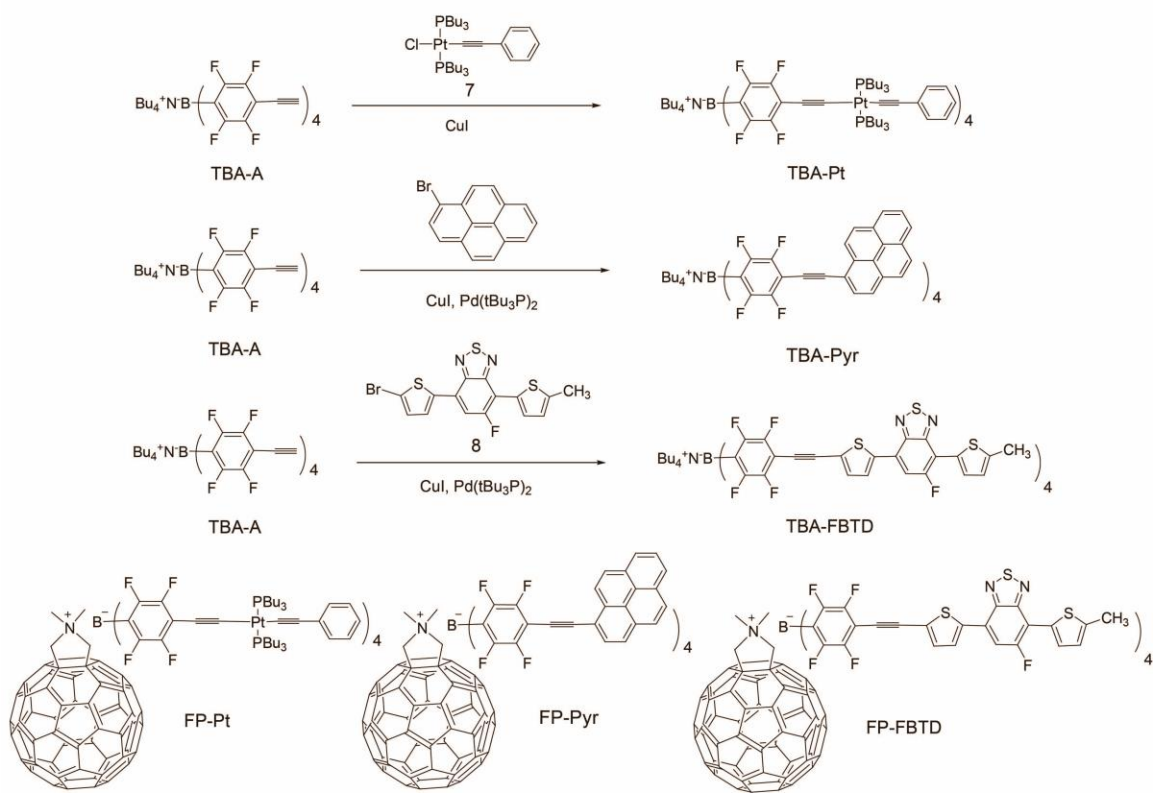

As shown in Figure 4.6, the UV-vis absorptions of newly synthesized fullerene-borate ionic complexes are also the superposition of their precursors as we mentioned before. **FP-Pt** has limited absorption in visible light range, which is mainly located between 300 nm and 350 nm. Unfortunately, no phosphorescence was observed at room temperature. **FP-Pyr** has intense absorption from 300 nm to 400 nm, while **FP-FBTD** has much broader absorption than all fullerene-borate ionic complexes we synthesized, which covers visible light range from 300 nm to 550 nm.

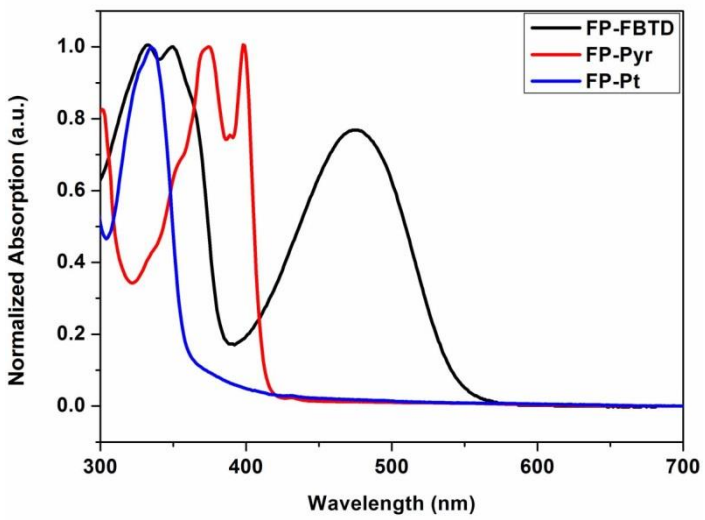

Figure 4.6 Normalized UV-vis absorption of **FP-Pt, FP-Pyr** and **FP-FBTD.**

4.5 Conclusions

In summary, we have successfully synthesized a series of fullerene-borate ionic complexes. Various chromophores can be introduced into our fullerene-borate ionic complex system through facile Sonogashira coupling reaction, and thus the optical and electrical properties of complex can be easily tuned. The fluorescence quenching study on **FP-Ant** indicated the efficient photo-induced charge transfer in our complex system, while the existence of long-lived charge separated states is under exploration. The success of obtaining single crystal of **FP-Ph** might give us some insight to develop the infinite crystalline structures of fullerene-borate ionic complex through ionic interaction between two counter ions. So far, the key factors affecting the assembling of complexes are still under investigation.

4.6 Future Plan

As we noticed that in our CV result of **FP-Ph**, a low lying LUMO of **FP-Ph** was ca. –4.12 eV, which is lower than the widely used acceptor materials PCBM. A larger difference between the LUMO of donor and acceptor materials can provide larger driving

force for electron transfer, which can promote the electron transfer efficiency. Together with the good solubility of **FP-Ph** in chlorobenzene, it is possible that **FP-Ph** can also serve as potential acceptor materials applied in organic solar cells.

Besides, Steigerwald, Nuckolls and their coworkers reported three new solids: $[Co_6Se_8(PEt_3)_6][C_{60}]_2$, $[Cr_6Te_8(PEt_3)_6][C_{60}]_2$, and $[Ni_9Te_6(PEt_3)_8][C_{60}]$. The former two assemble into a superatomic relative of the CdI_2 structure type, and the latter forms a simple rock-salt crystal. They used the clusters in similar size and shape to create binary assemblies, whose infinite crystalline structures are determined not only by the shapes of the clusters but also by the degree of charge transfer between the constituents.[60] Thus, electronic and magnetic properties of their solid-state materials, can be tuned by varying the constitution of the superatom building blocks. Inspired by their work, our fullerene-borate ionic complex should be able to get infinite crystalline structures by adjusting the size of two counter ions or tuning the electronic communication of two counter ions. Thus, promising electronic and magnetic properties of fullerene-borate ionic complex are expected.

4.7 Experimental Section

4.7.1 Materials and General Methods

All reagents and solvents were used as received from Sigma-Aldrich or Alfa Aesar unless otherwise noted. Anhydrous THF was distilled from Na/benzophenone prior to use. 300.13 MHz ^{1}H, 75.48 MHz ^{13}C and 282.37 MHz ^{19}F NMR spectra were recorded on a Bruker Avance III Solution 300 spectrometer. ^{1}H spectra were referenced internally to solvent signal. ^{19}F were referenced externally by using C_6F_6 ($\delta = -164.9$ ppm). Time-of-flight mass spectrometry (TOF MS) was performed on a Waters/Micromass LCT

Premier system operating under atmospheric pressure photoionization ($APPI^+$) mode. Ultraviolet-visible (UV-vis) absorption spectra were recorded on a Shimadzu UV-2401 PC spectrometer over a wavelength range of 240-900 nm. Fluorescence emission spectra were obtained using a Varian Cary Eclipse fluorimeter. Cyclic voltammetry was performed at 25 ℃ on a CH Instrument CHI604xD electrochemical analyzer using a glassy carbon working electrode, a platinum wire counter electrode, and a Ag/AgCl reference electrode calibrated using ferrocene redox couple (4.8 eV below vacuum). Tetrabutylammonium hexafluorophosphate (Bu_4NPF_6, 0.1 M) was used as the supporting electrolytes for the measurement. CV in solution was performed by dissolving samples in acetonitrile (1 mM) and adding into Bu_4NPF_6 (0.1 M) in acetonitrile during measurement. X-ray diffraction was performed on Bruker Kappa APEX II CCD diffractometer at the Department of Chemistry and Chemical Biology, UNM.

4.7.2 Synthetic Procedures

Compound 2: Compound **1** 2.29 g (10.0 mmol) and phenylacetlyene 1.53 g (15.0 mmol) was dissolved in 8 ml anhydrous THF and 2 mL TEA in a pressure vessel containing a magnetic stir bar. $Pd(PPh_3)_4$ (57.8 mg 5.0 mol%) and CuI (189.8 mg 10.0 mol%) were added to the pressure vessel in argon filled glovebox. The pressure vessel was sealed and taken out of the glove box. The reaction was carried out at 80 ℃ for 24 hours. After cooling the reaction mixture to room temperature, the resulted reaction mixture was firstly removed solvent by rotor-vapor. The crude product was further purified by silica gel chromatography with hexane/dichloromethane and then recrystallized from methanol. (2.15 g Yield 86.0%) ^1H NMR (300.13 MHz, $CDCl_3$), δ (ppm) = 7.05 (*Ph-H*, m, 1H),

7.35 -7.45 (*Ph-H*, m, 3H), 7.58-7.61 (*Ph-H*, m, 2H); ^{19}F NMR ($CDCl_3$), δ (ppm) = -135.1 (dd, 2F), -137.4 (dd, 2F).

Compound 3: To a dry 250 ml Schlenk flask add 500 mg (2.0 mmol) compound **2**, 20 - 30 ml anhydrous diethyl ether was then transferred into flask at -78 ℃. 0.8 mL nBuLi solution was added into the solution at -78 ℃. The mixture was kept stirring at -78 ℃ for 2 hours. And then, 0.5 mL BCl_3 1M solution was added into reaction mixture and further kept stirring at low temperature for another hour, and finally the reaction mixture was stirring at room temperature for overnight. The resulted reaction mixture was firstly removed the solvent by vacuum, which yield some yellow solid. The yellow solid was washed by large amount hexane, which gave the final compound. ^{1}H NMR (300.13 MHz, $CDCl_3$), δ (ppm) = 7.33 - 7.35 (*Ph-H*, m, 12H), 7.51 -7.54 (*Ph-H*, 8H); ^{11}B NMR ($CDCl_3$), δ (ppm) = -16.4; ^{19}F NMR ($CDCl_3$), δ (ppm) = -131.3 (s, 8F), - 139.6 (s, 8F).

TBA-Ph: compound 3 152.1 mg (0.15 mmol) and tetrabutylammonia bromide 644.8 mg (2.0 mmol) was dissolved in 5 ml methanol, and then stirring at room temperature for overnight. The white solid was precipitated out, and then the solid was filtered and collect the white solid. The crude compound was further recrystallized in pure methanol to yield final compound. (120 mg Yield 64%). ^{1}H NMR (300.13 MHz, $CDCl_3$), δ (ppm) = 0.95 (-CH_3, t, 12H, J = 7.2 Hz), 1.32 (-CH_2, m, 8H), 1.50 (-CH_2, m, 8H), 2.96 (-*CH*, t, 8H, J = 8.1 Hz), 7.33 - 7.35 (*Ph-H*, m, 12H), 7.52 -7.55 (*Ph-H*, 8H); ^{11}B NMR ($CDCl_3$), δ (ppm) = -16.4; ^{19}F NMR ($CDCl_3$), δ (ppm) = -130.4 (s, 8F), - 139.6 (s, 8F).

FP-Ph: TBA-Ph 40.9 mg (0.033 mmol) was dissolved in 3 ml DMSO, and then added into ionic fulleropyrrolidine FPI 28.2 mg (0.031 mmol) 3 mL DMSO solution with further stirring for 30 min. Then, H_2O was slowly added by dropwise until the brown

solids started to precipitate out. The suspension reaction mixture was kept stirring for 30 min, and then more H_2O was added. The suspension mixture was placed for 20 min, and then filtrated to collect the brown solid. The brown solid was further washed by large amount of DI H_2O. After that, the brown solid was dispersed in 30 ml methanol and stirring for 1 h before filtration. The suspension solution was filtered again and washed by methanol to yield target compound. (43 mg Yield 77.7%). ^{1}H NMR (300.13 MHz, $CDCl_3$), δ (ppm) = 4.08 (-CH3, s, 6H), 5.29 (-CH2, s, 4H), 7.32 (*Ph-H*, m, 12H), 7.50 - 7.51 (*Ph-H*, 8H); ^{11}B NMR ($CDCl_3$), δ (ppm) = -16.4; ^{19}F NMR ($CDCl_3$), δ (ppm) = - 130.1 (s, 8F), - 139.0 (s, 8F).

Compound 4: Compound 1 1.15 g (5.0 mmol) and TiPS-acetylene 1.35 g (7.5 mmol) was dissolved in 5 ml anhydrous THF and 5 mL TEA in a pressure vessel containing a magnetic stir bar. $Pd(PPh_3)_4$ (28.9 mg 5.0 mol%) and CuI (94.9 mg 10.0 mol%) were added to the pressure vessel in argon filled glovebox. The pressure vessel was sealed and taken out of the glove box. The reaction was carried out at 80 ^{o}C for 24 hours. After cooling the reaction mixture to room temperature, the resulted reaction mixture was firstly removed solvent by rotor-vapor. The crude product was further purified by silica gel chromatography with hexane and dry in high vacuum to remove the excess TiPS-acetylene. (1.10 g Yield 66.7%) ^{1}H NMR (300.13 MHz, $CDCl_3$), δ (ppm) = 1.14 (m, 21H), 7.02 (*Ph-H*, *tt*, 1H); ^{19}F NMR ($CDCl_3$), δ (ppm) = - 134.9 (dd, 2F), -137.7 (dd, 2F).

Compound 5: (1.80 g, 5.45 mmol) compound 4 were dissolved in 20 mL anhydrous diethyl ether under argon. The solution was cooled to -78 °C and one equivalent n-Butyllithium (2.1 mL, 5.25 mmol) was added dropwise. After one hour 0.25 equivalents BCl_3 (1.25 mL of a 1 M solution in heptane) were slowly added. The mixture was

allowed to warm to room temperature overnight, whereupon a white suspension was obtained. After removal of the solvent in vacuum, the white precipitate was dissolved in methylene chloride and precipitated in hexane two times. The precipitate was filtered, washed with hexane and dried to afford the pure compound as a white powder. (1.24g, Yield 74.5%) ^{1}H NMR (300.13 MHz, $CDCl_3$), δ (ppm) = 1.10 (m, 21H); ^{19}F NMR ($CDCl_3$), δ (ppm) = - 131.4 (s, 8F), -139.3(s, 8F). ^{11}B NMR ($CDCl_3$), δ (ppm) = -16.6.

Compound 6: Anhydrous copper (II) bromide (11.3 g; 50 mmol) was added to a solution of anthracene (4.45 g; 25 mmol) in tetrachloromethane (125 mL). The reaction mixture was heated under reflux for 18 hr. Copper (II) bromide was then removed by filtration and the filtrate was evaporated in vacuum to give an orange solid. The crude product was purified by silica gel chromatography with hexane, yielding 9-bromoanthracene (4.8 g, 74.7 %). ^{1}H NMR (300.13 MHz, $CDCl_3$), δ (ppm) = 7.48 (*Ph-H*, dd, 2H, J^3_{HH} = 7.2 Hz), 7.61 (*Ph-H*, dd, 2H, J^3_{HH} = 7.2 Hz), 8.01 (*Ph-H*, d, 2H, J^3_{HH} = 8.4 Hz), 8.45 (*Ph-H*, s, 1H), 8.52 (*Ph-H*, d, 2H, J^3_{HH} = 8.7 Hz)

TBA-A: To a solution of 1.60 g (1.20 mmol) compound 5 in THF (50 mL) was added dropwise a solution of tetrabutylammonium fluoride (1.88 g, 7.19 mmol) in THF (50 mL). The mixture was stirred for 2 h at room temperature. After washing 3 times with a concentrated aqueous solution of sodium chloride, the solvent removed under vacuum. The remainder was dissolved in methylene chloride, filtered over silica, precipitated in hexane two times and dried to afford the pure compound as a white solid. (940 mg, Yield 82.8%) ^{1}H NMR (300.13 MHz, $CDCl_3$), δ (ppm) = 0.94 (t, 12H), 1.31 (m, 8H), 1.52 (m, 8H), 2.95 (t, 8H), 3.45 (s, 4H); ^{19}F NMR ($CDCl_3$), δ (ppm) = - 130.2 (s, 8F), -139.5(s, 8F). ^{11}B NMR ($CDCl_3$), δ (ppm) = -16.5.

TBA-Ant: 128.5 mg (0.5 mmol) 9-bromoanthracene and TBA-A 94.5 mg (0.1 mmol) was dissolved in 20 ml THF and 4 ml TEA in a pressure vessel containing a magnetic stir bar. $Pd(PPh_3)_4$ (11.5 mg 10.0 mol%) and CuI (3.8 mg 20.0 mol%) were added to the pressure vessel in argon filled glovebox. The pressure vessel was sealed and taken out of the glove box. The reaction was carried out at 80 ℃ for 2 days, and the resulted reaction mixture was dissolved in large amount THF. Then, the insoluble salt or solid were filtered out. The resulting filtrate was concentrated and yield light golden yellow solid, which was further washed by MeOH and $CHCl_3$ to yield final pure compound as yellow solid. (80 mg Yield 45.7%) ^{1}H NMR (300.13 MHz, DMSO-d_6), δ (ppm) = 0.84 (-*CH_3*, t, 12H, J = 7.2 Hz), 1.21 (-*CH_2*, m, 8H), 1.47 (-*CH_2*, m, 8H), 3.06 (-*CH_3*, t, 8H), 7.63 (*Ph-H*, dd, 8H, J^3_{HH} = 7.2 Hz), 7.76 (*Ph-H*, dd, 8H, J^3_{HH} = 7.2 Hz), 8.19 (*Ph-H*, d, 8H, J^3_{HH} = 8.1 Hz), 8.52 (*Ph-H*, d, 8H, J^3_{HH} = 8.4 Hz), 8.79 (*Ph-H*, s, 4H); ^{11}B NMR (DMSO-d_6), δ (ppm) = -15.7; ^{19}F NMR (DMSO-d_6), δ (ppm) = -129.5, (s, 8F), - 138.3 (s, 8F).

FP: C_{60} (540 mg, 0.75 mmol) was dissolved in toluene (600 ml) by sonicating for 5 minutes. To this solution were added sarcosine (133.6 mg, 1.50 mmol) and paraformaldehyde (112.5 mg, 3.75 mmol), the reaction mixture was refluxing at 140 ℃ for 2 hours. Solvents were removed on a rotavap under vacuum. The product was dissolved in a minimum amount of toluene and loaded onto a silica gel column packed with toluene and eluted with toluene containing 0-5% acetone to collect pure compound. (200 mg, Yield 34.3%) ^{1}H NMR (300.13 MHz, $CDCl_3$), δ (ppm) = 3.01 (-*CH_3*, s, 3H), 4.41 (-*CH_2*, s, 4H).

FPTF: Methylation of **FP** (139.9 mg, 0.18 mmol) was carried out by dissolving the compounds in 100 ml toluene, and (147.7 mg, 0.90 mmol) Methyl triflate was added at

room temperature. The reaction mixture was stirring at room temperature for overnight. Pure methylated products **FPTF** were precipitated by adding hexanes after removing the solvent. (150 mg, Yield 88.6%) ^{1}H NMR (300.13 MHz, DMSO-d_6), δ (ppm) = 4.07 (-*CH*$_3$, s, 6H), 5.73 (-*CH*$_2$, s, 4H). ^{19}F NMR (DMSO-d_6), δ (ppm) = -75.6 (s, 3F).

FP-Ant: **TBA-Ant** (28.8 mg, 0.02 mmol) and **FPTF** (18.8 mg, 0.02 mmol) was dissolved in 8 ml DMSO, and then DI H_2O was added by dropwise until the solid was precipitated out. The solid was collected by vacuum filtration. Then, the resulting solid was dissolved in THF and filtered again to get rid of some insoluble solid impurity. The filtrate was concentrated and precipitated from methanol to yield final pure target compound. ^{1}H NMR (300.13 MHz, DMSO-d_6), δ (ppm) = 4.04 (-*CH*$_3$, s, 6H), 5.67 (-*CH*$_2$, s, 4H), 7.63 (*Ph-H*, dd, 8H, J^3_{HH} = 7.2 Hz), 7.76 (*Ph-H*, dd, 8H, J^3_{HH} = 7.2 Hz), 8.19 (*Ph-H*, d, 8H, J^3_{HH} = 8.4 Hz), 8.52 (*Ph-H*, d, 8H, J^3_{HH} = 8.4 Hz), 8.79 (*Ph-H*, s, 4H); ^{11}B NMR (DMSO-d_6), δ (ppm) = -15.7; ^{19}F NMR (DMSO-d_6), δ (ppm) = -129.5, (s, 8F), - 138.2 (s, 8F).

TBA-Pt 18.9 mg (0.02 mmol) **TBA-A** and **compound 7** 61.8 mg (0.084 mmol) was dissolved in 5 ml chloroform and 1 ml triethylamine in a pressure vessel containing a magnetic stir bar. CuI (0.8 mg 20.0 mol%) were added to the pressure vessel in argon filled glovebox. The pressure vessel was sealed and taken out of the glove box. The reaction was carried out at room temperature for 24 hours, and the resulted reaction mixture was firstly removed the solvent by rotor vapor. The crude compound precipitated from cold methanol to yield white solid. (56.0 mg Yield 74.8%) ^{1}H NMR (300.13 MHz, $CDCl_3$), δ (ppm) = 0.90 (-*CH*$_3$, m, 60H), 1.32 (-*CH*$_2$, m, 56H), 1.57 (-*CH*$_2$, m, 56H), 2.14 (-*CH*$_2$, t, 48H), 2.95 (-*CH*$_2$, t, 8H) 7.07 - 7.28 (*Ph-H*, m, 20H); ^{11}B NMR ($CDCl_3$), δ (ppm)

= -16.5; ^{19}F NMR ($CDCl_3$), δ (ppm) = -132.7 (s, 8F), - 142.2 (s, 8F); ^{31}P NMR ($CDCl_3$), δ (ppm) = 3.66.

FP-Pt: **TBA-Pt** (11.2 mg, 3.0 umol) and **FPTF** (3.4 mg, 3.6 umol) was dissolved in 1 ml DMSO and 1 ml THF, and then MeOH was added by dropwise until the solid was precipitated out. The solid was collected by vacuum filtration. Then, the resulting solid was dissolved in acetone and filtered again to get rid of some insoluble solid impurity. The filtrate was concentrated and dried as final compound. ^{1}H NMR (300.13 MHz, acetone-d6), δ (ppm) = 0.90 (-*CH*$_3$, t, 84H, J = 7.2 Hz), 1.45 (-*CH*$_2$, m, 56H), 1.62 (-*CH*$_2$, m, 56H), 2.18 (-*CH*$_2$, m, 56H), 4.51 (-*CH*$_3$, s, 6H), 6.08 (-*CH*$_2$, s, 4H), 7.08-7.24 (-*Ph-H*, m, 20H); ^{11}B NMR (aceton-d6), δ (ppm) = -15.4; ^{19}F NMR (aceton-d6), δ (ppm) = -131.5 (s, 8F), - 142.7 (s, 8F); ^{31}P NMR (aceton-d6), δ (ppm) = 5.17.

TBA-FBTD: 180 mg (0.44 mmol) **compound 8** and **TBA-A** 100.9 mg (0.11 mmol) was dissolved in 50 ml THF and 5 ml TEA in a pressure vessel containing a magnetic stir bar. $Pd(tBu_3P)_2$ (5.6 mg 10.0 mol%) and CuI (4.2 mg 20.0 mol%) were added to the pressure vessel in argon filled glovebox. The pressure vessel was sealed and taken out of the glove box. The reaction was carried out at room temperature for 24 hours, and the resulted reaction mixture was firstly removed solvent by rotor vapor and washed by chloroform to yield dark red solid. (210 mg Yield 84.2%) ^{1}H NMR (300.13 MHz, $CDCl_3$), δ (ppm) = 1.00 (-*CH*$_3$, t, 12H, J = 7.2 Hz), 1.36 (-*CH*$_2$, m, 8H), 1.54 (-*CH*$_2$, m, 8H), 2.60 (-*CH*$_3$, s, 3H), 3.0 (-*CH*$_2$, t, 8H, J = 8.1 Hz), 6.90 (-*Th-H*, 4H, J = 3.9 Hz), 7.38 (-*Th-H*, d, 4H, J = 3.9 Hz), 7.73 (-*Ph-H*, d, 1H, J = 12.9 Hz), 7.95 (-*Th-H*, d, 1H, 3.9 Hz), 8.06 (-*Th-H*, 1H, J = 3.3 Hz); ^{11}B NMR (THF), δ (ppm) = -16.0; ^{19}F NMR (THF), δ (ppm) = -108.3, (s, 4F), -130.4 (s, 8F), - 139.6 (s, 8F).

FP-FBTD: **TBA-FBTD** (45.4 mg, 0.02 mmol) and **FPTF** (18.8 mg, 0.02 mmol) was dissolved in 4 ml DMSO and 4 ml THF in 20 ml vial, and then the reaction mixture was left in fume hood to slowly evaporate THF. After 2 days, two solid layers were formed at the bottom and top of solvent phase. The resulting solid was collected by vacuum filtration and washed by MeOH. (40 mg, Yield 71.0%) The compound showed limited solubility in THF, but should dissolve in THF and DMSO mixture. ^{11}B NMR (THF), δ (ppm) = -15.9; ^{19}F NMR (THF), δ (ppm) = -108.4, (s, 4F), -130.0 (s, 8F), -140.1 (s, 8F).

TBA-Pyr: 112.5 mg (0.4 mmol) **bromopyrene** and **TBA-A** 94.5 mg (0.1 mmol) was dissolved in 20 ml THF and 10 ml TEA in a pressure vessel containing a magnetic stir bar. $Pd(tBu_3P)_2$ (5.0 mg 10.0 mol%) and CuI (4.0 mg 20.0 mol%) were added to the pressure vessel in argon filled glovebox. The pressure vessel was sealed and taken out of the glove box. The reaction was carried out at room temperature for 2 days, and the resulted reaction mixture was firstly removed solvent by rotor vapor and purified by column by dichloromethane and hexane to yield light yellow solid. (80 mg Yield 45.7%) ^{1}H NMR (300.13 MHz, DMSO-d_6), δ (ppm) = 0.92 (-*CH*$_3$, t, 12H, J = 7.2 Hz), 1.30 (-*CH*$_2$, m, 8H), 1.54 (-*CH*$_2$, m, 8H), 3.14 (-*CH*$_3$, t, 8H), 8.13 – 8.45 (-*Ph-H*, m, 32H), 8.59 (-*Ph-H*, 4H, J = 9.3 Hz); ^{11}B NMR (DMSO-d_6), δ (ppm) = -15.7; ^{19}F NMR (DMSO-d_6), δ (ppm) = -129.6, (s, 8F), - 138.3 (s, 8F).

FP-Pyr: **TBA-Pyr** (35.0 mg, 0.02 mmol) and **FPTF** (18.8 mg, 0.02 mmol) was dissolved in 8 ml DMSO, and then DI H_2O was added by dropwise until the solid was precipitated out. The solid was collected by vacuum filtration. Then, the resulting solid was dissolved in THF and filtered again to get rid of some insoluble solid impurity. The filtrate was concentrated and precipitated from methanol. ^{1}H NMR (300.13 MHz, DMSO-d_6), δ (ppm)

= 4.07 (-*CH*$_3$, s, 6H), 5.71 (-*CH*$_2$, s, 4H), 8.14 – 8.46 (-*Ph-H*, m, 32H), 8.59 (-*Ph-H*, 4H, J = 9.0 Hz); ^{11}B NMR (DMSO-d$_6$), δ (ppm) = -15.7; ^{19}F NMR (DMSO-d$_6$), δ (ppm) = -129.5 (s, 8F), - 138.2 (s, 8F).

4.8 References

(1) Echegoyen, L.; Diederich, F.; Echegoyen, L. E. *Fullerenes, Chemistry, Physics, and Technology, Kadish, K. M.; Ruoff, R. S., Ed.* Wiley-Interscience, New York, **2000**, pp. 1.

(2) Guldi, D. M.; Fukuzumi, S. *Fullerenes: From Synthesis to Optoelectronic Properties, Guldi, D. M.; Martin, Kluwer, Dordrecht, N., Ed.* **2003**, pp. 237.

(3) Sgobba, V.; Rahman, G. M. A.; Guldi, D. M. *Carbon Nanotubes in Electron Donor–Acceptor Nanocomposites, Chemistry of Carbon Nanotubes, Basiuk, V. A., Ed.* American Scientific Publishers, California, **2006**.

(4) Fukuzumi, S.; Guldi, D. M. *Electron Transfer in Chemistry, Balzani, V., Ed.* Wiley-VCH, Weinheim, **2001**, 2, pp. 270.

(5) Frey, J.; Kodis, G.; Straight, S. D.; Moore, T. A.; Moore, A. L.; Gust, D. *J. Phys. Chem. A* **2013**, 117, 607.

(6) Gust, D.; Moore, T.A.; Moore, A. L. *In Electron Transfer in Chemistry; Balzani, V., Ed.* Wiley-VCH: Weinheim, **2001**, 3, pp 272.

(7) Gust, D.; Moore, T. A.; Moore, A. L. *Acc. Chem. Res.* **1993**, 26, 198.

(8) Gust, D.; Moore, T. A.; Moore, A. L. *Acc. Chem. Res.* **2009**, 42, 1890.

(9) Bottari, G.; De la Torre, G.; Guldi, D. M.; Torres, T. *Chem. Rev.* **2010**, 110, 6768.

(10) D'Souza, F.; Ito, O. *Chem. Soc. Rev.* **2012**, 41, 86.

(11) Balzani, V.; Ceroni, P.; Juris, A.; Venturi, M.; Campagna, S.; Puntorieno, F.; Serroni. S. *Coord. Chem. Rev.* **2001**, 219-221, 545.

(12) Fukuzumi, S. *Org. Biomol. Chem.* **2003**, 1, 609.

(13) Fukuzumi, S. *Phys. Chem. Chem. Phys.* **2008**, 10, 2283.

(14) Fukuzumi, S.; Ohkubo, K. *J. Mater. Chem.* **2012**, 22, 4575.

(15) Fukuzumi, S.; Ohkubo, K.; Suenobu, T. *Acc. Chem. Res.* **2014**, 47, 1455.

(16) Kirner, S.; Sekita, M.; Guldi, D. M. *Adv. Mater.* **2014**, 26, 1482.

(17) D'Souza, F.; Ito, O. *Chem. Soc. Rev.* **2012**, 41, 86.

(18) Fukuzumi, S.; Ohkubo, K.; D'Souza, F.; Sessler, J. L. *Chem. Commun.* **2012**, 48, 9801.

(19) D'Souza, F.; Ito, O. *Chem. Commun.* **2009**, 33, 4913.

(20) Chitta, R.; D'Souza, F. *J. Mater. Chem.* **2008**, 18, 1440.

(21) Guldi, D. M.; Costa, R. D. *J. Phys. Chem. Lett.* **2013**, 4, 1489.

(22) Bottari, G.; Trukhina, O.; Ince, M.; Torres, T. *Coord. Chem. Rev.* **2012**, 256, 2453.

(23) Costa, R. D.; Lodermeyer, F.; Casillas, R.; Guldi, D. M. *Energy Environ. Sci.* **2014**, 7, 1281.

(24) Guldi, D. M.; Sgobba, V. *Chem. Commun.* **2011**, 47, 606.

(25) Shen, Y.; Nakanishi, T. *Phys. Chem. Chem. Phys.* **2014**, 16, 7199.

(26) Fukuzumi, S.; Ohkubo, K. *Dalton Trans.* **2013**, 42, 15846.

(27) Babu, S. S.; Moehwald, H.; Nakanishi, T. *Chem. Soc. Rev.* **2010**, 39, 4021.

(28) Guldi, D. M.; Illescas, B. M.; Atienza, C. M.; Wielopolski, M.; Martin, N. *Chem. Soc. Rev.* **2009**, 38, 1587.

(29) Wang, T.; Pearson, A. J.; Lidzey, D. G. *J. Mater. Chem. C* **2013**, 1, 7266.

(30) Jariwala, D.; Sangwan, V. K.; Lauhon, L. J.; Marks, T. J.; Hersam, M. C. *Chem. Soc. Rev.* **2013**, 42, 2824.

(31) Dubacheva, G. V.; Liang, C.-K.; Bassani, D. M. Coord. *Chem. Rev.* **2012**, 256, 2628.

(32) Ricks, A. B.; Brown, K. E.; Wenninger, M.; Karlen, S. D.; Berlin, Y. A.; Co, D. T.; Wasielewski, M. R. *J. Am. Chem. Soc.* **2012**, 134, 4581.

(33) Lewis, F. D.; Letsinger, R. L.; Wasielewski, M. R. *Acc. Chem. Res.* **2001**, 34, 159.

(34) Wasielewski, M. R. *Acc. Chem. Res.* **2009**, 42, 1910.

(35) Faiz, J. A.; Heitz, V.; Sauvage, J.-P. *Chem. Soc. Rev.* **2009**, 38, 422.

(36) Diederich, F.; Gomez-Lo´pez, M.´ *Chem. Soc. Rev.* **1999**, 28, 263.

(37) Chambron, J.-C.; Collin, J.-P.; Dalbavie, J.-O.; Dietrich-Buchecker, C. O.; Heitz, V.; Odobel, F.; Solladie, N.; Sauvage, J.-P. *Coord. Chem. Rev.* **1998**, 178-180, 1299.

(38) *The Photosynthetic Reaction Center; Deisenhofer, J., Norris, J. R., Ed.* Academic Press: San Diego, **1993**.

(39) *Molecular Level Artificial Photosynthetic Materials; Meyer, G. J., Ed.* John Wiley & Sons: New York, **1997**.

(40) Hodgkiss, J. M.; Tu, G.; Albert-Seifried, S.; Huck, W. T.; Friend, R. H. *J. Am. Chem. Soc.* **2009**, 131, 8913.

(41) Allemand, P.-M.; Khemani, K. C.; Koch, A.; Wudl, F.; Holczer, K.; Donovan, S.; Grüner, G.; Thompson, J. D.; Science **1991**, 253, 301.

(42) Konarev, D. V.; Khasanov, S. S.; Otsuka, A.; Maesato, M.; Saito, G.; Lyubovskaya, R. N. *Angew. Chem. Int. Ed.* **2010**, 49, 4829.

(43) Konarev, D. V.; Lyubovskaya, R. N. *Russ. Chem. Rev.* **2012**, 81, 336.

(44) Ohkubo, K., Kawashima, Y., Fukuzumi, S. *Chem. Comm.* **2012**, 48, 4314.

(45) Nakamura, E.; Isobe, H. *Acc.Chem. Res.* **2003**, 36, 807.

(46) Guldi, D. M.; Prato, M. *Acc. Chem. Res.* **2000**, 33, 695.

(47) Li, H.; Hollamby, M. J.; Seki, T.; Yagai, S.; Möhwald, H.; Nakanishi, T. *Langmuir* **2011**, 27, 7493.

(48) Aoyagi, S., Nishibori, E., Sawa, H., Sugimoto, K., Takata, M., Miyata, Y., Kitaura, R.; Shinohara, H.; Okada, H.; Sakai, T.; Ono, Y; Kawachi, K.; Yokoo, K.; Ono, S.; Omote, K.; Kasama, Y.; Ishikawa, S.; Komuro, T.; Tobita, H. *Nature Chem.* **2010**, 2, 678.

(49) Li, C. Z.; Chueh, C. C.; Yip, H. L.; O'Malley, K. M.; Chen, W. C.; Jen, A. K.-Y. *J. Mater. Chem.* **2012**, 22, 8574.

(50) O'Malley, K. M.; Li, C. Z.; Yip, H. L.; Jen, A. K.-Y. *Adv. Energy Mater.* **2012**, 2, 82

(51) Hudson, Z.M.; Wang, S. *Acc. Chem. Res.* **2009**, 42, 1584.

(52) Wade, C. R.; Broomsgrove, A. E.; Aldridge, S.; Gabbai, F. P. *Chem. Rev.* **2010**, 110, 3958.

(53) Kim, D.-S.; Ham, J. *Org. Lett.* **2010**, 12, 1092.

(54) Kobayashi, H.; Sonoda, T.; Iwamoto, H. *Chem. Lett.* **1982**, 8, 1185;

(55) Iwamoto, H.; Sonoda, T.; Kobayashi, H. *Tetrahedron Lett.* **1983**, 24, 4703.

(56) Iwamoto, H.; Sonoda, T.; Kobayashi, H. *J. Fluorine Chem.* **1984**, 24, 535.

(57) Kobayashi, H. *J. Fluorine Chem.* **2000**, 105, 201.

(58) Maggini, M.; Scorrano, G. *J. Am. Chem. Soc.* **1993**, 115, 9798.

(59) Türp, D., Wagner, M., Enkelmann, V.; Müllen, K. *Angew. Chem. Int. Ed.* **2011**, 50, 4962.

(60) Roy, X.; Lee, C. H.; Crowther, A. C.; Schenck, C. L.; Besara, T.; Lalancette, R. A.; Seigrist, T.; Stephens, P. W.; Brus, L. E.; Kim, P.; Steigerwald, M. L.; Nuckolls, C. *Science* **2013**, 341, 157.